Small-Scale Kinematics of HI in Nearby Spiral Galaxies

Domenico Tamburro
Max–Planck–Institut für Astronomie

Heidelberg 2008

Dissertation in Astronomy
submitted to the
Combined Faculties for the Natural Sciences and for
Mathematics of the Ruperto–Carola University of
Heidelberg, Germany
for the degree of
Doctor of Natural Sciences

presented by
Dipl.–Astron. *Domenico Tamburro*
born in Caserta, Italy

Oral examination: **21.05.2008, 14:00 pm**

Small-Scale Kinematics of HI in Nearby Spiral Galaxies

Referees: Prof. Dr. Hans-Walter Rix
Prof. Dr. Ralph S. Klessen

Zusammenfassung – Deutsch

Wir untersuchen die Zeitskala für Sternenstehung und die energetische Rückkopplung an das interstellare Gas in einer Stichprobe von nahen Galaxien, basierend auf einem Satz einzigartiger Multi-Wellenlängen-Karten. Insbesondere umfassen diese Daten 21-cm-Emissionslinien-Bilder aus dem THINGS Projekt, sowie dem 24 μm Band des Spitzer Satelliten. Aus diesen Daten werden Proxy-Karten für das Gas-Reservoir konstruiert, aus dem Sterne entstehen, sowie für die Sternentstehungsrate und den kinetischen Energieinhalt des H I Gases.

Aus einem Vergleich der Winkelverschiebung zwischen H I und 24 μm Emissionsspitzen als Funktion des Radius für eine Stichprobe von 14 Galaxien stellen wir fest, dass wenigstens ein Teil der spiralarminduzierten Sternentstehung die Molekülwolkenphase sehr schnell durchläuft, innerhalb von 10^6 bis $4{\times}10^6$ Jahren.

Wir finden, dass die H I Geschwindigkeitsdispersion und Sternenstehungsrate in einer Stichprobe von normalen und Zwergengalaxien korreliert sind. Da die spezifische E_{kin}(H I) lokal mit der Sternenstehungsrate skaliert, ist es plausibel, dass Sternentstehung ein Teil der Turbulenz antreibt. Die Galaxien aus der Stichprobe zeigen einen systematischen radialen Abfall der H I Geschwindigkeitsdispersion. Bei einer stellaren Flächenhelligkeit von $\mu_B = 25$ mag arcsec^{-2} zeigen alle Galaxien ähnliche Werte von H I Geschwindigkeitsdispersion, 10 ± 1 km s^{-1}, H I Massendichte, ~ 3 M$_\odot$ pc^{-2}, und Sternenstehungsrate, $10^{-9.5}$ M$_\odot$ yr^{-1} pc^{-2}.

Abstract – English

We study the timescales for star-formation and the energetic feedback to the inter-stellar gas in a sample of nearby galaxies, drawing on a unique multi-wavelength mapping. In particular, these data encompass 21-cm emission line maps from the THINGS project, 24 μm band from the Spitzer satellite. These data serve to construct proxy-maps for the gas reservoir from which stars form, for the star formation rate, and the kinetic energy content of the H I gas.

From comparing the angular offsets of the H I emission peaks and the 24 μm emission as a function of radius for a sample of 14 galaxies, we find that at least a portion of the spiral-arm induced star-formation proceeds rapidly through the molecular cloud phase, within 1–4 Myr.

We find that the H I velocity dispersion and star formation rate are correlated in a sample of normal and dwarf galaxies. As the specific E_{kin}(H I) scales locally with the star formation rate, it is plausible that star formation does drive some of the gas turbulence. The sample galaxies exhibit a systematic radial decline of H I velocity dispersion. At a stellar surface brightness $\mu_B = 25$ mag arcsec^{-2} all the sample galaxies show similar H I velocity dispersion, 10 ± 1 km s^{-1}, H I mass density, ~ 3 M$_\odot$ pc^{-2}, and star formation rate, $10^{-9.5}$ M$_\odot$ yr^{-1} pc^{-2}.

To Caterina

Contents

Chapter 1

Introduction

1.0 Preamble

Star formation represents at the same time a mechanism of gas consumption, dissipation, and recycling in galaxies. Therefore, it clearly influences, the evolution of galaxies since their initial assembly to the present time; on smaller scales, it affects the chemistry of the interstellar gas, and, at the smallest scales, the building of individual stars and planets. Though star formation history and galaxy evolution at high redshift are an extensive and active research field, central issues have not been clarified in the local Universe, particularly, in the solar vicinity and in nearby galaxies, where observation provide high spatial resolution and reveal a full wealth of physical properties that are still awaiting an exhaustive interpretation.

The star formation rate (SFR) is determined by the quantity of available cold gas with a sufficiently high density that local gravity prevails over all other contrasting forces and efficiently gathers the gas in order to form stars. On the other hand, the quantity of available gas is limited by its consumption during star formation. As galaxies grow in size and mass, rotational shear and Coriolis force also hinder the gas gravitational formation of gas clouds. Moreover, star forming regions are violent "feeding back" energy into their surroundings. Beside winds and ionizing radiation from young hot stars, supernovae (SN) represent the primary source of stellar feedback, shocking and heating the gas. Still, it is not clear in what relative importance are these processes quenching star formation. SNe, are fundamental for the metal enrichment of the interstellar gas, determining the class of subsequent generations of stars. The dust production from SNe and evolved (asymptotic giant branch) stars is also an essential ingredient for star formation. The opaque shield provided by the dust facilitates the accretion of individual stars. Therefore, SFR in galaxies is regulated by several conditions as critical density of the gas, galactic rotation, metalicity, opacity, etc. The observed present-day values of SFR span many orders of magnitudes among different parts within individual galaxies, and the galaxy-averaged SFR

exhibits a similar range even between galaxies of different morphological types. What determines the types of galaxies is however uncertain. Star formation involves only a small volume fraction of the total available gas, which means that the star formation efficiency (SFE) is very low, because only a small fraction of gas mass is converted into stars. SFR and SFE set the rate at which the gas reservoir is consumpted. However, it has not been well established what limits the SFE.

1.0.1 Overview

Here we list the most relevant topics covered in the next chapters and which we preface in the next sections, addressing to the fundamental questions posed in this thesis.

Spiral arms in galaxies represent regions of high concentration of gas (§ 1.1), thus of active star formation, where the atomic gas undergoes a rapid procession through the molecular phase, assembling in giant molecular clouds (GMC), whose collapse, facilitated by disk instabilities (§ 1.2), induces star formation. Star formation feedback could be propelling turbulent motions (§ 1.3) in the interstellar medium (ISM). Turbulence, in turn, could quench star formation, but at the same time could generate density waves which instead lead to star formation. It is not clear however at what level these processes are regulating each other. Possibly, the time scales for the assembly of these density waves and for stars to form (§ 1.4) is controlled by turbulent motions. A panoramic view over the properties of star formation at high spatial resolution is provided by nearby galaxies. For this scope, the optimal data set, that offers an integral view of the different phases of the ISM and stellar populations, is composed by a multi-wavelength mapping (§ 1.5).

We analyze high resolution tracers of gas and star formation for a sample of nearby galaxies (Chap. 2) in order to answer the following questions. What are the star formation time scales and efficiencies (Chap. 4)? Which aspects of the H I kinematics are not attributable to the galaxy gravitational potential? If we model the gravitationally induced orbital motions, and subtract these from the observed H I kinematics, do we evidence the signatures of feedback (Chap. 3)? How turbulent motions and star formation relate with each other? Is the turbulence in the ISM driven by star formation feedback (Chap. 5)?

1.1 Spiral Waves and Star Formation

Stars and gas in disk galaxies are organized in spiral structures whose morphology vary from galaxy to galaxy. The classic picture of spiral arm formation is explained in terms of density waves (Lin & Shu 1964). However, density waves are not likely to trigger significant star formation (Elmegreen & Elmegreen 1986). The concentration of blue stellar populations and H II regions near the spiral arms is only a consequence of the gas kinematics, since the gas happens to flow more slowly as it passes through the arms (Roberts 1969), so that star forming

regions appear to converge in the arms. If this ansatz is correct, in galaxies morphologically classified as flocculent and grand-design, the mechanism that triggers star formation must be the same (e.g. gravitational instability; § 1.2.1), while the difference between these two types of galaxies is only dictated by the strength of density waves. We will use these statements in Chap. 4 to show that the star formation time scales in spiral arms environment occupy a narrow range (1–4 Myr) for an heterogeneous sample of grand-design and flocculent galaxies.

1.1.1 Formation of Spiral Arms

B. Lindblad was the first who tackled the theory of spiral arms formation. He proposed that spiral structure arises from the interaction between the orbits and and the gravitational potential of the stars in the disk. If stars were arranged permanently in a spiral pattern the arm would, after a few galactic rotations, become increasingly curved and wind around the galaxy even tighter (winding problem). The originary idea was that spiral arms represent regions of density waves that rotate with a lower angular velocity than the material in the disk. As the gas enters a density wave, it undergoes to compression, and initiates star formation. However, we recall that more recent results conclude with a different view (e.g. Elmegreen & Elmegreen 1986).

Density Waves Theory

The density waves theory proposed by Lindblad was reexamined later by Lin & Shu (1964) who suggested a quasi-stationary spiral structure to explain that the pattern remains unchanged over many orbital times. They proposed that the spiral structure is a quasi-stationary density wave, attempting to explain the large scale structure of spirals in terms of a wave propagating in the disk with a constant kinematic pattern speed. Assuming that the stars lie on elliptical orbits and that the orientations of the lines of nodes of the orbits are slightly offset from each other, the elliptical orbits thread closer together in certain regions giving rise to the increase of density. The passage of the compression wave triggers star formation on the leading edge of the spiral arms. Lin-Shu theory provides a large number of predictions that have been confirmed by observations, e.g. the prevalence of trailing over leading spiral arms, and the prevalence of two-armed spirals. Moreover, in this scenario, combined with the fact that spiral arms are regions of active star formation, the spiral arms are predicted to be narrow. In fact, since O and B stars and H II regions have short life time (10^7 yr) compared with the galactic age (10^{10} yr), they can not drift too far away from their formation sites. Assuming reasonable values for the pattern speed and the angular velocity, the angular width $\Delta\theta = |\Omega - \Omega_p|\,\Delta t$ is typically $\sim 10^\circ$ (e.g. Roberts 1969). However, though the regularity of the symmetry is striking, Lin and Shu hypothesis of steady state spirals only well describes grand design spirals and breaks down for flocculent spirals, or for irregularities and patchiness even in grand design galaxies. These irregularities may be better explained by a smaller scale chaotic theory of spiral formation, where chaotic perturbations

on the local scale (less than a kiloparsec typically) will collapse into structures which will then be disrupted by shear.

Modifying the Density Wave Theory

The idea of the pattern speed can also be explained in terms of epicyclic motions. We will recall in Chap. 3 this basic idea, which was formulated for stars, and apply it to the gas kinematics with the appropriate conditions. An orbit viewed in a rest frame rotating with angular velocity Ω_p, appears closed if the frequency of the azimuthal and radial motions, Ω and κ, respectively, have integer ratio. In this case the pattern speed is $\Omega_p \simeq \Omega - n\kappa/m$. Lindblad noted that for the specific ratio $n/m = 2$, $\Omega - \kappa/2$ is nearly constant for most radii. Lin & Shu (1964) argued that the spiral gravity could force $\Omega - \kappa/2$ to remain constant, and for a given Ω_p the stellar orbits could be closed for a wide range of radii. As the material approaches the spiral arm, the gravity of the spiral arm pulls the material outward, slowing the speed of the orbit, and pulls the material after it has crossed the arm, speeding up the epicycle (see Roberts 1969).

Toomre (1969) noted that though the Lin-Shu dispersion relation for spiral waves the phase velocity equals the pattern speed, the group velocity instead causes the wave crests to move inward (see also Binney & Tremaine 1987). For a flat rotation curve Toomre showed quantitatively that the radial crest wavenumber increases during the time with a constant rate, and, consequently, the spiral pattern winds up since the arms get closer together. Therefore, the quasi-stationary density wave theory did not prove successful. This induced Toomre (1969) to propose that the spiral is a transient structure, that can be provoked by interactions. Toomre & Toomre (1972) modeled a system similar to M51, showing that tidal models adequately reproduce the observed features, and the transient character is due to the process of swing amplification (Toomre 1981).

Modal Theory

Bertin et al. (1989) describe the spiral modes as self-amplified wave trains. The maintenance of spiral modes may be considered in terms of oppositely propagating wave trains that satisfy a dispersion relation. The amplification mechanism for such modes is stimulated by coherent reflection near corotation (Mark 1976). In this terms, the wave amplification would be analogous to the laser mechanism, ensuing temporal growth of spiral modes. Another reflection mechanism origins from the central region of the galaxy, the bulge or the bar, so that the wave trains are in a closed loop. Therefore the spirals result as standing wave patterns. Modal theory finds support with the observation of coexisting and corotating $m = 2$ and $m = 3$ spirals (Elmegreen, Elmegreen, & Montenegro 1992). Most of $m = 2$ spirals are self-sustaining wave modes with inner wave reflections from bars inside the corotation, and the observed $m = 3$ spiral are wave modes driven by the $m = 2$ mode.

Numerical Approaches

Jeans instability (§ 1.2.1) is possibly responsible for the clouds and H II regions formation, and consequently for the formation of individual stars in disks. In this sense, numerical simulations intervene as a practical support to the theories exploring complicated problems like galaxy formation (e.g. Freeman 1970; Sellwood 1981; Fall & Efstathiou 1980). At early stages the gas is highly turbulent. Shocks that develop in supersonic flows are likely to compress gas and form Pop-II stars and globular clusters. The gas collapses into a rotating disk, with the inner parts forming before the outer, remaining turbulent during this phase. The feedback alters the dynamics by pressurizing the star-forming gas and stabilizing forming disks against fragmentation (Robertson et al. 2004). Instability quickly causes a fragmentation of the gas disk into clumps, which collapse under self-gravity and form stars on a short time scale. Recent simulations show that the Jeans instability promotes the formation of exponential disks (Bournaud, Elmegreen, & Elmegreen 2007). The mass redistribution, initially organized in massive clumps of gas, lasts for several orbital times, and evolves toward an exponential brightness profile. The fragmentation of unstable disks into clumps and the interactions between fragments accounts for the chaotic rotation curve, which evolves from irregular to flat, and the velocity dispersion goes from turbulent to relaxed. The presence of clumps conflicts with density wave theory, since density waves are not able to form clumpy spirals within a reasonable time scale. These results are supported by observations of irregular morphologies of galaxies at high redshift, $z \sim 1 - 2$, and their rotation curves (Förster-Schreiber et al. 2006; Genzel et al. 2006).

1.2 Disk Instabilities and Star Formation in Disk Galaxies

To better understand the star formation process, it is fundamental to study the formation and evolution of molecular clouds, which are the sites where this process takes place. Giant molecular associations mostly appear matching the spiral arms and the regions of active star formation (Wong & Blitz 2002; Engargiola et al. 2004). GMCs play a fundamental role in disk galaxy evolution by regulating the SFR. While the formation and growth of GMCs via collisional agglomeration of interstellar gas, giant H I clouds ($M \sim 10^7\ M_\odot$), seem to proceed too slowly (Elmegreen 1990, 1995), the growth of unstable modes is able to efficiently develop gas condensations. These instabilities mainly involve self-gravity, Coriolis force, shear due to differential rotation, and magnetic forces. The issue of disk instabilities will recur in this thesis several times. It is therefore essential to provide an overview over the factors that play a stabilizing and destabilizing role for cold gas in disk galaxies, hence regulate star formation.

1.2.1 Gravitational Instability

The gravitational instability, or Jeans instability, induces the collapse of interstellar gas clouds and is the key mechanism for ensuing star formation. The stability of a gas cloud is given by the hydrostatic equilibrium condition,

$$\frac{dp}{dr} = -\frac{G\rho M(r)}{r^2}, \tag{1.1}$$

which means that the enclosed cloud mass $M(r)$ is supported by the pressure p against gravity. The equilibrium is stable if small perturbation are damped, and unstable if they grow exponentially, causing the collapse.

Stability of Differentially Rotating Disks: Toomre Q

An important component in rotating disks is the centrifugal force, which tends, together with the pressure, to stabilize a compressed region against the collapse. Whether a disk is locally stable to axisymmetric perturbations can be determined using the dispersion relation for a gaseous disk (Binney & Tremaine 1987):

$$\omega^2 = \kappa^2 - 2\pi G\Sigma|k| + k^2 c_s^2, \tag{1.2}$$

where κ is the epicyclic frequency, Σ the mass surface density of the disk, $\lambda = 2\pi/k$ the size of the perturbation, and c_s^2 the sound speed. Since the right hand terms of the equation are real, also ω^2 must be real. If $\omega^2 > 0$, then the wave frequency ω is real and the amplitude of the perturbation has harmonic solutions, therefore the disk is stable, otherwise if $\omega^2 < 0$ the perturbation amplitude grows exponentially and the disk is unstable. The limit condition of stability is given by:

$$\kappa^2 - 2\pi G\Sigma|k| + k^2 c_s^2 = 0 \tag{1.3}$$

where positive solutions for $|k|$ exist if the condition

$$Q \equiv \frac{c_s \kappa}{\pi G\Sigma} > 1 \quad \text{(stable)} \tag{1.4}$$

is satisfied, that also corresponds to the stability criterion for a gaseous disk (Safronov 1960; Goldreich & Lynden-Bell 1965). Equivalently, Toomre (1964) derived the stability criterion for a stellar disk from a kinetic theory approach for a collisionless stellar system:

$$Q \equiv \frac{\sigma_r \kappa}{3.36 G\Sigma} > 1 \quad \text{(stable)}, \tag{1.5}$$

where σ_r is the radial velocity dispersion.

Schaye (2004) heuristically derived in terms of time scales the Toomre stability criterion for a rotating thin disk. If the gas responds to a perturbation of size λ more rapidly than the action of the gravity, or in other words, the sound crossing time $t_{\rm sc} = \lambda/c_{\rm s}$ is shorter than the collapse time scale $t_{\rm coll} = \sqrt{\lambda/G\Sigma}$, then the gas is stable. Therefore the stability requires a perturbation of size

$\lambda < c_{\rm s}^2/G\Sigma$. For a rotating disk the centrifugal force can also support against gravitational collapse. The perturbations are forced to rotate around their centers due to the Coriolis effect. If the collapse time scale $t_{\rm coll}$ is longer than the rotational period $t_{\rm rot} = 2\pi/\kappa$, then the perturbation is stable. Therefore, the stability a perturbation size $\lambda > 4\pi^2 G\Sigma/\kappa^2$. The gravitational instability regime will occur within the sizes regime of pressure and centrifugal support given by

$$\frac{c_{\rm s}^2}{G\Sigma} < \lambda < \frac{4\pi^2 G\Sigma}{\kappa^2} \quad \text{(unstable)}. \tag{1.6}$$

This condition yields

$$Q = \frac{c_{\rm s}\kappa}{2\pi G\Sigma} < 1 \quad \text{(unstable)}, \tag{1.7}$$

which is the Toomre criterion of Eq. 1.4 to within a factor of two. However, the formal derivation of the criterion (cf. Binney & Tremaine 1987) should include a linear analysis of the equations of motion of gas in a shearing disk.

In conclusion, the guideline for the interpretation of the Toomre-Q parameter is the following. (1) The Coriolis force, which is proportional to κ, contrasts the collapse. The epicyclic frequency is defined as $\kappa^2 \equiv 2\,(1+\alpha)\Omega^2$, where $\alpha \equiv d\log v_c/d\log r$ is the logarithmic derivative of the rotation curve. For a flat rotation curve $\alpha = 0$, and $\kappa = v_c/r$. Therefore faster rotators are more gravitationally stable. (2) The pressure, whose square root is proportional to the sound speed c_s, also provides support against collapse. It becomes clear in this terms that a turbulent environment, with high velocity dispersion, tends to resist the collapse. (3) If the mass surface density, which produces self-gravity ($G\,\Sigma$), reaches a critical value, can induce local collapse. This is possibly the case for the spiral arms, where the surface density is locally higher, the gravitational collapse is promoted finally ensuing star formation.

Shear

Schaye (2004) investigated whether the shear due to differential rotation, in addition to the Coriolis force, is able to prevent the gravitational collapse in rotating disks (Elmegreen 1993; Hunter, Elmegreen, & Baker 1998). If the Jeans time scale is longer than the shearing time scale, the perturbation is unable to grow, and the stability is achieved. The shear rate is given by Oort's constant A,

$$t_{\rm sh}^{-1} \sim |A| = \frac{1}{2}\,r\,\left|\frac{d\Omega}{dr}\right|. \tag{1.8}$$

The stability requires $t_{\rm sh} < t_J$, therefore $\lambda > G\Sigma/A^2$. This stability condition and the stability against gravitational collapse $\lambda < c_s^2/G\Sigma$ cannot both be satisfied if

$$Q_{\rm sh} = \frac{c_s A}{G\Sigma} < 1 \quad \text{(unstable)}. \tag{1.9}$$

The $Q_{\rm sh}$ parameter for shearing perturbations differs with the Toomre parameter of Eq. 1.4 by the factor πA replaced to κ. The critical condition in the $Q_{\rm sh}$

parameter has the same dependency with the velocity dispersion as Q. In the inner parts of galaxies the shear is low, because the rotation curve is similar to that of a solid body, consequently A can be much smaller than κ. In the outer part, the rotation curve is approximately flat, and in this limit $Q_{\rm sh} \simeq Q\,\pi/2 \simeq 1.11\,Q$. In conclusion, in both inner and outer parts the Coriolis force is always more important than shear for preventing the growth of perturbations.

1.2.2 Magneto-hydrodynamical Instabilities

Beside Jeans instability and rotational mechanisms like Coriolis force and shear, the galactic magnetic field plays an important role in condensation of interstellar gas. Parker instability, in which buoyancy induces the magnetic field to buckle and material to pile up in magnetic field valleys, and magneto-Jeans instability, which is efficient in low shear magnetized regions, and contrasts the stabilizing Coriolis effect, are both important in compressing the ISM and triggering the formation of GMCs as the gas orbits through the spiral arms. These classes of instabilities may act together with the gravitational instability in order to form the observed distribution of H II regions and OB associations in "beads on a string" pattern in spiral arms (Elmegreen & Elmegreen 1983).

Parker Instability

Parker (1966) showed that a horizontal (parallel to the galactic plane) magnetic field provides partial support against the vertical component of the galactic gravitational field. The medium is subject to a class of magnetic Rayleigh-Taylor[1] instability. Horizontal lines of field initially bend and induce the material to move toward the magnetic valleys. The material subsequently buoys upon the field lines forcing them to rise even higher, causing more material to be collected. The Parker instability may be one of the processes associated with the formation of gas clouds (Parker 1966; Mouschovias 1974; Blitz & Shu 1980) and, cooperating with thermal instability, of high density clumps (Kosiński & Hanasz 2007). Mouschovias, Shu, & Woodward (1974) argued that the Parker instability is triggered in spiral arms, behind spiral density shock waves, leading to the formation of large cloud complexes in valleys of curved magnetic field lines. However, Parker instability can not be accounted as the primary mechanism of GMC formation in galactic disks (Basu, Mouschovias, & Paleologou 1997; Kim et al. 1998; Kim, Ostriker, & Stone 2002).

Magneto-Rotational Instability – no Gravity

Regardless of gravity, the magneto-rotational instability (Balbus & Hawley 1991) arises when the angular velocity of a magnetized fluid decreases as function of the distance from the rotation center. A rotating fluid disk will remain in a

[1] In Rayleigh-Taylor instability a dense fluid is supported by the pressure of a thin fluid and drips downward through the less dense fluid.

laminar flow state if the angular momentum increases with radius (Rayleigh stability criterion). The stability condition is given by:

$$\frac{\partial \Omega^2}{\partial r} \geq 0 \quad \text{(stable)} \tag{1.10}$$

In a rotating fluid disk threaded by a weak axial magnetic field, two radially neighboring fluid elements are chained together by a magnetic field which enforces the corotation (by resisting shear), while the inner element orbits more rapidly than the outer, causing the magnetic field to stretch. The field forces the outer element to rotate too fast in the new radial location. When restoring forces are not able to compensate, displaced fluid elements are driven away from their equilibrium positions, leading to substantial angular momentum transport. Magneto-rotational instability with thermal instability maintain the velocity dispersion $\sim 1 - 3$ km s^{-1} in the midplane, and prevents gravitational instability in outer part of galaxy (Piontek & Ostriker 2007).

Magneto-Jeans Instability

In a rotating disk azimuthally threaded by a magnetic field the Magneto-Jeans instability (Elmegreen 1987; Kim et al. 2002) becomes important in low shear regime. In this picture the gas tends to condense by gravity, and is twisted by Coriolis force, resisting the contraction. Tension forces from azimuthal magnetic fields enfeeble the stabilizing Coriolis force. Kim et al. (2002) show, that Magneto-Jeans instability under weak shear in spiral arms is more effective than the Parker instability, and can form dense clumps within one orbital time.

Formation of Spurs via Gravitational Instability

Spiral arm perturbations may induce the formation and growth of smaller scales gaseous structures. H II regions and OB star associations are often observed along "beads on a string" pattern in spiral arms showing a quasi-regular series of dust lanes, with a separation of roughly 3 times (1–4 kpc) the full arm thickness, independent of pitch angle and galactocentric radius (Elmegreen & Elmegreen 1983). Elmegreen (1994) pointed out that this spacing of giant H II regions is due to gravitational collapse of magnetized gas. The spurs formation mechanism may as well include differential rotation, compression by the spiral pattern, self-gravity, and magnetic field. Low the surface density or strong shear can indeed prevent gas condensation on large scales.

Kim & Ostriker (2002) investigate, using MHD simulations, how such spurs could form and subsequently fragment from the interaction between interstellar gas and a stellar spiral arm. They show that the main flow shocks and compresses the ISM as it passes through a local tightly wound stellar spiral arm, and that spur structures rapidly emerge via magneto-Jeans mechanism. Subsequently the spurs undergo fragmentation to form massive clumps ($4\ 10^6$ M$_\odot$), which may evolve into bright arm and interarm H II regions.

1.2.3 Star Formation Triggering

Star formation may in part result from spontaneous gravitational cloud formation, but could in part also be triggered by the compression of existing clouds. Local star formation can proceed from self-propagating stochastic star formation (Gerola & Seiden 1978; Seiden & Gerola 1982). The basic idea is that, initially, shock waves induced by SNe accelerate the ISM (Mueller & Arnett 1976), and, subsequently, expanding H I shells slow down to an expansion velocity comparable to velocity dispersion of environment. In this phase, the expanding shell may have accumulated enough matter that can become Jeans-unstable and collapse. For example, the creation of holes and shells in the ISM is commonly attributed to feedback from massive stars, stellar winds, and SNe (Tenorio-Tagle & Bodenheimer 1988). Alternative scenarios include high-velocity cloud impacts, disk instabilities, turbulence, and ram pressure stripping (Sánchez-Salcedo 2002). In normal disks, holes and shells are dissipated by turbulent motions and rotational shear on time scales of 10^7 yr. However, in dwarf galaxies the shear effect is minor, since their rotation curve is that of a solid body. Yet, nearby dwarf galaxies show a large number of holes in the ISM (Walter 1999; Walter & Brinks 1999). Starburst regions and sites of massive star cluster formation in the center of shells are able to provide on short time scales spatially concentrated feedback, and likely to origin these shells and trigger star formation on their edges (Cannon et al. 2005). With numerical simulations Gritschneder et al. (2006) showed that ionizing radiation of H II regions and O-B stars interact with the turbulent medium and can trigger the collapse of an otherwise stable molecular cloud and substantial star formation.

Star formation does not occur necessarily in every location where the gas is dense, but primarily in self-gravitating cloud cores, which correspond only to a small mass fraction of the cloud. Even so, dense cloud clumps are generally stable and unable to form stars due to turbulence compression. Turbulence gives structure to gas and star formation. Elmegreen (2000) showed that there exists a correlation between the size of star forming regions – cloud diameter – and the crossing time – obtained by dividing the size by the internal velocity dispersion. The same correlation is found between age separation and distance separation for the Large Magellanic Cloud (LMC) star clusters (Efremov & Elmegreen 1998). The fact that star formation regions share the same size-time correlation as the turbulent ISM, suggests that positions of young stars and timing for star formation are hierarchical, and in each region the star formation process must last about one or two crossing times. Turbulence is predicted to decay in a short time (Stone, Ostriker, & Gammie 1998; Mac Low et al. 1998). If the formation of stars occurs in only few (turbulent) crossing times, cloud lifetimes are short and the existence of a mechanism sustaining turbulence (e.g. energy feedback) is not needed.

1.2.4 Star Formation Laws

The consumption rate of gas converted into forming stars strongly influences the galaxy evolution. The process of star formation occurs at several regimes of rates globally for different types of galaxies and locally in individual galaxies. Although, star formation follows two simple empirical laws: (1) the SFR is a power law of the gas density, and (2) star formation is efficient above a critical surface density. The existence of these two laws suggests that star formation might be mostly regulated by gravitational instability.

Kennicutt-Schmidt Law

The universality of the empirical correlation between the SFR and the average gas surface density is one of the galaxy properties that so far has not been well understood. On scales as small as individual clouds ($\sim 10-100$ pc), star formation process appears to be rather stochastic and difficult to model (Hartmann 2002), whilst on kiloparsec scales star formation appears more regular. Schmidt (1959) originally proposed that the SFR scales as a power-law of the gas volume density. Kennicutt (1989) empirically found that star formation is regulated by the general correlation between SFR and gas surface density normalized over the stellar disk area:

$$\Sigma_{\rm SFR} \propto \Sigma_{\rm gas}^{1.4}, \tag{1.11}$$

where the gas surface density takes in account both neutral and molecular gas (H I, H_2, and He) averaged over a large scale (kiloparsec). The global star formation law is found to be shared by a wide range of galaxy types, beside normal galaxies, including starbursts (Kennicutt 1998) and dwarfs (Leroy et al. 2005). More recently, Kennicutt et al. (2007) found that star formation in M51 follows the same global power law also on local scales of individual GMC complexes ($300-1850$ pc). The existence of a star formation law that holds from galactic scales down to sub-kiloparsec scales raises the natural question whether it is possible to define a spatially resolved relation. The larger is the aperture the more the biases are indeed reduced, but the problem is that SFR and gas surface densities vary locally by orders of magnitude and the actual measurements may be aperture dependent.

Star Formation Threshold

Soon after that Toomre (1964), and Goldreich & Lynden-Bell (1965) had developed the local stability criteria for rotating disks, Spitzer (1968) and Quirk (1972) proposed that the gravitational instability is able to determine a gas density threshold for star formation. Given that a thin rotating gas disk is unstable to axisymmetric perturbations if the Toomre parameter,

$$Q = \frac{\sigma\kappa}{\pi G\Sigma} \tag{1.12}$$

is less than unity, the local collapse and subsequent onset of star formation is expected where the gas surface density exceeds the critical surface density

defined as

$$\Sigma_{\rm crit} = \alpha \frac{\sigma \kappa}{\pi G}, \tag{1.13}$$

where $\alpha \equiv \Sigma_{\rm gas}/\Sigma_{\rm crit}$, and the epicyclic frequency κ, the velocity dispersion σ and the surface density $\Sigma_{\rm gas}$ are functions of galactocentric radius. According to Silk (1997), the velocity dispersion remains roughly constant in self-regulated regions of disks, and a lower limit might be set by MHD-driven turbulence in the outer disk (Sellwood & Balbus 1999). Assuming that the velocity dispersion does not vary much with radius across a spiral galaxy, then the critical surface density is $\Sigma_{\rm crit} \propto \kappa$, where for a flat rotation curve $\kappa \propto 1/R$, so that $\Sigma_{\rm crit}$ falls roughly as R^{-1}. Therefore, if the total gas surface density profile has steeper decline than the critical surface density, there exists a threshold radius where the gas surface density becomes sub-critical, in other words the is gas unable to collapse. In these circumstances, gravitational instability provides an explanation for the rather sharp cutoff of most stellar disks.

The distribution of Hα emission in disk galaxies, accordingly with the observations, shows that the radial SFR profile drops abruptly at a few disk scale lengths. Kennicutt (1989) and Martin & Kennicutt (2001) investigated how the observed cutoff in the SFR is related to the Toomre-Q parameter, which would be expected to equal the unity at the threshold radius. Assuming a constant gas velocity dispersion of 6 km s^{-1}, they found that $\alpha \equiv 1/Q \simeq 0.5$ at the threshold radius for a sample of nearby spiral galaxies. Hunter et al. (1998), using a different velocity dispersion, found instead $\alpha \simeq 0.25$. The velocity dispersion assumed by Hunter et al. if scaled to 6 km s^{-1} would yield a value for α more consistent with Kennicutt's results. However, the assumption of a constant velocity dispersion is questionable[2].

What Regulates Star Formation Laws

The Kennicutt-Schmidt law depends on the assumption of the global constance of parameters that instead may locally vary, like H_2 to CO conversion, extinction, velocity dispersion, stellar mass, etc. The slope of the law varies in fact from 1.2 to 3 in different studies. Kennicutt threshold may also require the influence of stars, beside gas, and the effect of shear.

First, in order to calculate the molecular gas mass in nearby galaxies, the ^{12}CO(1-0) intensity line is used with an adopted X conversion factor between I(CO) and N(H_2) measured in the solar neighborhood. Boselli, Lequeux, & Gavazzi (2002) question the universality of the X conversion factor, which may depend on metalicity, cosmic ray density and UV radiation field. Kennicutt's law assumes instead a constant conversion factor for estimating the total gas surface density H I + H_2.

[2] Formally, the Toomre Q parameter is expressed in terms of sound speed, whilst most studies are based on the measured velocity dispersion, which is depends on the sound speed as $\sigma = c_s \gamma^{-1/2}$ if the velocity dispersion is not dominated by turbulence, where the adiabatic index $\gamma = 5/3$ for a monoatomic gas and $\gamma = 7/5$ for a diatomic gas.

Second, Wong & Blitz (2002) suggest that Toomre-Q parameter is not a reliable indicator of SFR, but rather a measure of the gas fraction. The stellar surface density component to the disk instability should not be neglected (see also Wang & Silk 1994). In fact, high Q values generally correspond with low $\Sigma_{\rm gas}/\Sigma_{\rm tot}$ fraction. Boissier et al. (2003) found that galaxies with ongoing star formation are instead sub-critical in terms of Q parameter for pure gas. Thilker et al. (2007) recently showed that substantial UV emission from young stars is observed far beyond the classical threshold. Jog & Solomon (1984) and, more recently, Li, Mac Low, & Klessen (2005, 2006) found that a disk composed of gas and stars is more unstable in terms of Toomre-Q parameter than either component considered individually. Both gaseous and stellar component can account to the growth of density perturbation, facilitating the collapse. The instability condition is expressed by

$$2\pi G k \left(\frac{\Sigma_{\rm star}}{\kappa^2 + k^2 c_{s,\,\rm star}^2} + \frac{\Sigma_{\rm gas}}{\kappa^2 + k^2 c_{s,\,\rm gas}^2} \right) > 1 \quad \text{(unstable)}, \tag{1.14}$$

where $\lambda = 2\pi/k$ is the wavelength of the perturbation.

Last, the influence of shear by differential rotation, which Schaye (2004) argued less effective compared to the Coriolis force in stabilizing the disk, has instead been proven important in some case studies. Luna et al. (2006) observe that molecular gas motion within the Milky Way arms locally resembles that of a solid body, with constant angular velocity. The massive star formation in the arms is regulated by low shear and is consistent the Kennicutt-Schmidt law. Using numerical simulations, Vorobyov (2003) explained the low SFR in the inner regions of the Cartwheel ring galaxy in terms of high shear, which can suppress formation of massive stars, where the Toomre criterion for star formation can not account for the observed sharp drop of young stellar associations.

In conclusion, the sharp cutoff in the stellar surface density, suggests the existence of a star formation threshold. Kennicutt (1989) and Martin & Kennicutt (2001) have demonstrated that the Toomre criterion generally can explain this truncation, although they must introduce a correction factor α to the Toomre parameter, with $\alpha \simeq 0.5$ accounting for the use of velocity dispersion rather than sound speed (Schaye 2004). The Toomre instability criterion must be modified in order to include the shear support, the effects of magnetic field and, more importantly, the contribution of the stellar gravitational potential, which may alone explain the correction factors found by Kennicutt (1989) and Martin & Kennicutt (2001). In addition, the temperature of the cold phase and the velocity dispersion can also play a role for the onset of gravitational instability (Mac Low & Klessen 2004). Differences in the assumptions of these variables modify the instability criterion, and therefore vary the star formation thresholds.

1.3 Turbulence and Feedback

We provide here an overview over the turbulence in the ISM and the star formation feedback as a possible driving source. We will address our results on this issue in Chap. 5 (see also § 1.6).

Turbulence in the ISM plays a dual role, maintaining a pressure support on global scales and inducing collapse locally (Mac Low & Klessen 2004). On the one hand, stochastic motions can produce high gas density enhancements. The ram pressure forces large regions of dispersed gas to assemble into a network of dense filaments (Klessen et al. 2004). In regions, where the density is sufficiently high to ensue the condition of gravitational instability, the collapse of small scale structures is set on. On the other hand, the turbulence acts against the collapse, and is able to dissipate density enhancements before they can collapse, preventing ultimately the gas clouds to form stars. In this aspect, the turbulence regulates the efficiency of star formation, by determining the balance between the pressure support and the local density. This balance depends on the driving scale lengths of turbulence and the scale lengths of the gravitational forces, respectively. In fact, while turbulence supports against the collapse globally, it may still favor the collapse locally (Klessen, Burkert, & Bate 1998; Klessen, Heitsch, & Mac Low 2000; Heitsch, Mac Low, & Klessen 2001). Star formation is regulated on a large range of spatial scales, and depends on the parental gas cloud conditions. Star formation is apparently inefficient where the turbulence prevents the collapse, and occurs exclusively on small fragmentation enough dense to undergo the collapse. Regions of Jeans-unstable gas collapse on a relatively short time scale, about a free-fall time, and tend naturally to form stars efficiently and rapidly. In fact, while turbulence supports against the collapse globally, it may still favor the collapse locally.

1.3.1 Kolmogorov Turbulence Regime

The heuristic prescription formulated by Kolmogorov (1941) works well in delineating the dynamics of an incompressible fluid in a turbulent condition. Turbulence can be described by a hierarchy of eddies of a wide range of scale sizes going from the largest scale $\lambda_{\rm max}$, the size at which the turbulence is driven, to the dissipation scale $\lambda_{\rm visc}$. Interacting eddies tend to subdivide into smaller eddies, producing therefore a cascade mechanism of energy transfer from larger to smaller eddies down to the smallest scale $\lambda_{\rm visc}$. The energy transfer from each scale to the next occurs at a rate $\dot{E} \propto v^3/\lambda_{\rm max}$, which implies that the kinetic energy distribution $E \propto v^2 \propto k^{-11/3}$ is a power law of the eddies sizes $k = 2\pi/\lambda$.

Supersonic turbulence in molecular clouds decays in a relatively short time, less than a free-fall time (Stone et al. 1998; Mac Low et al. 1998). Since the whole process of cascade energy transfer is highly dissipative, a mechanism that supplies energy is needed in order to sustain the turbulence in a steady state. Motions that involve gas compression and form molecular clouds, e.g. gravitational collapse and magneto-hydrodynamic waves may provide this energy

injection (Ballesteros-Paredes, Hartmann, & Vázquez-Semadeni 1999).

1.3.2 Hierarchical Structures in the ISM

Kolmogorov scaling law appears to adequately describe the turbulence in the ISM, though this theory applies to the dynamics of incompressible gas and the actual interstellar gas is instead compressible. The existence of a power-law distribution of sizes of the eddies denotes a hierarchy in the turbulent structures. Spatially, the ISM displays a similar mode of behavior. Diverse techniques of pattern study, e.g. fractal analysis (Feitzinger & Galinski 1987; Battinelli, Efremov, & Magnier 1996; Elmegreen & Salzer 1999; Pietrzyński et al. 2001), unsharp masks (Elmegreen & Elmegreen 2001), and auto-correlation functions (Harris & Zaritsky 1999; Zhang, Fall, & Whitmore 2001) reveal that the ISM and regions of star formation distribute in a hierarchical network, where self-similar structures have sizes that range from the Nyquist resolution, including sub-parsec scales in the solar neighborhood (Testi et al. 2000) up to a few kpc scales in external galaxies. These hierarchical patterns only manifest in star forming regions younger than a crossing time (Elmegreen 2000), before random motions disrupt the geometric structure of emerging newborn stars.

The sizes distribution of H I emission in the LMC is approximately a power law over two decades in length (Elmegreen, Kim, & Staveley-Smith 2001). Fractal structure of interstellar gas, both atomic and molecular is also observed in other external galaxies (Elmegreen & Falgarone 1996; Westpfahl et al. 1999). Similarly, star formation patches both in flocculent and grand-design galaxies also display structures with a nearly Kolmogorov scaling law distribution of sizes (Elmegreen, Elmegreen, & Leitner 2003). The sizes of these regions are comparable to the critical Jeans length, indicating that they may have been generated by gravitational instabilities and disrupted by rotational shear, forming subsequently flocculent spiral arms. This mechanism produces supersonic turbulence, which cascades into a hierarchy of sizes of gas clouds and star formation patches. In fact, the existence of such kinematic and spatial hierarchy is possibly caused by turbulence, as also shown by numerical simulations (Klessen, Heitsch, & Mac Low 2000; Ossenkopf, Klessen, & Heitsch 2001). Given that interstellar gas and star forming regions possess similar structures, and exhibit the same correlation between crossing-time and spatial separation, it suggests that young stars and gas proceed in a coherent pattern limited by local random flows and cloud lifetime (Efremov & Elmegreen 1998; Ballesteros-Paredes et al. 1999).

Turbulence in the ISM can origin from a combination of spiral instabilities acting on several scales. Spiral gravitational and magnetic instabilities, swing-amplifier, and shear act pervasively. On large scale they can generate turbulence (Toomre & Kalnajs 1991; Sellwood & Balbus 1999; Wada, Meurer, & Norman 2002) and drive the dynamics of clouds, acting as cold and supersonic pressure gradients. Magnetic instabilities generally are not able to produce dense structures, and gravitational energy rapidly dissipates by radiation, and, in order to sustain turbulence, the energy input must be continuous. Shear and stars

are likely to replenish the turbulence energy. However, shear is less effective on smaller scales – clouds resist to tidal forces (Vázquez-Semadeni & García 2001). On scales of individual clouds, stellar energy ionizes and heats the surrounding gas, and, on larger scales, provides internal energy to the gas clouds to resist against collapse, maintaining the ISM in a steady state of Kolmogorov regime.

Noteworthily, star forming regions in grand-design galaxies exhibit the same intrinsic geometry as flocculent galaxies, suggesting that star formation is not triggered by stellar spiral waves, but rather by stochastic density enhancements induced by turbulent spiral instabilities (Elmegreen, Elmegreen, & Leitner 2003). In this aspect, the star formation process has identic character in both grand-design and flocculent galaxies, since the ISM and the emerging young stellar associations set in a coherent pattern developed by turbulent motions.

1.3.3 What Drives Turbulence

The turbulent character of the ISM could not last in a metastable regime, it would decay on a short time scale that is comparable to the turbulent crossing-time (Elmegreen 2000), unless it is renewed by a continuous injection of energy, providing thereby support against the gravitational collapse (Mac Low & Klessen 2004). Hereafter, some of the possible mechanisms that could drive turbulence are enumerated.

Magneto-Rotational Instabilities

Rotational shear is able to supply energy to the turbulence in the ISM on large scales (Fleck 1981; Schaye 2004). Magneto-rotational instabilities in the disk (e.g. Balbus & Hawley 1991) could efficiently transfer energy from the shear down to smaller scales into turbulent motions. According to Sellwood & Balbus (1999), a typical value of magnetic field of 3 μG for an average density of $\rho = 10^{-24}$ g cm^{-3} could well be able to maintain a turbulent field at about 6 km s^{-1}. Therefore, the measured regime of velocity dispersion in disk galaxies may in part be accounted to magneto-rotational instabilities.

Gravitational Instabilities

The stellar spiral wave can induces, beside gravitational compression and triggers of star formation (Lin & Shu 1964), also shocks in the gas flowing across the arms (Roberts 1969). In galaxies with prominent spiral perturbations, at the position of the shocks, the gas moves almost perpendicularly to the disk plane into the arms (Gómez & Cox 2002). The vertical gas flows reach velocities of about 20 km s^{-1}, and part of the interstellar turbulence can be accounted to these flows. However, since interstellar turbulence is observed also in the outskirts of disk galaxies, where the surface density is low, and in galaxies without prominent spiral arms, turbulence cannot be driven only by this process. Furthermore, Wada, Spaans, & Kim (2000) found that the the coupling between rotational shear and gravitation provides an energy input by two orders

of magnitude lower than the energy needed to sustain the observed regime of turbulence.

Protostellar Outflows

Energetic jets and outflows can be produced by protostars and stellar accretion phenomena, but their released power seems inefficient as a mechanism of energy injection, since jets and winds can provide energy only into low density gas regions (Henning 1989). Turbulent motions are observed on scales comparable to the sizes of molecular clouds, and on such large scales embedded protostars are not able to drive turbulence (Ossenkopf & Mac Low 2002).

Massive Stars

Massive stars provide various mechanisms of energy feedback: winds, radiation, and they ultimately end up into type-II SNe. The most massive stars undergo to intensive mass loss during their evolution. The total energy deposit by the winds of a main sequence star of type O is comparable to the energy of its SN explosion, and the winds of a Wolf-Rayet star are even stronger (Mac Low & Klessen 2004). However, the number of O type stars only corresponds to a small fraction of the total number of stars that terminate their evolution into SNe. Moreover, the intensity of the stellar winds strongly decreases for lower luminosities. It is therefore clear that the energy release of SN explosions dominate over the winds of the most massive stars.

The strong UV flux from O and B stars ionizes and heats the gas up to $\sim 10^4$ K. This process still injects less power into the ISM than SNe. The ionizing radiation also drives supersonic expansion of H II regions. The radiation energy is inverted into raising the pressure and temperature of the diffuse gas, but does not account for maintaining the turbulence. Supersonic flows of expanding H II regions are effective near young clusters and can quench star formation only on small scales.

Supernovae

SN-driven turbulence can in part inhibit cloud collapse, but without completely preventing star formation (Joung & Mac Low 2006). Though SNe explosions regulate turbulence on large scales, Dib & Burkert (2005) found that this mechanism can not account for the turbulent H I motions observed in Ho II, where the required scale of energy injection must be of ~ 6 kpc, which is much larger than the scale implied by SN driving. SN feedback contributes to the velocity dispersion of ~ 3 km s^{-1} for the H I, and, seemingly, depends on the SN rate weakly (Dib, Bell, & Burkert 2006). There is an obvious correlation between SFR – therefore the number of O-B stars – and SN rate. The gas velocity dispersion also appears to fairly correlate with these parameters. However, while this scenario is compatible with turbulence being driven by SN feedback, it is also compatible with stochastic motions inducing star formation via density enhancements. In this aspect, the origin of such relation is still matter of study.

Cloud Infall

The H I transonic turbulence could be maintained by continuous infall of gas clouds onto H I disks (Santillán, Sánchez-Salcedo, & Franco 2007). This mechanism could account for a H I velocity dispersion of about 6.5 km s^{-1}. Therefore, unless there exists an efficient mechanism of gas transport to high galactic altitudes, an extragalactic replenishment of gas that continuously falls onto the disk seems unrealistic. In this scenario, SNe and stellar winds must be able produce gas outflows perpendicular to the galactic plane. Then, supershells bursting out of the disk can eventually fall back to the disk (e.g. Norman & Ikeuchi 1989).

Random Motions

Wada et al. (2002) suggest that the large scale galactic rotation couples with the small scale kinematics of the gas, and maintains the turbulent regime of the ISM. Their numerical approach show that the gas velocity field sets on a quasi-steady state, where a fully developed turbulence follows a Kolmogorov scaling law over 3 decades of wavenumber. The main energy sources are associated to rotational shear, local tidal forces due to self-gravity of the gas, and, as long as the ISM is not in pressure equilibrium, local pressure gradients. This scenario depicts turbulence in the ISM as an effect only due to the random velocity field.

1.4 Time scales for Star Formation

A fundamental issue in the star formation theory lies in understanding how rapidly young star clusters emerge after the molecular clouds assembling and collapse, and at which rate the total gas reservoir in galaxies is consumpted in order to form stars. We address our analysis and results on this specific issue in Chap. 4 (see also § 1.6). The estimate of the time scales for star formation are subject of controversy, though. If this time scale is longer than the dynamical time of the parent gas clouds, then there is a predominance of the processes that delay or prevent the star formation or the cloud collapse. Contrarily, if this time scale is comparable to the dynamical time, then star formation must proceeds as fast as physically possible.

Observational results of the past decades estimated time scales for star formation as long as $\sim 10^8 - 10^9$ yrs (Zuckerman & Evans 1974; Scoville & Solomon 1975; Solomon, Sanders, & Scoville 1979), and from 10 to 30 Myr for the GMC lifetimes (Bash, Green, & Peters 1977; Leisawitz, Bash, & Thaddeus 1989). More recently, these time scales turn out to be lower than previously observed by a factor of ~ 10, with various workers finding time scales as short as few Myr (Hartmann, Ballesteros-Paredes, & Bergin 2001; Onishi et al. 2002; Hartmann 2003; Egusa, Sofue, & Nakanishi 2004; Vázquez-Semadeni et al. 2005; Ballesteros-Paredes & Hartma 2007), although the lifetimes of the GMCs in the LMC still appear to be longer, i.e. $\sim 10 - 30$ Myr (Fukui 2007; Kawamura et al. 2007; Blitz et al. 2007). The classical theory of long lasting and quiescent molecular clouds (Blitz & Shu 1980), has been recently reviewed in a light where clouds are instead transient

and short-lived (Ballesteros-Paredes et al. 1999; Elmegreen 2000). GMCs typically exhibit super-critical masses, and should, in principle, efficiently form stars on a dynamical time, say in 1-10 Myr, depending on their mass and size. If stars form in only one dynamical time, it suggests that several processes promote a rapid collapse (Elmegreen 2007). Observations also suggest that stars do not form in one monolithic event, but rather in fragmented sub-regions of parent clouds, which appear dynamically stable (Williams, Blitz, & McKee 2000).

1.4.1 Rapid Star Formation: Implications

Why does it Occur?

The basic idea is that the clouds and the interstellar turbulence are formed simultaneously and at the same place, resulting therefore both as transient entities, limited by the local crossing time (Ballesteros-Paredes, Vázquez-Semadeni, & Scalo 1999; Ballesteros-Paredes et al. 2007). Subsequently, clouds are destroyed shortly after that stars are formed (Fukui et al. 1999; Yamaguchi et al. 2001), before turbulence decays. This picture is in opposition with the previously envisioned view (e.g. Zuckerman & Evans 1974), where clouds were thought to be long-lived and supported by supersonic turbulence.

Rapid star formation occurs when the processes that lead to the formation of molecular clouds, e.g. self-gravity, density fluctuations and shocks, spiral instabilities and random motions, operate on time scales comparable to the crossing time of the turbulent motions. These processes act reasonably close to the dynamical time, $t_d \sim (G\rho)^{-1/2}$, and more rapidly at higher gas densities. In other words, globally, the clouds appear in pressure equilibrium, supported by the supersonic turbulence, displaying long dynamical times, but star formation takes place only in the densest and localized sub-regions on short time scales.

Rapid Star Formation Implies Low SFE

Recent observations evidenced that molecular clouds are not in virial equilibrium and that star formation proceeds quickly (cf. Mac Low & Klessen 2004; Ballesteros-Paredes 2006; Ballesteros-Paredes et al. 2007), modifying the paradoxal picture where GMCs are meta-stable systems and slowly evolving, and where most of their mass has a dynamical time – and life time – longer than the time scale for star formation. This implies that star formation is inefficient in molecular clouds. In fact, only a small fraction, typically $\sim 10\%$, of the mass of a GMC is converted into stars (Williams & McKee 1997). The SFE can be even controlled and reduced by the stellar feedback, which destroys molecules and drives turbulence in the medium (Williams & McKee 1997; Matzner & McKee 2000; Nakamura & Li 2005). The process where star formation is active involves only the cores (e.g., the HCN cores), while the envelopes, evolving more slowly, display no star formation (Polk et al. 1988). Efficiencies as high as 30% to 50% can be found in denser sub-cores (e.g., the CS cores) with low total mass, and which form individual stars (Shirley et al. 2003). Therefore, observational

results suggest that SFE increases in hierarchical fashion towards smaller and smaller structures. Moreover, provided that the efficiency is low, since only a small fraction of molecular clouds mass form stars, then the consumption time of the gas reservoir is long.

End of Cloud Life Cycle

After the onset of star formation, three processes are involved in the dissipation of molecular clouds: destruction, dispersal, and consumption, but only the first two are determinant for quenching star formation and setting an end to the life cycle of molecular clouds. The cloud destruction, where molecules are converted back into atomic form through ionization and heating, operates on long time scales, since ionization only destroys $\sim 10 - 20\%$ of the total cloud mass. The cloud dispersal, which is mainly due to turbulent motions, is instead faster, acting on time scales comparable to the dynamical time, and it does not require the occurrence of star formation as for the case of destruction via ionization. The consumption time is the longest, since the SFE is low, and consequently a small fraction of the gas reservoir is consumpted. In conclusion, molecular clouds are formed quickly, e.g. by random density fluctuations, and dispersed by the same processes that formed them and on the same time scales. Ultimately, they will exist as long as they undergo destruction through stellar feedback. Their gas reservoir consumption does not correspond to any limit to their life cycle (Elmegreen 2007).

Hierarchical Structures

The hierarchical nature of the spatial distribution of neutral and molecular interstellar gas and young stellar populations (Westpfahl 1999; Stutzki et al. 1998; Efremov & Elmegreen 1998; Dickey et al. 2001; Elmegreen et al. 2001) needs the correct interpretation, since sampling and resolution limits could in principle introduce selection effects on observational results. Recent studies have revealed that evolutionary time scales, e.g. cloud life times, are shorter than what earlier observations implied. If the formation and the dispersal of structures is related to the crossing time of local turbulent motions, then the dynamical time varies as function of the local scale size. Consequently, the improvement in the accuracy of observational techniques enables the possibility to observe smaller and smaller structures, which are evolving more rapidly, and provides therefore shorter time scales.

The sizes of the structures of active star formation, however, are not representative of the time scales there involved. While stellar activity itself causes the destruction of the parent cloud, turbulence causes the cloud dispersal. These effects limit therefore the life time of GMCs, which ranges between 10 to 20 Myr, and drops by almost a factor of ~ 10 for the star forming active cores. As an additional consequence of these self-dissipating effects, star formation begins at high rate in only a few Myr, appearing in large organized structures – beads on a string – of few hundred pc scales (Efremov 1995; Elmegreen 2007), and it

remains active for a long time, $\sim 30 - 50$ My, but with a gradually decreasing star forming rate, until the complete quenching. In conclusion, since star formation is organized in a hierarchical fashion both in time and in space, where across regions as large as GMCs several episodes of star formation occurs in O-B complexes on small and uncorrelated scales, the correct interpretation of the time scales might strongly depend on the considered scale sizes.

1.5 Multi-Band Studies

An empirical assessment of the physical state and spatial distribution of various gas phases, dust and stellar populations is possible only trough multi-wavelength observations. While stars are relatively simple systems, considering that most of their emitted radiation limited in the near-IR to optical/UV, gas and dust are much more complex features, presenting a large variety of properties, which are observable from the radio up to γ-ray regime both in emission and in absorption. Recent advances in observing capabilities have opened up the field dramatically, as we show with the outcoming results of this thesis, which are in fact based on the analysis of a multi-wavelength mapping of nearby galaxies (Chap. 2).

1.5.1 Radio/sub-mm Emission

Radio Continuum

In normal galaxies, two different emissions are present in the decimeter regime of wavelengths: the synchrotron (non-thermal) emission associated with cosmic rays, and the free-free thermal emission from hot ionized gas.

In star forming regions, shock waves and magnetic fields in SNe shells propagating in the ISM accelerate charged particles, mostly protons (90%), α-particles (9%), and electrons (1%), up to energies of $10-10^5$ GeV, and generates therefore a flux of cosmic rays pervading the ISM. High energy electrons, spiraling around magnetic field lines, emit synchrotron radiation. This non-thermal emission associated with cosmic rays dominates the radio continuum. The total amount of energy contained in the flux of cosmic rays, decays on short time scales, while propagating through the ISM via winds or diffusion. Therefore, a mechanism of energy replenishment is needed in order to balance the energy losses. There exists a strong correlation between dust continuum emission and the non-thermal radio luminosity, suggesting that part of the energy released by massive stars and SN remnants is transferred to the cosmic rays. In this logic, the non-thermal emission can be regarded as indicator of massive star formation.

The intense UV radiation provided by O and B stars heats and ionizes the surrounding gas, producing H II regions. The free-free emission (bremsstrahlung) from the hot (10^4 K) ionized gas in thermal equilibrium characterizes the radio continuum in the decimeter-centimeter wavelengths. H II regions are relatively compact (few tens of pc) and considerably bright regions. Ionized gas as traced by radio continuum, as well as by hydrogen emission lines in the optical/near-IR (e.g. Balmer or Paschen lines), is a straightforward indicator of star formation

activity, and since this wavelength range is unaffected by extinction, the hot gas emission serves not only to determine the extinction by comparison with Hα observations, but also to measure temperature and density of the hot gas.

The 21 cm Hydrogen Line

In its ground level, the atomic neutral hydrogen has two possible states: a higher energy state, with parallel spins configurations, and a lower state, with antiparallel spins. Collisions allow to populate the upper level, and the transition to the lower state produces the emission of a photon at 21 cm wavelength (1.4 GHz frequency). The transition is forbidden, since the half-life of the decay is $\sim 1.1 \times 10^7$ years, but the line is easily observable due to the large number of hydrogen atoms in the ISM. Being the potential fuel for the formation of molecular clouds, the neutral atomic hydrogen plays a fundamental role in star formation. Therefore, the overall content of H I may well determine galaxy types and their evolution. Observations of the Milky Way and of external galaxies accordingly exhibit evidence that most of H I emission is connected to star forming regions as demonstrated by the correlation between H I emission and other star formation tracers e.g. Hα or dust emission.

Molecular Hydrogen

Most of the ISM is composed by both neutral and molecular hydrogen, where the H_2 is the most abundant molecule in the ISM. Therefore, combining H I and H_2 emissions provides a measurement of the overall gas content. The presence of the H_2 molecule is observationally correlated to star formation, being the fundamental constituent connected to the formation of GMCs. While the H I gas is more diffuse, molecular gas concentrates in giant clouds of $\sim 10^5 - 10^6$ $M_\odot$ enclosed in a few hundred parsecs. GMCs, in turn, exhibit high degree of inhomogeneities and substructures: clumps of $\sim 10^3$ $M_\odot$ mass, and cores of few $M_\odot$ and ~ 0.1 pc size – the sites where stellar clusters and individual stars form, respectively.

Despite the high H_2 abundance, the rotational and vibrational emissions of this molecule at mm wavelengths are difficult to observe. The H_2 molecule is in fact a symmetric rotor and has no permanent dipole moment. Moreover, the ground level can be observed only in the UV or in absorption, which requires a background source, and consequently precludes the observation of high column density regions like GMCs. In place of the H_2 molecule, observations in the mm wavelengths commonly rely on the CO molecule, whose fundamental rotational transition ($J = 1 \rightarrow 0$) produces a photon at 2.6 mm. Most of our understanding on the properties of GMCs avails in fact on observations in the CO bands, used as tracer of the molecular gas.

1.5.2 Mid- and Far-Infrared

The IR range between ~ 1 μm and ~ 600 μm wavelengths of star forming regions of spiral and irregular galaxies is dominated by the dust re-radiation of absorbed UV light emitted by young hot stars. Elliptical galaxies, in turn, have a low dust content and are mostly populated by red and old stars, consequently they also exhibit faint emission at these wavelengths. The process of dust heating is more efficient in the blue/UV regime, since the dust grains have characteristic sizes comparable to the wavelengths of the photons interacting with the dust. By cooling, the grains radiate a quasi-blackbody emission spectrum. The typical temperature of the dust thermal emission peaks at $\sim 20 - 40$ K, but multiple components with different temperatures might coexist in equilibrium, including very cold dust as observed in the sub-mm range. The dust characteristic emission depends on the physical properties of the grains, not only on the size, but also their shape, composition, etc., which affects the absorption and the cooling probability of single grains. The resulting dust emissivity is therefore wavelength dependent.

The mid-IR spectrum of the ISM, between ~ 6 μm and ~ 12 μm, is populated by emission lines associated to vibrational de-excitation of polycyclic aromatic hydrocarbons (PAH) molecules. PAHs are excited by single UV photon hits, and subsequently emit a series of IR photons by a cascade process analogous to the optical fluorescence. The emission from PAH indicates rich chemistry in the ISM, and is generally found in association to star forming regions.

Since the mid- and far-IR emission is provoked by young stars shining onto surrounding dust, this wavelength range proves to be a reliable indicator of star formation activity, though dust regions near old stellar populations shining in UV, also produce an infrared cirrus emission induced by ambient field stars. However, the mid-/far-IR emission, turns out to be one of the best available star formation tracers, since it is not affected by extinction effects. Likewise, there exists a very tight relationship between dust continuum luminosity and the non-thermal radio continuum, indicating a mutual connection between the SFR and the SN rate as traced by the cosmic rays. Observationally, this relationship results the tightest among other star formation tracers relations. Other indicators may in fact result less favorable, carrying other classes of uncertainties, for example, Hα and UV emission likely be obscured by interstellar dust, while atomic and molecular gas can also stay in a quiescent state without forming stars. The main reason of this tight relationship between dust emission and non-thermal radio continuum may possibly be due to reduced extinction effects at these wavelengths that minimizes the scatter.

1.5.3 Optical and Near-Infrared

Near-Infrared

Beside dust emission, the IR spectrum, up to ~ 5 μm, also includes the Rayleigh-Jeans regime of light radiation from the stellar component. The extinction by

interstellar dust does not effectively influence the observations in the near-IR bands. Therefore these wavelengths turn out to be fairly suitable for unobscured studies of stellar populations. In normal disk galaxies, most of the emission at these wavelengths is associated to old stellar population both in the disk and the bulge, though bright compact clusters of young stars may also give considerable contribution to the near-IR luminosity. The spiral arms appear very narrow (few hundred of pc) in the optical bands, mostly reflecting hot and young stars. Bands at longer wavelengths are instead more sensitive to the old stellar population and show much broader arms. In fact, older and cooler stars, in particular those of K and M types, dominate in mass and number the stellar component. These stars are characterized by higher velocity dispersion and consequently by higher spatial spread across the spiral arms than the young population.

Optical

The optical bands (from ~ 4000 Å to ~ 6000 Å) trace primarily radiation from stars. A lesser contribution comes from ionized gas, e.g. planetary nebulae and H II regions, and from blue diffuse emission due to differential scatter by interstellar dust, most effective at shorter wavelengths.

Color-magnitude diagrams of resolved stellar populations, allow to determine global properties of clusters or individual stars, e.g. age, temperature, and metalicity, which can be applied to systems where individual stars are unresolved, such as distant galaxies, and derive their properties. In this sense the integrated light of galaxies provides details about total stellar mass, average population, metalicity, star formation history, etc. However, in normal galaxies most of the total luminosity is emitted by the brightest stars, the less representative stars of the sample population, since most massive stars represent only a minor fraction of the total number of stars, while K and M type stars yield the main contribution in mass and number to the total galactic population.

Also absorption patterns reveal to be noteworth in the visible bands. At these wavelengths, dusty regions are observed in absorption as dark patches, which consist of dense and metal rich environments, displaying PAH features and IR emission, and dominated by molecular – and typically gravitationally unstable – gas. For these characteristics dust lanes are commonly associated to regions of active star formation.

Recombination Lines

Emission due to recombination lines is characteristic of H II regions, where young and hot stars are able to efficiently ionize and heat the surrounding gas, predominantly hydrogen. After being ionized, the electrons recombine to the protons initially at any energy level, and descend to successive lower states, producing series of cascade emission lines. The most luminous hydrogen line in the optical bands is the Hα, the first line of the Balmer series. While Hα emission could be affected by extinction, Paα traces dust-obscured ionized hydrogen in the

near-IR. Beside recombination lines, forbidden lines – collision-stimulates de-excitations of metastable energy levels of atoms and ions – are also commonly observed in H II regions.

An H II region is basically an evolved GMC and typically have a lifetime of a few million years. During this time the system is effectively dissipated by the ionizing radiation field and winds of the newborn massive stars. Narrow band imaging of ionization lines, e.g. Hα, Paα, etc., permit to trace star forming regions and to estimate their SFR.

1.5.4 UV and High Energies

In general, stars that are very massive and luminous in the UV are also quite young, typically less than 10^9 years. While tracers such as Hα are interpreted and indirect signature of star formation, the UV light directly targets the photospheres of those young and massive stars that subsequently collapse into SNe and contribute to the metal enrichment of the ISM (Cowie et al. 1988). Therefore, the UV bands are continuously regarded for observational studies of star forming regions. However, a remarkable degree of uncertainty arises from extinction effects. Since the reddening is more effective at short wavelengths, small variations in the interstellar dust column densities may reflect in strong variations in extinction.

At higher energies (keV – MeV), there is a large variety of radiation sources. Galactic objects that emit X-rays are in general accretion phenomena of a central compact object, for example in X-ray binaries, neutron stars, black holes, super-massive black holes, etc., where material is heated by friction during the accretion process, or accelerated and violently shocked against high density surfaces, e.g. in white dwarfs, neutron stars and SN remnants. The inter-galactic medium can also be a source of X-rays where the gas infalling into the potential well of a galaxy cluster is shock-heated up to $10^7 - 10^8$ K via bremsstrahlung process. At extreme energies (MeV – GeV/TeV), γ-rays are produced by cosmic ray collisions with interstellar gas, by SN explosions, and by inverse Compton effect – photons colliding with energetic electrons accelerated by magnetic fields near pulsars or quasars.

1.6 Relevant Questions

We address in the next chapters some relevant issues concerning star formation. Specifically, using a multi-wavelength mapping of a sample of nearby galaxies, we focus on the analysis and interpretation of star formation proxies, of atomic and molecular gas emission, and of H I gas kinematics.

Our investigation draws on two large observational programs, SINGS (Kennicutt et al. 2003) and THINGS (Walter et al. 2008), which provide a high resolution and sensitivity mapping of local Universe galaxies (Chap. 2). SINGS, carried out with the Spitzer infra-red space telescope, probes the dust emission in the mid-infrared between 3.6 and 8.0 μm and in the far-infrared between 24 and 160 μm,

and it is complemented with optical, UV, and radio observations of the CO and H I emissions. THINGS, constituted by 21-cm H I observations carried out at the NRAO Very Large Array, provides not only the emissivity maps, but also the H I gas kinematics, thus velocity maps and rotation curves. Combining the multi-wavelength imaging of SINGS and THINGS permits to study the distribution and dynamics of the H I gas, and the diverse stellar populations and phases of the ISM.

Using the H I kinematics we attempt to separate the orbital motions induced by the galaxy gravitational potential and those motions attributable to feedback (Chap. 3). We construct an analytic model for the H I velocity maps including also the effects due to a non-axisymmetric potential, treating the problem in terms of perturbation theory. We propose to investigate how the velocity residuals, obtained by comparing the observed and the model velocity maps, are related to the presence of young stellar activity.

We estimate the characteristic time scale for star formation in spiral galaxies (Chap. 4). Measuring the angular offset $\Delta\phi$ between the patterns of 21-cm H I and 24 μm hot dust emissions, knowing the H I rotation velocity Ω, and assuming a constant pattern speed Ω_p, we calculate the implied time span $t_{\mathrm{HI}\mapsto 24\,\mu\mathrm{m}}$ between these two patterns, which indicate two sequential phases – the onset of the cloud collapse and the formation of massive star clusters. In other words, we geometrically test the simple kinematic equation $\Delta\phi = (\Omega - \Omega_p) \times t_{\mathrm{HI}\mapsto 24\,\mu\mathrm{m}}$ as a function of galactocentric radius, which provide the average time scale between the dense – and super-critical – phase of the H I and the the existence of massive stars that heat the surrounding dust, and the value of the instantaneous pattern speed of the spiral wave.

Ultimately, we study the connection between turbulence in the H I traced by the velocity dispersion, and the surface density SFR obtained by combining 24 μm and UV emissions (Chap. 5). We investigate, whether the H I turbulent motions could be induced by energetic processes due to the onset of star formation, which could include, winds and UV radiation from hot stars, and, more importantly, SNe explosions.

Bibliography

Balbus, S. A., & Hawley, J. F. 1991, ApJ, 376, 214

Ballesteros-Paredes, J. 2006, MNRAS, 372, 443

Ballesteros-Paredes, J., & Hartmann, L. 2007, RevMexA&A, 43, 123

Ballesteros-Paredes, J., Hartmann, L., & Vázquez-Semadeni, E. 1999, ApJ, 527, 285

Ballesteros-Paredes, J., Klessen, R. S., Mac Low, M.-M., & Vazquez-Semadeni, E. 2007, Protostars and Planets V, 63

Ballesteros-Paredes, J., Vázquez-Semadeni, E., & Scalo, J. 1999, ApJ, 515, 286

Bash, F. N., Green, E., & Peters, W. L., III 1977, ApJ, 217, 464

Basu, S., Mouschovias, T. C., & Paleologou, E. V. 1997, ApJL, 480, L55

Battinelli, P., Efremov, Y., & Magnier, E. A. 1996, A&A, 314, 51

Bertin, G., Lin, C. C., Lowe, S. A., & Thurstans, R. P. 1989, ApJ, 338, 104

Binney, J., & Tremaine, S. 1987, Princeton, NJ, Princeton University Press, 1987, 747 p.,

Blitz, L., Fukui, Y., Kawamura, A., Leroy, A., Mizuno, N., & Rosolowsky, E. 2007, Protostars and Planets V, 81

Blitz, L., & Shu, F. H. 1980, ApJ, 238, 148

Boissier, S., Prantzos, N., Boselli, A., & Gavazzi, G. 2003, MNRAS, 346, 1215

Bournaud, F., Elmegreen, B. G., & Elmegreen, D. M. 2007, ApJ, 670, 237

Boselli, A., Lequeux, J., & Gavazzi, G. 2002, Ap&SS, 281, 127

Cannon, J. M., et al. 2005, ApJL, 630, L37

Cowie, L. L., Lilly, S. J., Gardner, J., & McLean, I. S. 1988, ApJL, 332, L29

Dib, S., Bell, E., & Burkert, A. 2006, ApJ, 638, 797

Dib, S., & Burkert, A. 2005, ApJ, 630, 238

Dickey, J. M., McClure-Griffiths, N. M., Stanimirović, S., Gaensler, B. M., & Green, A. J. 2001, ApJ, 561, 264

Efremov, Y. N. 1995, AJ, 110, 2757

Efremov, Y. N., & Elmegreen, B. G. 1998, MNRAS, 299, 588

Egusa, F., Sofue, Y., & Nakanishi, H. 2004, PASJ, 56, L45

Elmegreen, B. G. 1987, ApJ, 312, 626

Elmegreen, B. G. 1990, ApJL, 361, L77

Elmegreen, B. G. 1993, ApJL, 419, L29

Elmegreen, B. G. 1994, ApJ, 433, 39

Elmegreen, B. G. 1995, MNRAS, 275, 944

Elmegreen, B. G. 2000, ApJ, 530, 277

Elmegreen, B. G. 2007, ApJ, 668, 1064

Elmegreen, B. G., & Elmegreen, D. M. 1983, MNRAS, 203, 31

Elmegreen, B. G., & Elmegreen, D. M. 1986, ApJ, 311, 554

Elmegreen, B. G., & Elmegreen, D. M. 2001, AJ, 121, 1507

Elmegreen, B. G., Elmegreen, D. M., & Leitner, S. N. 2003, ApJ, 590, 271

Elmegreen, B. G., Elmegreen, D. M., & Montenegro, L. 1992, ApJS, 79, 37

Elmegreen, B. G., & Falgarone, E. 1996, ApJ, 471, 816

Elmegreen, B. G., Kim, S., & Staveley-Smith, L. 2001, ApJ, 548, 749

Elmegreen, D. M., & Salzer, J. J. 1999, AJ, 117, 764

Engargiola, G. A., Navarrini, A., Plambeck, R. L., & Wadefalk, N. 2004, Proc. SPIE, 5498, 556

Fall, S. M., & Efstathiou, G. 1980, MNRAS, 193, 189

Feitzinger, J. V., & Galinski, T. 1987, A&A, 179, 249

Fleck, R. C., Jr. 1981, ApJL, 246, L151

Förster Schreiber, N. M., et al. 2006, ApJ, 645, 1062

Freeman, K. C. 1970, ApJ, 160, 811

Fukui, Y., et al. 1999, PASJ, 51, 745

Fukui, Y. 2007, IAU Symposium, 237, 31

Genzel, R., et al. 2006, Nature, 442, 786

Gerola, H., & Seiden, P. E. 1978, ApJ, 223, 129

Goldreich, P., & Lynden-Bell, D. 1965, MNRAS, 130, 97

Gómez, G. C., & Cox, D. P. 2002, ApJ, 580, 235

Gritschneder, M., Naab, T., Heitsch, F., & Burkert, A. 2006, ArXiv Astrophysics e-prints, arXiv:astro-ph/0609709

Harris, J., & Zaritsky, D. 1999, AJ, 117, 2831

Hartmann, L. 2002, ApJ, 578, 914

Hartmann, L. 2003, ApJ, 585, 398

Hartmann, L., Ballesteros-Paredes, J., & Bergin, E. A. 2001, ApJ, 562, 852

Heitsch, F., Mac Low, M.-M., & Klessen, R. S. 2001, ApJ, 547, 280

Henning, T. 1989, Astronomische Nachrichten, 310, 363

Hunter, D. A., Elmegreen, B. G., & Baker, A. L. 1998, ApJ, 493, 595

Jog, C. J., & Solomon, P. M. 1984, ApJ, 276, 127

Joung, M. K. R., & Mac Low, M.-M. 2006, ApJ, 653, 1266

Kawamura, A., Minamidani, T., Mizuno, Y., Onishi, T., Mizuno, N., Mizuno, A., & Fukui, Y. 2007, IAU Symposium, 237, 101

Kennicutt, R. C., Jr. 1989, ApJ, 344, 685

Kennicutt, R. C., Jr. 1998, ApJ, 498, 541

Kennicutt, R. C., Jr., et al. 2003, PASP, 115, 928

Kennicutt, R. C., Jr., et al. 2007, ApJ, 671, 333

Kim, J., Hong, S. S., Ryu, D., & Jones, T. W. 1998, ApJL, 506, L139

Kim, W.-T., & Ostriker, E. C. 2002, ApJ, 570, 132

Kim, W.-T., Ostriker, E. C., & Stone, J. M. 2002, ApJ, 581, 1080

Klessen, R. S., Ballesteros-Paredes, J., Li, Y., & Mac Low, M.-M. 2004, The Formation and Evolution of Massive Young Star Clusters, 322, 299

Klessen, R. S., Burkert, A., & Bate, M. R. 1998, ApJL, 501, L205

Klessen, R. S., Heitsch, F., & Mac Low, M.-M. 2000, ApJ, 535, 887

Kolmogorov, A. 1941, Akademiia Nauk SSSR Doklady, 30, 301

Kosiński, R., & Hanasz, M. 2007, MNRAS, 376, 861

Leisawitz, D., Bash, F. N., & Thaddeus, P. 1989, ApJS, 70, 731

Leroy, A., Bolatto, A. D., Simon, J. D., & Blitz, L. 2005, ApJ, 625, 763

Li, Y., Mac Low, M.-M., & Klessen, R. S. 2005, ApJL, 620, L19

Li, Y., Mac Low, M.-M., & Klessen, R. S. 2006, ApJ, 639, 879

Lin, C. C., & Shu, F. H. 1964, ApJ, 140, 646

Luna, A., Bronfman, L., Carrasco, L., & May, J. 2006, ApJ, 641, 938

Mac Low, M.-M., & Klessen, R. S. 2004, Reviews of Modern Physics, 76, 125

Mac Low, M.-M., Klessen, R. S., Burkert, A., & Smith, M. D. 1998, Physical Review Letters, 80, 2754

Mark, J. W. K. 1976, ApJ, 205, 363

Martin, C. L., & Kennicutt, R. C., Jr. 2001, ApJ, 555, 301

Matzner, C. D., & McKee, C. F. 2000, ApJ, 545, 364

Mouschovias, T. C. 1974, ApJ, 192, 37

Mouschovias, T. C., Shu, F. H., & Woodward, P. R. 1974, A&A, 33, 73

Mueller, M. W., & Arnett, W. D. 1976, ApJ, 210, 670

Nakamura, F., & Li, Z.-Y. 2005, ApJ, 631, 411

Norman, C. A., & Ikeuchi, S. 1989, ApJ, 345, 372

Onishi, T., Mizuno, A., Kawamura, A., Tachihara, K., & Fukui, Y. 2002, ApJ, 575, 950

Ossenkopf, V., Klessen, R. S., & Heitsch, F. 2001, A&A, 379, 1005

Ossenkopf, V., & Mac Low, M.-M. 2002, A&A, 390, 307

Parker, E. N. 1966, ApJ, 145, 811

Pietrzyński, G., Gieren, W., Fouqué, P., & Pont, F. 2001, A&A, 371, 497

Piontek, R. A., & Ostriker, E. C. 2007, ApJ, 663, 183

Polk, K. S., Knapp, G. R., Stark, A. A., & Wilson, R. W. 1988, ApJ, 332, 432

Quirk, W. J. 1972, ApJL, 176, L9

Roberts, W. W. 1969, ApJ, 158, 123

Robertson, B., Yoshida, N., Springel, V., & Hernquist, L. 2004, ApJ, 606, 32

Safronov, V. S. 1960, Annales d'Astrophysique, 23, 979

Sánchez-Salcedo, F. J. 2002, Revista Mexicana de Astronomia y Astrofisica, 38, 39

Santillán, A., Sánchez-Salcedo, F. J., & Franco, J. 2007, ApJL, 662, L19

Schaye, J. 2004, ApJ, 609, 667

Schmidt, M. 1959, ApJ, 129, 243

Seiden, P. E., & Gerola, H. 1982, Fundamentals of Cosmic Physics, 7, 241

Scoville, N. Z., & Solomon, P. M. 1975, ApJL, 199, L105

Sellwood, J. A. 1981, A&A, 99, 362

Sellwood, J. A., & Balbus, S. A. 1999, ApJ, 511, 660

Shirley, Y. L., Evans, N. J., II, Young, K. E., Knez, C., & Jaffe, D. T. 2003, ApJS, 149, 375

Silk, J. 1997, ApJ, 481, 703

Solomon, P. M., Sanders, D. B., & Scoville, N. Z. 1979, ApJL, 232, L89

Spitzer, L. J. 1968, Nebulae and interstellar matter. Edited by Barbara M. Middlehurst; Lawrence H. Aller. Library of Congress Catalog Card Number 66-13879. Published by the University of Chicago Press, Chicago, ILL USA, 1968, p.1, 1

Stone, J. M., Ostriker, E. C., & Gammie, C. F. 1998, ApJL, 508, L99

Stutzki, J., Bensch, F., Heithausen, A., Ossenkopf, V., & Zielinsky, M. 1998, A&A, 336, 697

Tenorio-Tagle, G., & Bodenheimer, P. 1988, ARA&A, 26, 145

Testi, L., Sargent, A. I., Olmi, L., & Onello, J. S. 2000, ApJL, 540, L53

Thilker, D. A., et al. 2007, ApJS, 173, 538

Toomre, A. 1964, ApJ, 139, 1217

Toomre, A. 1969, ApJ, 158, 899

Toomre, A. 1981, Structure and Evolution of Normal Galaxies, 111

Toomre, A., & Kalnajs, A. J. 1991, Dynamics of Disc Galaxies, 341

Toomre, A., & Toomre, J. 1972, ApJ, 178, 623

Vázquez-Semadeni, E., & García, N. 2001, ApJ, 557, 727

Vázquez-Semadeni, E., Kim, J., Shadmehri, M., & Ballesteros-Paredes, J. 2005, ApJ, 618, 344

Vorobyov, E. I. 2003, A&A, 407, 913

Wada, K., Meurer, G., & Norman, C. A. 2002, ApJ, 577, 197

Wada, K., Spaans, M., & Kim, S. 2000, ApJ, 540, 797

Walter, F. 1999, Publications of the Astronomical Society of Australia, 16, 106

Walter, F., et al. 2008, AJ, submitted

Walter, F., & Brinks, E. 1999, AJ, 118, 273

Wang, B., & Silk, J. 1994, ApJ, 427, 759

Westpfahl, D. J. 1999, Synthesis Imaging in Radio Astronomy II, 180, 201

Westpfahl, D. J., Coleman, P. H., Alexander, J., & Tongue, T. 1999, AJ, 117, 868

Williams, J. P., Blitz, L., & McKee, C. F. 2000, Protostars and Planets IV, 97

Williams, J. P., & McKee, C. F. 1997, ApJ, 476, 166

Wong, T., & Blitz, L. 2002, ApJ, 569, 157

Yamaguchi, R., et al. 2001, PASJ, 53, 985

Zhang, Q., Fall, S. M., & Whitmore, B. C. 2001, ApJ, 561, 727

Zuckerman, B., & Evans, N. J., II 1974, ApJL, 192, L149

Chapter 2

The Data Sample: SINGS and THINGS

Abstract

The research described in this thesis draws extensively on data from two large observational programs: SINGS and THINGS, carried out by the Spitzer infra-red space telescope and by the NRAO Very Large Array (VLA). These two surveys have mapped the gas, dust and stars in a substantial number of nearby spiral galaxies and dwarf galaxies. The new opportunity provided by these surveys consists in several aspects: a high physical resolution, due to high angular resolution and the proximity of the targets, a large angular coverage up to several optical radii, a large data sample spanning over several properties, e.g. star formation rates, morphological types, dynamical masses, etc., and, more importantly, a wide wavelength mapping which enables the study of the various stellar populations and phases of the interstellar medium (ISM). For our specific objectives we use data cubes from VLA observations of the H I emission line at 21-cm as a tracer of the neutral atomic gas. We combine the H I data with emission maps of the Spitzer 24 μm and the GALEX satellite far-UV bands, which we consider as proxies of star formation.

The combination of SINGS and THINGS throws a shed of light on a number of fundamental astrophysical problems, e.g. the physical nature and origin of the Hubble sequence and the galaxy evolution, and how this relates to the local structures of the ISM and its phase balance, and the interpretation of high-redshift observations, although many questions in the local universe remain open. In fact, our understandings of star formation on galactic scales, the consumption of the gas reservoir, and the existence of star formation laws that appear universal for different environments, are still relatively limited.

2.1 SINGS

The Spitzer Infrared Nearby Galaxies Survey (SINGS; Kennicutt et al. 2003) project has been designed to probe galaxies in the local Universe at mid- to far-infrared emission, in order to study galaxy properties, including the interstellar medium (ISM) and unobscured star formation (SF) environments. The infrared (IR) data from the Spitzer satellite are complemented by observations in visible/UV and submillimeter/IR bands. The ensemble of data provides a multi-wavelength perspective of the physical processes in SF and ISM.

2.1.1 Scientific Targets

The mid- and far-infrared emission of galaxies is a suitable range of exploration of young star forming regions and their ISM associations – gas and dust. The UV radiation emitted by young stars in the range 6 eV $< h\nu <$ 13.6 eV shines on the surrounding gas and dust, producing ionization of molecules and atoms, and photo-dissociation regions (PDR; Hollenbach & Tielens 1999). The heated dust grains emits the absorbed power through thermal continuum emission and a large number of emission lines associated to various ionized elements, molecules and excited polycyclic aromatic hydrocarbons (PAH). In H II regions and in PDRs the dust grain emission provides most of the radiation flux from a galaxy, but dust in ambient clouds illuminated by the interstellar radiation field can also be important (Lonsdale-Persson & Helou 1987).

SINGS is composed of imaging and spectroscopic study of 75 nearby galaxies. The full coverage and the vicinity of the target galaxies, whose distances range between 1 and 30 Mpc, provides high physical details. For a galaxy like M81 at a distance of 3.5 Mpc the linear dimension that can be resolved range from 40 pc to 100 pc for the Spitzer/IRAC bands, and from 300 pc to 700 pc for the Spitzer/MIPS bands. Combining IR with UV and Hα maps of dust-obscured star forming regions, SINGS offers complete and unbiased maps of massive SF. The IR spectral energy distributions (SED) and the multi-wavelength analysis also are suitable for probing (1) the dust properties, like temperature and distribution, (2) the properties of star forming regions, whose heating flux can be constrained knowing the dust temperature, and (3) the hardness and ionizing flux, using the spectral line ratios.

Ancillary Data

The mid- and far-IR Spitzer satellite observations consist in a multi-wavelength mapping carried out with the 3.6, 4.5, 5.8 and 8.0 μm bands of the IRAC instrument and with the 24, 70, and 160 μm bands of the MIPS instrument. The Spitzer observations are fully complemented with a multi-wavelength set of imaging, covering the spectrum from UV/optical to sub-millimeter/radio. Multi-color broadband imaging in the visible and near-IR, namely $BVRIJHK$, Hα, and radio 21-cm H I (see § 2.2) and millimeter CO lines, sets constraints on the stellar SED and populations, stellar mass and on the dust extinction,

while the Hα imaging allows to estimate the star formation rate (SFR) and to derive informations on the geometric and evolutionary properties of star forming regions, and the radio maps trace the warm and cold gaseous ISM.

For this purpose a number of other observational programs has been involved. Besides optical/near-IR ground based imaging at KPNO (Meurer et al. 2006) and CTIO (Kuchinski et al. 2000), the surveys that have been exploited are: the Two-Micron All Sky Survey (2MASS; Jarrett et al. 2003) for the near-IR imaging in JHK, the Galaxy Evolution Explorer (GALEX; Gil de Paz et al. 2007) for the UV in 1350-3000 Å wavelength range , HST Paα line and H band imaging (Böker et al. 1999; Holwerda et al. 2005), and the Berkeley-Illinois-Maryland Association Survey of Nearby Galaxies (BIMA SONG; Helfer et al. 2003) for CO maps. Ultimately, the THINGS program (§ 2.2) undertakes a complementary survey of the SINGS sample.

Project Motivations: importance of multi-wavelength

The large number and the diverse morphological types of the SINGS galaxies allow to recognize on different scales the influences of gas and dust properties, like density, phase, metalicity, and temperature, across the Hubble sequence. In this sense also the global pattern of SF and therefore the individual galaxy evolution may vary as a function of the Hubble type.

Most of our understanding concerning the physics of SF processes in galaxies relies on studies in optical and UV bands (e.g. Kennicutt 1998). However, at these wavelengths the main source of systematic errors is due to interstellar dust extinction, which can also be highly non-uniform within galaxies. Consistently with the fact that half of the absorbed light is re-radiated in the IR, the typical variations produce in average about 1 magnitude for near-UV/optical bands and are the largest specially in active star forming regions, which are environments chemically abundant and rich of dust and where the extinction could be of several magnitudes (> 30). According to Heckman (1999), about 20-30% of all star forming regions in the local universe is heavily obscured to UV/visible light. In contrast, the IR bands successfully reveal the presence of young star clusters emitting UV, since the ISM is optically thin at these wavelengths even for regions with high column densities. Multi-band IR imaging provides resolved SED maps, which combined with CO, H I, and UV/visible maps are suitable for studying and modeling the processes of cloud and star formation, the gaseous environments, spiral arms etc.

An accurate view of dust-enshrouded and fully exposed star forming regions can be obtained by combining SF proxies as Hα and UV maps with the IR SED maps. The enshrouded IR emitting regions without UV/Hα associations trace the youngest cores of SF. UV/Hα emitting regions are supposedly evolved environments, where the dusty and obscuring envelope has been removed and dissipated. Eventually, the low extreme can be explored – galaxies with quiescent SF, like (1) ellipticals and S0, which are dust poor due to internal processes such as stellar mass loss, or feedback from a nuclear super-massive object, or from mergers that dissipate the galactic gaseous content, or like (2) dwarf galax-

ies and (3) low surface brightness galaxies, where the SF has been suppressed by SN feedback or the gas density is sub-critical.

Usage of the Data

The analysis carried out in this thesis involves the utilization of H I maps, which we will describe in § 2.2, as an indicator of the neutral atomic gas phase. In addition, we combine these data with SINGS maps.

In Chap. 4 we interpret angular offsets between the H I and heated dust emissions in arm and inter-arm environments as a sequence of two distinct phases of the ISM and measure the characteristic time separation. We consider that the MIPS bands, 24, 70, and 160 μm) are tracing hot dust heated by UV radiation from young massive stars, and are thus optimal indicators of recent SF activity. The two regarded phases, H I and dust emission, represent therefore the material that is about to form a molecular clouds and young dust-enshrouded stellar clusters. For our purpose, rely on the band with the highest resolution, more precisely 24 μm. Since the PAH features traced by the 8 μm Spitzer/IRAC band may undergo strong depletion in presence of intense UV radiation, the 24 μm band has been recognized as the best of the Spitzer bands for tracing SF (Calzetti et al. 2005, 2007), although the 8 μm band has higher resolution.

In Chap. 5 we study the local interplay between H I turbulence, as traced by the velocity dispersion (see § 2.2.2), and the surface density of SFR. We carry out our intent by combining the MIPS 24 μm and the GALEX far-UV maps following Calzetti et al. (2007) methodology, in order to estimate the SFR maps for the sample galaxies. While the MIPS 24 μm traces dust-enshrouded and ongoing SF over a time scale $3-10$ Myr, the far-UV emission complements the 24 μm emission in the regions poor in dust content, probing therefore low-metalicity and older regions of SF (e.g. outermost parts of spiral galaxies) over timescales of $\tau \sim 10-100$ Myr.

2.2 THINGS

The H I Nearby Galaxy Survey (THINGS; Walter et al. 2008) is a large observational project carried out at the NRAO[1] Very Large Array (VLA) to obtain 21-cm H I observations of nearby galaxies at high spatial resolution ($\sim 7''$), and velocity resolution (≤ 5.2 km s^{-1}), and homogeneous ($5\,\sigma$) sensitivity to column density of $N(HI) \geq 8 \times 10^9$ cm^{-2} per channel for a substantial fraction of the galaxies of the sample. A total sample of 34 objects, at distances $2 < D < 15$ Mpc, has been selected in order to overlap a large fraction of the SINGS data set galaxies. The properties of the galaxies also are selected in order to cover a wide range of SFRs ($\sim 10^{-3} - 6$ M$_\odot$ yr^{-1}), H I total masses ($0.01 - 14 \times 10^9$ M$_\odot$) and dynamical masses, absolute luminosities (M$_B$ from

[1]The National Radio Astronomy Observatory is a facility of the National Science Foundation operated under cooperatice agreement by Associated Universities, Inc.

-11.5 to -21.7 mag), and metalicities ($7.5-9.2$ in units of $12+\log(\mathrm{O/H})$). The most direct scientific goals of THINGS aim to the investigation of the ISM in relation with the Hubble type, SF and mass distribution, as well as the small- and large-scale kinematics, and the processes that lead to and influence SF. The galaxies taken from the THINGS sample and considered throughout this thesis are listed in Table 2.1.

2.2.1 Science of THINGS

The scientific perspectives achievable with the THINGS survey cover a wide range of topics. The two main branches include at first hand, the kinematics and the dynamics of the H I disks and their implications, and secondly, the study of the ISM properties and the interplay with SF processes. The best profit is obtained as THINGS and SINGS are combined together.

The high resolution rotation curves enable a characterization of the total visible and dark matter distribution in disk galaxies. The stellar mass can be obtained from estimates of the mass to light ratio supplied by the Spitzer 3.6 μm and the K band imaging (de Blok et al. 2008). The results can be further compared with the prediction of the cold dark matter paradigm (Navarro et al. 1996, 1997; Moore et al. 1999) and other observational findings on the problem of the halo cuspyness (de Blok et al. 2001). The velocity fields also allow to quantify the relevance of non-circular motions in galaxies (Trachternach et al. 2008; Oh et al. 2008) and determine the character of non-axisymmetric perturbations to the potential and the location of resonances (see Chap. 3).

One of the most striking aspects emerging from THINGS are the many holes and supergiant shells seen at high resolution in the H I integrated maps (Bagetakos et al. 2008). The THINGS data quality offers not only the opportunity for several structural studies, for example the fine scale structure of the ISM by studying the H I peak surface brightness distribution (Usero et al. 2008), and the analysis of H I edges of galactic disks (Portas et al. 2008), but also a comparative study of the H I properties of nearby galaxies and the H I absorption features found in damped Lyman alpha systems at high redshift (Zwaan et al. 2008).

Since the resolution of the H I maps is similar to that obtained with the Spitzer bands, direct comparison of spatial distribution of the neutral gas and the dust emission, which is an unobscured proxy for recently formed stars, allows to determine the time scales for the SF to set on spiral arm environments. This method, illustrated in detail in Chap. 4, suggests a follow up application to regions of molecular clouds and H II associations using other bands, e.g. CO, Hα, and UV, in order to put constraints on the evolutionary phases of the ISM.

The comparative study of SF and ISM, e.g. using Calzetti et al. (2007) method, permits to calculate pixel-by-pixel (corresponding to scales of 100-500 pc) the SFR, which combined with the measured H I and CO gas densities allows to constrain the Schmidt-Kennicutt law on sub-kiloparasec scales (Bigiel et al. 2008). Combining the SFR maps with the H I and CO emission maps also allow to investigate the existence of a universal SF threshold and its character locally

– testing disk and cloud instability, spiral density waves, and tidal effects – and globally as a function of galaxy type (Leroy et al. 2008). Besides the Q stability parameter proposed by Toomre (1964), other methods to calculate and test the SF threshold can be applied at high resolution (e.g. Martin & Kennicutt 2001; Schaye 2004; Li, Mac Low, & Klessen 2005).

A fundamental issue related to the instability criteria and the SF threshold is the velocity dispersion (see Chap. 5). The gas velocity dispersion maps obtained from THINGS probes the degree of turbulence in the ISM and the local balance between gravitational forces and pressure support. Turbulence indeed provides support to molecular clouds by suppressing the collapse and quenching the SF, but is also able to produce local enhancements of density, inducing the collapse of super-critical regions and consequent SF (Mac Low & Klessen 2004). The combined study with SINGS also probes the location of recent SF regions and their impact in terms of energy input. Estimate this energy input is crucial to understand not only the formation of bubbles and supergiant shells, which may in turn trigger secondary events of SF (Cannon et al. 2005), but also the mechanisms that possibly drive turbulence in the ISM (Dib, Bell, & Burkert 2006; Kim & Ostriker 2006; Wada, Meurer, & Norman 2002).

2.2.2 Description of THINGS

The galaxies sample of THINGS has been selected in order to complement part of the SINGS observations and to extend the investigation of the ISM to the neutral atomic gas regime. The selected galaxies present a large variety of properties in terms of (1) mass and luminosity going from dwarf to massive galaxies, (2) of SF efficiency including quiescent and normal galaxies, and one starburst (NGC 4826), and (3) of metalicity. The sample does not include elliptical and S0 galaxies, due to their different properties with respect to late type galaxies, and edge-on disks, to avoid ambiguities while modeling deprojected patterns.

The scientific purposes of THINGS – e.g. to accurately determine the central slope of the rotation curves or to compare the spatial properties of H I and ISM as traced by the Spitzer bands – require high spatial and spectral resolution. High spatial resolution is provided since the galaxies are nearby, the distances range from 3 to 15 Mpc. The achieved physical resolutions ranges from 100 to 500 pc, provided that the angular resolution of the VLA, is $6''$, which is comparable to Spitzer and GALEX resolutions, being $\sim 6''$ at 24 μm and $\sim 5''$ in NUV, respectively. The obtained velocity resolution varies within 2.5 to 5 km s^{-1}, from object to object, and is needed to adequately sample the line width of the warm neutral medium, whose FWHM typically corresponds to $6 - 12$ km s^{-1}.

H I Generic Maps

The processing of the 21-cm line data cubes to obtain meaningful maps, such as total flux, velocity fields, or higher moments, can be operated through several methods. The emission lines can be either numerically integrated along the velocity axis, and therefore the emission line moments are denoted in terms of

statistics over several channels, or fitted with a model function, whose analytic parameters yield the line moments.

The observation are characterized by a 1-σ noise of $\sim$ 0.4 mJy beam^{-1} corresponding to a column density detection limit of 3.2×10^{20} cm^{-2} for a $6''$ beam, which is well below the typical value of 10^{21} cm^{-2} of column density observed in normal disk galaxies. Sensitivity limits as low as 4×10^{19} cm^{-2}, typical of outer regions of disks, could be achieved by convolving the data cubes to a resolution of $30''$. The total spectral width of the data cubes brackets the whole range of velocities of the corresponding observed galaxy, and the spectral sampling of the data cubes is constant, so that each channel has a width of 2.5 or 5 km s^{-1} depending on each individual observation. In these circumstances, the integrated zeroth moment map is calculated simply by collapsing the data cube along the velocity dimension for a total number N of channels per data cube, where N is typically ~ 100, using:

$$\mu_0 = \sum_{i=1}^{N} S_i, \tag{2.1}$$

where S_i is the signal in the i-th channel. The first moment map, which corresponds to the velocity fields, is given by the intensity-weighted mean velocity:

$$\mu_1 = \frac{1}{\mu_0} \sum_{i=1}^{N} v_i \, S_i, \tag{2.2}$$

where v_i is the velocity value of the i-th channel, and the term $1/\mu_0$ expresses the normalization to the total signal. And lastly, the variance, which corresponds to the velocity dispersion square, is given by intensity-weighted mean deviation:

$$\sigma^2 = \frac{1}{\mu_0} \sum_{i=1}^{N} (v_i - \mu_1)^2 \, S_i. \tag{2.3}$$

Obviously, higher moments, e.g. skewness and kurtosis, can be calculated by extending this iteration. The two main advantages of using the integrated moment maps are that their computation is much straightforward and the definition is model independent. However, the integrated moment values can be highly affected by the presence of noise, and in particular these definitions may even fail in a low signal-to-noise regime, leading to misinterpretation of the results. For example, even a narrow line, whose amplitude is comparable to the noise level, would have higher variance than its actual width. In that case the variance has a non-physical meaning. Note in fact that noise with flat power spectrum of frequencies has zero average signal, but non-zero variance. Moreover, tidal material around the central disks of galaxies affects not only the evaluation of the velocity dispersion, which would clearly be overestimated, but also that of the bulk velocity. Fitting instead the line profiles with an analytic function, compared to direct numerical integration, is a more robust method against the presence of noise. Although, fitting demands the assumption that the data are

best described by the chosen profile, e.g. by a Gaussian. The shape of the line profiles, depending on the galaxy type and on the environmental character of the ISM, show a large variety of properties. In fact, dwarf galaxies are rather dynamically quiescent, and the H I lines present fairly Gaussian profiles, whilst the spirals display signatures of shocks, and broader and asymmetric lines gauging higher level of turbulence. Therefore, at high spectral resolution it becomes preferable to use a Gauss-Hermite expanded function:

$$f(w) = \frac{A\, e^{-\frac{w^2}{2}}}{\sqrt{2\pi}\,\sigma} \left[1 + h_3 \frac{2w^3 - 3w}{\sqrt{3}} + h_4 \frac{4w^4 - 12w^2 + 3}{\sqrt{24}}\right], \qquad (2.4)$$

$$\text{where} \quad w = \frac{v - V}{\sigma},$$

and v is the channel velocity value, V is the mean velocity, σ is the line width, A formally corresponds to the zeroth moment, and h_3 and h_4 to the skewness and kurtosis, respectively. Fitting a Gauss-Hermite profile proves to be more reliable while recovering the mean velocity value from highly asymmetric lines. In a such case, a simple Gaussian profile fit would instead give a biased result. Compared to direct numerical integration, the main drawback of performing a Gaussian or Hermite fit, besides from being computationally slower, is that the method is model dependent. For example, this method is not able to cope with double peaked profiles, since the line model is forced to have a specific shape.

Alternatively to these two methods above illustrated, another technique proves more robust. Regions of low signal-to-noise ratio are blanked out from the data cubes: after convolving the data cubes to a $30''$ resolution, regions which show emission in three consecutive channels above a 2-σ level are retained. This step specifically serves to eliminate the noise and retain only areas of genuine emission in the data cubes. Subsequently, the integrated moment maps can be calculated using Equations 2.1, 2.2, and 2.3. We plot for visual comparison the IRAC 3.6 μm, MIPS 24 μm, BIMA-SONG CO, and the THINGS H I maps for the galaxies M51 and NGC 628 in Fig. 2.1 and in Fig. 2.2, respectively. The H I maps are calculated following the prescriptions of this last described method.

Clearly, the moments interpreted from direct numerical integration and Gauss-functional fitting might differ depending in part on the signal-to-noise regime, and in part on the presence of fine scale structures in the signal. The presence of extra features in the spectral dimension, e.g. tidal and multiple H I clouds in the disk, causes the or in general multiple kinematically disconnected variance calculated by direct integration to overestimate the actual line width, resulting in a value of the variance generally higher than the Gaussian width, since a functional fit proves to better recover the actual line profile. However, direct integration can without biases recover the total signal along the velocity dimension, while Gaussian fitting tends to smooth out fine scale structures, and consequently to underestimate the actual column density.

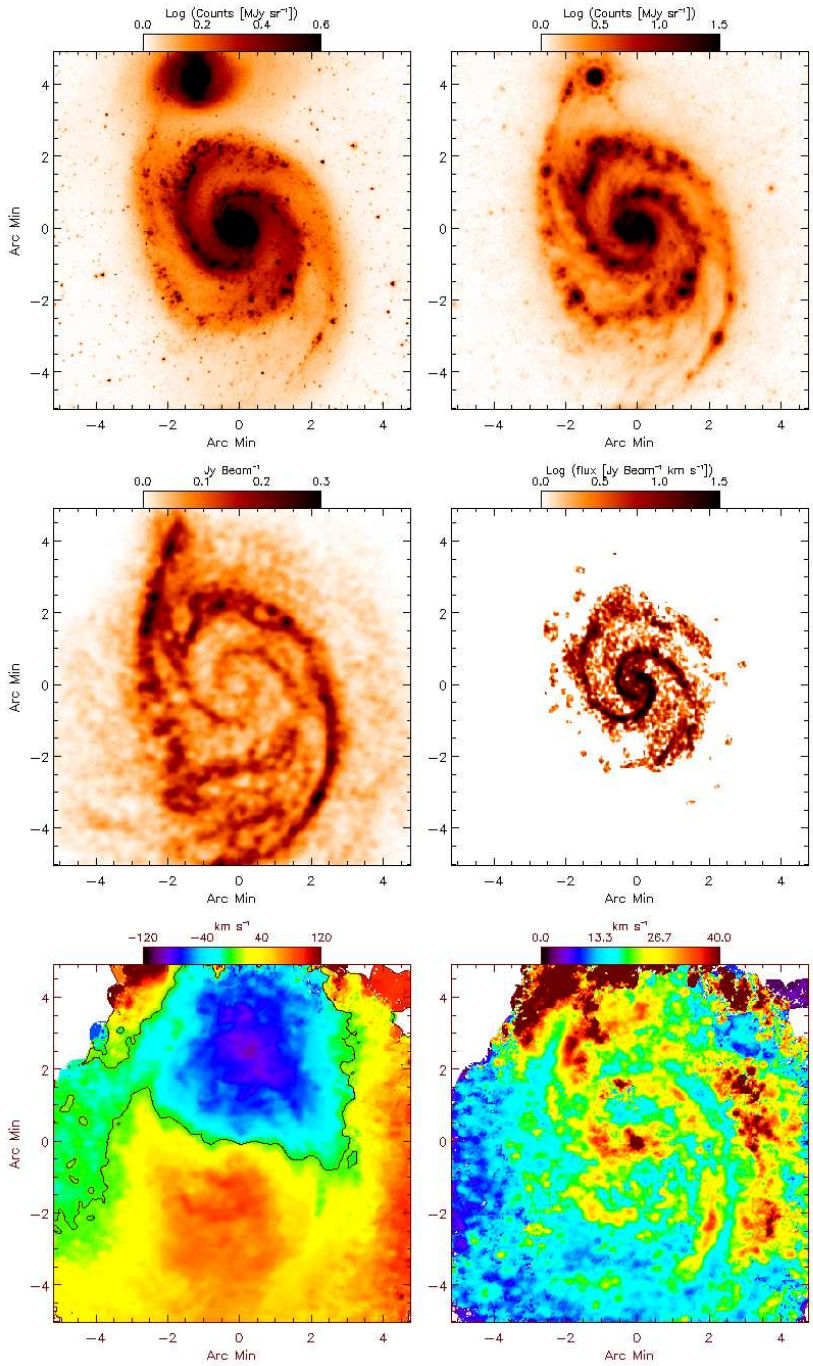

Figure 2.1: M51 – From top left to bottom right: IRAC 3.6 μm emission, MIPS 24 μm emission, H I integrated map (Eq. 2.1), CO (BIMA SONG) emission, H I velocity field (Eq. 2.2), where the solid line denotes $v = 0$, and H I velocity dispersion (Eq. 2.3).

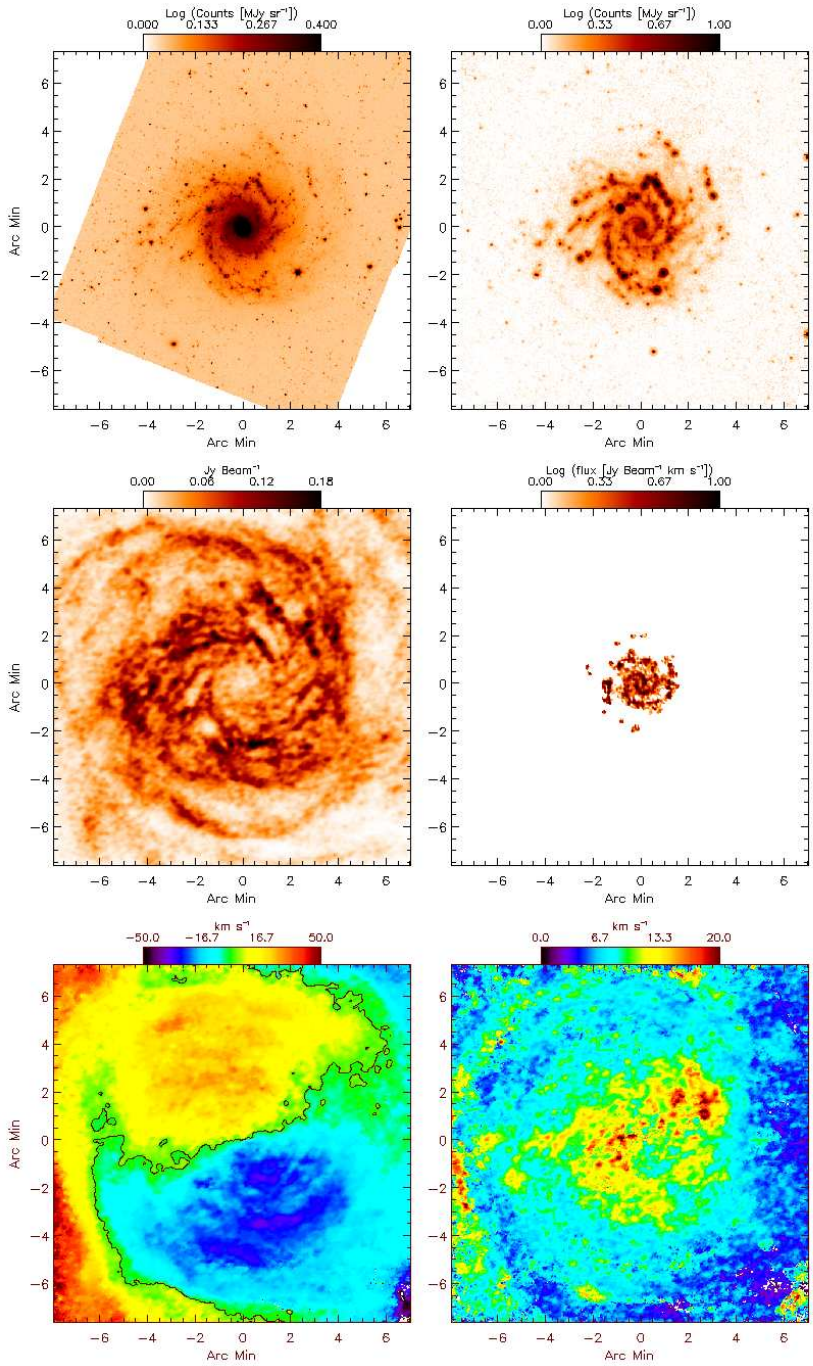

Figure 2.2: NGC 628 – From top left to bottom right: IRAC 3.6 μm emission, MIPS 24 μm emission, H I integrated map (Eq. 2.1), CO (BIMA SONG) emission, H I velocity field (Eq. 2.2), where the solid line denotes $v = 0$, and H I velocity dispersion (Eq. 2.3).

Obj. name	Alt. name	R_{25} ($'$) (1)	i ($^\circ$) (2)	PA ($^\circ$) (3)	D (Mpc) (4)	$v_{\rm max}$ (km s^{-1}) (5)
NGC 2403		9.98	63	124	3.22	128
NGC 2841		3.88	74	153	14.1	331
NGC 2903		5.6	65.2	204.3	8.9	
NGC 3031	M81	10.94	59	330	3.63	256
NGC 3184		3.62	16	179	11.1	260
NGC 3351	M95	3.54	41	192	9.33	210
NGC 3521		4.8	73	340	10.05	241
NGC 3621		5.24	65	345	6.64	144
NGC 3627	M66	4.46	62	173	9.25	204
NGC 4214		3.38	43.7	65	2.94	56
NGC 4736	M94	3.88	41.4	296.1	4.66	167
NGC 5055	M63	6.01	59	102	7.82	209
NGC 5194	M51	4.89	42	172	7.77	241
NGC 5236	M83	7.06	24	225	4.47	
NGC 5457	M101	11.99	18	39	7.38	
NGC 628	M74	4.77	7	20	7.3	219
NGC 6946		5.35	32.6	242	5.5	201
NGC 7793		5.0	50	290	3.82	109
NGC 925		5.23	66	286	9.16	121
IC 2574		6.44	53.4	55.7	4.02	73
HOII		3.3	41	177	3.39	38

Table 2.1: THINGS and SINGS target galaxies studied in this thesis. (1): semi-major axis of the 25 mag arcsec^{-2} isophote in the B band obtained from the LEDA database (URL: http://leda.univ-lyon1.fr/); (2) and (3): kinematic inclination and PA, respectively; (4): adopted distance; (5): maximum amplitude of the rotation velocity corrected for inclination.

Bibliography

Bagetakos, I., et al. 2008, AJ, submitted

Bigiel, F., et al. 2008, AJ, submitted

Böker, T., et al. 1999, ApJS, 124, 95

Calzetti, D., et al. 2005, ApJ, 633, 871

Calzetti, D., et al. 2007, ApJ, 666, 870

Cannon, J. M., et al. 2005, ApJL, 630, L37

de Blok, W.J.G, et al. 2008, AJ, submitted

de Blok, W. J. G., McGaugh, S. S., Bosma, A., & Rubin, V. C. 2001, ApJL, 552, L23

Dib, S., Bell, E., & Burkert, A. 2006, ApJ, 638, 797

Gil de Paz, A., et al. 2007, ApJS, 173, 185

Heckman, T. M. 1999, After the Dark Ages: When Galaxies were Young (the Universe at $2 < z < 5$), 470, 322

Helfer, T. T., Thornley, M. D., Regan, M. W., Wong, T., Sheth, K., Vogel, S. N., Blitz, L., & Bock, D. C.-J. 2003, ApJS, 145, 259

Hollenbach, D. J., & Tielens, A. G. G. M. 1999, Reviews of Modern Physics, 71, 173

Holwerda, B. W., Gonzalez, R. A., Allen, R. J., & van der Kruit, P. C. 2005, AJ, 129, 1396

Jarrett, T. H., Chester, T., Cutri, R., Schneider, S. E., & Huchra, J. P. 2003, AJ, 125, 525

Kennicutt, R. C., Jr. 1998, ApJ, 498, 541

Kennicutt, R. C., Jr., et al. 2003, PASP, 115, 928

Kim, W.-T., & Ostriker, E. C. 2006, ApJ, 646, 213

Kuchinski, L. E., et al. 2000, ApJS, 131, 441

Leroy, A., et al. 2008, in preparation

Li, Y., Mac Low, M.-M., & Klessen, R. S. 2005, ApJL, 620, L19

Lonsdale Persson, C. J., & Helou, G. 1987, ApJ, 314, 513

Mac Low, M.-M., & Klessen, R. S. 2004, Reviews of Modern Physics, 76, 125

Martin, C. L., & Kennicutt, R. C., Jr. 2001, ApJ, 555, 301

Meurer, G. R., et al. 2006, ApJS, 165, 307

Moore, B., Ghigna, S., Governato, F., Lake, G., Quinn, T., Stadel, J., & Tozzi, P. 1999, ApJL, 524, L19

Navarro, J. F., Frenk, C. S., & White, S. D. M. 1996, ApJ, 462, 563

Navarro, J. F., Frenk, C. S., & White, S. D. M. 1997, ApJ, 490, 493

Oh, S.-H., et al. 2008, AJ, submitted

Portas, A., et al. 2008, AJ, submitted

Schaye, J. 2004, ApJ, 609, 667

Toomre, A. 1964, ApJ, 139, 1217

Trachternach, C., et al. 2008, AJ, submitted

Usero, A., et al. 2008, AJ, submitted

Wada, K., Meurer, G., & Norman, C. A. 2002, ApJ, 577, 197

Walter, F., et al. 2008, AJ, submitted

Zwaan, M., et al. 2008, AJ, submitted

Chapter 3

Modeling HI Velocity Maps

Abstract

This chapter describes how we attempt to match and subtract the part of the H I kinematics that is plausibly due to gravitationally induced orbital motions. This may then leave the position of the kinematics that is attributable to feedback. In other words, provided that we can model H I kinematics, including non-axisymmetric effects, and, subsequently, subtract the best fit model to the observed velocity field, we investigate how the velocity residuals are related to the presence of young stellar activity. With this purpose, we model H I velocity maps from THINGS (Walter et al. 2008) and attempt an interpretation of the nature of the velocity deviations, and, eventually, compare them with star formation tracers maps provided from SINGS (Kennicutt et al. 2003).

To attain this goal, we model the velocity H I maps $v_{obs}(x, y)$ including also the effects due to a non-axisymmetric potential, describing $v_{obs}(x, y)$ in terms of Fourier series. Given the approximate cylindrical symmetry for galaxy disks, it is sensible to treat this problem in polar coordinates, which facilitates the analysis and the modeling. We treat the problem in terms of perturbation theory. Accordingly, a gas particle responds to a perturbation in the potential with harmonic oscillations around an equilibrium point, the guiding center, which describes a circular orbit as if in an axisymmetric potential.

3.1 Overview

The next sections will describe how we formulate a kinematic model for the gas velocity field of a galaxy in terms of gravitationally induced non-circular motions, so that for a given perturbation the observed and the model velocity fields, v_{obs} and v_{mod}, can be straightforwardly compared. A non-axisymmetric perturbation to the gravitational potential induces harmonic oscillations in the

orbits of gas particles, which describe a type of epicycles about circular orbits (§ 3.2). These oscillations ensue a composition of radial and azimuthal motions v_R and v_θ, which ultimately reflect in a velocity map observed with a given viewing angle (§ 3.3). Alternatively, given v_R and v_θ, the analytic form of the velocity map can be rewritten in terms of Fourier series. Finally, with these prescriptions and for a given class of perturbation, i.e. a bar (§ 3.4) or a spiral-like perturbation (§ 3.4.2), the corresponding model velocity field can be constructed in terms of Fourier components and compared to the observed velocity field.

Among the galaxies of the THINGS sample, in order to facilitate our analysis as much as possible, we select a galaxy with a regular velocity field, that is, without strong distortions along the minor axis, or evident asymmetries, or tidal interactions. Specifically, we apply our method to the galaxy NGC 3184 (see Fig. 3.3). However, we also test the opposite extreme of this criterial selection, applying our method to the galaxy NGC 2903, which is characterized by a twist in the position angle evidenced by the distortion of the velocity field along the minor axis (see Fig. 3.5).

3.2 Non-Axisymmetric Potential

A non-axisymmetric potential can be described as the sum of an axisymmetric term and a perturbation term, assuming that such perturbation is weak:

$$\Phi(R,\varphi) = \Phi_0(R) + \Phi_1(R,\varphi), \tag{3.1}$$

where we denote hereafter with the index "0" the axisymmetric term and with the index "1" the perturbation term. The analytic approximate solution to the problem can be obtained following the formalism adopted in Binney & Tremaine (1987, pp.146-148). We rewrite the polar coordinates as:

$$R(t) = R_0 + R_1(t) \qquad \varphi(t) = \varphi_0(t) + \varphi_1(t), \tag{3.2}$$

where the perturbative terms R_1 and φ_1 are assumed to be small with respect to the terms R_0 and φ_0 of circular orbits. We suppose that the perturbation is rotating with a steady pattern speed Ω_p, and consider the problem in the rest frame of the perturbation with polar coordinates (R,φ). We are looking for closed loop orbits in an axisymmetric potential with a weak perturbation. The treatment is closely related to the epicyclic theory (Lindblad & Lindblad 1994). The solution, in fact, will describe the orbits as small oscillations around the guiding center (R_0,φ_0). In the potential Φ of Eq. 3.1 the equations of the motion of a gas particle in the rest frame of the perturbation are:

$$\ddot{R}_1 + \Lambda\,\dot{R}_1 + \kappa_0^2\,R_1 = -\left[\frac{\partial\Phi_1}{\partial R}\right]_{R_0} - 2\,\frac{\Omega_0}{R_0}\int_{t_0}^{t} dt\,\left[\frac{\partial\Phi_1}{\partial\varphi}\right]_{R_0}, \tag{3.3}$$

$$\dot{\varphi}_1 + 2\,\Omega_0\,\frac{R_1}{R_0} = -\frac{1}{R_0^2}\int_{t_0}^{t} dt\,\left[\frac{\partial\Phi_1}{\partial\varphi}\right]_{R_0}, \tag{3.4}$$

where $\dot{\varphi}_0 = \Omega_0 - \Omega_p$, Ω_0 is the angular velocity of the guiding center, κ_0 is the epicyclic frequency:

$$\kappa_0^2 \equiv \left(3\,\Omega^2 + \frac{d^2\Phi_0}{dR^2} \right)_{R_0} . \tag{3.5}$$

Since the gas is collisional we also introduce (as Wada 1994; Byrd et al. 1998) the damping term $\Lambda\,\dot{R}_1$ in the radial motion. We neglect for simplicity the damping in the azimuthal direction. Then, we can choose an analytic form for the perturbation:

$$\Phi_1(R,\varphi) = \Phi_R(R)\,\cos(m\,\varphi), \tag{3.6}$$

where $\Phi_R(R)$ is only function of R and $m \in \mathbb{N}, \quad m \neq 0$ denotes the harmonic order of the perturbation (e.g. a bar may be described a a perturbation of order $m = 2$), therefore the Eq. 3.3 and Eq. 3.4 become:

$$\ddot{R}_1 + \Lambda\,\dot{R}_1 + \kappa_0^2\,R_1 = -\left[\frac{\partial\Phi_R}{\partial R} + \frac{2\,\Omega\,\Phi_R}{R\,(\Omega - \Omega_p)} \right]_{R_0} \cos(m\varphi_0), \tag{3.7}$$

$$\dot{\varphi}_1 + 2\,\Omega_0\,\frac{R_1}{R_0} = -\frac{\Phi_R}{R_0^2\,(\Omega_0 - \Omega_p)}\,\cos(m\varphi_0). \tag{3.8}$$

3.2.1 Solutions

The Eq. 3.7 is the equation of a damped driven harmonic oscillator in $R_1(t)$. The natural frequency of this particular harmonic oscillator is the epicyclic frequency κ_0, which is basically dictated by the potential Φ_0, and therefore is a function of radius. Here, the driving force is due to the perturbation and its amplitude is oscillating with a frequency $m\,(\Omega_0 - \Omega_p)$. Therefore we look for a solution with the form:

$$R_1(t) = A\,\cos(m\varphi_0 - \delta), \tag{3.9}$$

where (without going into detailed mathematics, but also cf. Sakamoto et al. 1999; Wong, Blitz, & Bosma 2004):

$$A = -\left[\frac{\partial\Phi_R}{\partial R_0} + \frac{2\,\Omega_0\,\Phi_R}{R_0\,(\Omega_0 - \Omega_p)} \right] \frac{1}{|\Delta|\,\sqrt{1 + \tan^2\delta}}, \tag{3.10}$$

$$\tan\delta = \frac{2m\,\Lambda\,(\Omega_0 - \Omega_p)}{\Delta}, \tag{3.11}$$

$$\Delta = \kappa_0^2 - m^2\,(\Omega_0 - \Omega_p)^2. \tag{3.12}$$

After substituting Eq. 3.9 into Eq. 3.8 we look for a solution of Eq. 3.8 of the form:

$$\varphi_1(t) = -B\,\sin(m\varphi_0 - \beta), \tag{3.13}$$

where:

$$B = |E|\,\sqrt{1 + F^2 + 2F\,\cos\delta}, \tag{3.14}$$

$$E = \frac{2A\,\Omega_0}{m\,R_0\,(\Omega_0 - \Omega_p)}, \tag{3.15}$$

$$F = \frac{\Phi_R}{2A\, v_c\, (\Omega_0 - \Omega_p)}, \tag{3.16}$$

$$\tan\beta = \frac{\sin\delta}{\cos\delta + F}. \tag{3.17}$$

Analytic Form for the Perturbation

The analytical expression of the non-axisymmetric potential Φ_R is given by:

$$\Phi_R = \varepsilon_R\, \Phi_0(R), \tag{3.18}$$

with the appropriate function $\varepsilon_R(R)$ the perturbative potential remains everywhere a small fraction of the axisymmetric part. Using, for example, a Toomre disk for the axisymmetric part, and following Sanders (1977):

$$\varepsilon_R = \varepsilon_0\, \frac{a^{2\nu-2}\, R^2}{(R^2 + a^2)^\nu}, \tag{3.19}$$

where $\nu \geq 1$, and a is the length scale of a Toomre disk expressed by:

$$\begin{aligned} \Phi_T(R) &= -\frac{GM}{(R^2 + a^2)^{1/2}} \\ v_T^2(R) &= \frac{GM\, R^2}{(R^2 + a^2)^{3/2}}. \end{aligned} \tag{3.20}$$

Therefore, adopting for example $\nu = 2$, we use for the non-axisymmetric part:

$$\Phi_R = -\varepsilon_0\, \frac{a^2}{R^2 + a^2}\, v_c^2. \tag{3.21}$$

For simplicity we obtain the length scale a by fitting the observed velocity curve to Eq. 3.20 and hold it fixed in our model Φ_R.

Resonances

The corotation resonance occurs for $\Omega_0 = \Omega_p$, where the guiding center and the perturbation corotate. There are two other resonances, also known as Lindblad resonances, which occur when frequency of the driving force equals the natural frequency of the harmonic oscillator, that is the epicyclic frequency. The condition is given by $\Delta = 0$, or equivalently:

$$m(\Omega_0 - \Omega_p) = \pm\kappa_0. \tag{3.22}$$

Due to the presence of the damping term the amplitude of the oscillations does not diverge, but it has only a limited maximum.

3.3 The Line of Sight Velocity Map

We first derive the velocity components for a single orbit, afterwards, we will extend the solution to a gaseous disk, and, finally, compare the projected velocity components with the velocity map in terms of Fourier series.

3.3.1 Single Orbit

In a frame at rest with respect to the observer, and described in polar coordinates (R, θ), we obtain the radial velocity component by substituting the solutions for R_1 and φ_1 of Eq.3.9 and Eq. 3.13, respectively into the Eq. 3.2, and retaining only the first order terms:

$$v_R = \dot{R} = -v_c \frac{A}{R_0} m(1-\omega_p) \sin(m\varphi_0 - \delta), \tag{3.23}$$

where $\omega_p \equiv \Omega_p/\Omega_0$, and the azimuthal velocity component:

$$\begin{aligned} v_\theta &= v_\varphi + R\Omega_p \\ &= R(\dot{\varphi} + \Omega_p) \\ &= v_c \left[1 + \frac{A}{R_0} \cos(m\varphi_0 - \delta) - B\, m(1-\omega_p) \cos(m\varphi_0 - \beta)\right]. \end{aligned} \tag{3.24}$$

3.3.2 Gaseous Disk Orbits

For the case of multiple orbits, e.g. for a gas disk, the observed coordinates (R_{map}, φ_{map}) on a velocity map do not necessarily correspond to the orbital coordinates (R_0, φ_0). We should evaluate the corresponding point (R_0, φ_0) for a given observed point (R_{map}, φ_{map}), and the velocity that we have previously evaluated at R_0 should now be evaluated at $R_{orb} = R_0 + R_1$ and $\varphi_{orb} = \varphi_0 + \varphi_1$, we therefore apply the corrections (Schoenmakers, Franx, & de Zeeuw 1997):

$$\begin{aligned} v_c(R_0) &= v_c(R_{map}) \left[1 - \frac{R_1}{R_0} \frac{d\ln v_c(R_{map})}{d\ln R_{map}}\right] \\ \omega_p(R_0) &= \omega_p(R_{map}) \left[1 - \frac{R_1}{R_0} \frac{d\ln \omega_p(R_{map})}{d\ln R_{map}}\right]. \end{aligned} \tag{3.25}$$

Substituting the corrections into v_θ and v_R, and retaining only the first order terms yield:

$$v_R = -v_c \frac{A}{R_0} m(1-\omega_p) \sin(m\varphi_0 - \delta), \tag{3.26}$$

which remains unchanged, and

$$v_\theta = v_c \left[1 + \frac{A}{R_0}(1-\alpha) \cos(m\varphi_0 - \delta) - B\, m(1-\omega_p) \cos(m\varphi_0 - \beta)\right] \tag{3.27}$$

where

$$\alpha \equiv \frac{d\log v_c}{d\log R}. \tag{3.28}$$

3.3.3 Harmonic Expansion of the Velocity Field

At this point, we compare the perturbed observed velocity map, described in terms of the radial and azimuthal components here derived, with the expansion

in Fourier series of the velocity map. The observed velocity map is given by:

$$v_{obs} = v_{sys} + \sin i \, (v_\theta \, \cos\psi + v_R \, \sin\psi) \tag{3.29}$$

where v_{sys} is the systemic velocity of the observed disk, and i the inclination, adopting $i = 0$ as the face-on configuration, and $\psi = 0$ indicates the kinematic position angle. We neglect here the velocity component orthogonal to the disk $v_z \cos i$. In the previous discussion we silently assumed that the perturbation in Eq. 3.6 is aligned with the long axis of the potential, given by $\varphi = 0$; we also assumed for simplicity that $\varphi_0 = (\Omega_0 - \Omega_p)t$. For a rigorous treatment we should instead insert two additional constants: (1) we should redefine the position of the perturbation by setting $\varphi \mapsto \varphi + \varphi_{pert}$ and (2) we should use more generally the time variable $t \mapsto t - t_0$. Since we want to solve the problem numerically (not analytically) we set for simplicity $\varphi_0 \mapsto \psi + \psi_0$, which will override the degeneracy between φ_{pert} and t_0. Using this setting and substituting the expressions in Eq. 3.26 and Eq. 3.27 into Eq. 3.29, the sine term in v_R becomes $\sin(m\varphi_0 - \delta) \mapsto \sin(m(\psi + \psi_0) - \delta)$ and the two cosine terms in v_θ become $\cos(m\varphi_0 - \delta) \mapsto \cos(m(\psi + \psi_0) - \delta)$ and $\cos(m\varphi_0 - \beta) \mapsto \cos(m(\psi + \psi_0) - \beta)$. Subsequently, using Werner's formulae, v_{obs} is then expressed only as a linear composition of terms in $\cos(n\psi)$ and $\sin(n\psi)$, with $n \in \mathbb{N}$. Comparing this expression with the Fourier expansion of the velocity map:

$$v_{obs} = c_0 + \sum_{n=1}^{+\infty} \left[c_n \, \cos(n\psi) + s_n \, \sin(n\psi) \right], \tag{3.30}$$

except for c_0 and c_1, all the terms c_n and s_n for $n \neq m \pm 1$ are zero. For a perturbation of order m the non-zero terms in the velocity field are therefore:

$$\begin{aligned}
c_0 &= v_{sys} \\
c_1(r) &= v_\star(r) \equiv v_c(r) \, \sin i \\
c_{m-1}(r) &= v_\star \left\{ \frac{A}{2r} \, [1 - \alpha - m(1 - \omega_p)] \, \cos(m\psi_0 - \delta) + \right. \\
&\quad \left. - \frac{1}{2} \, B \, m(1 - \omega_p) \, \cos(m\psi_0 - \beta) \right\} \\
s_{m-1}(r) &= -v_\star \left\{ \frac{A}{2r} \, [1 - \alpha - m(1 - \omega_p)] \, \sin(m\psi_0 - \delta) + \right. \\
&\quad \left. - \frac{1}{2} \, B \, m(1 - \omega_p) \, \sin(m\psi_0 - \beta) \right\} \\
c_{m+1}(r) &= v_\star \left\{ \frac{A}{2r} \, [1 - \alpha + m(1 - \omega_p)] \, \cos(m\psi_0 - \delta) + \right. \\
&\quad \left. - \frac{1}{2} \, B \, m(1 - \omega_p) \, \cos(m\psi_0 - \beta) \right\} \\
s_{m+1}(r) &= -v_\star \left\{ \frac{A}{2r} \, [1 - \alpha + m(1 - \omega_p)] \, \sin(m\psi_0 - \delta) + \right.
\end{aligned} \tag{3.31}$$

$$-\frac{1}{2}\,B\,m(1-\omega_p)\,\sin(m\psi_0-\beta)\Big\}\,.$$

For example, a perturbation of order $m = 2$, as such a bar, would produce terms of order $m = 1$ and $m = 3$ in the velocity map (Schoenmakers et al. 1997). A lopsidedness, that is a perturbation of order $m = 1$, would instead produce terms of order $m = 0$ and $m = 2$ (Swaters et al. 1999).

3.3.4 Multiple Perturbation

For multiple perturbative components we can consider, as for Eq. 3.1, that the potential is given by the sum of an axisymmetric part and a perturbation term which is a series of small terms:

$$\Phi(R,\varphi) = \Phi_0(R) + \sum_n \Phi_n(R,\varphi), \tag{3.32}$$

where, again, the index "0" denotes the axisymmetric part and "n" the perturbation terms. The polar coordinates can be also be rewritten as:

$$R(t) = R_0 + \sum_n R_n(t) \qquad \varphi(t) = \varphi_0(t) + \sum_n \varphi_n(t). \tag{3.33}$$

If all the terms are small, in other words, if every single perturbation is weak, we can exploit the linearity of the solutions by neglecting the coupling between components, and treat each component individually and independently from the others. The harmonic terms $(c_n, s_n)_{mod}$ will therefore also be derived separately for each perturbative component, and the resulting set of harmonic terms will be the sum of the contribution of all the perturbative components. In this case each component will be described by its own set of parameters: the pattern speed $\Omega_{p,n}$, the initial position $\psi_{0,n}$, and the amplitude $\varepsilon_{0,n}$.

3.4 The Methodology: Bar Perturbation

The modeling of the velocity map is carried out in two main steps: one purely mathematical, which only serves as a gauge for the type of perturbation, and the other using the prescriptions here described. We need to preliminarily sample the map $v_{obs}(x,y)$ into polar coordinates $v_{obs}(r,\psi)$ to adapt the data to the geometry of the theoretical problem, where $r = r(x,y)$ and $\psi = \psi(x,y)$ using the tilted-disk geometry (e.g. Begeman 1989). We sample the velocity map into concentric ellipses of $6''$ width (representing concentric rings projected on the disk) holding the center fixed, and the inclination i and the position angle are here assumed as global constants.

3.4.1 Harmonic Decomposition and Reconstruction of the Velocity Field

First, we need to know the order of the perturbation, therefore we decompose v_{obs} into harmonics (c_n, s_n), and reconstruct the velocity field v_{harm}. The

decomposition into harmonics is carried out by fitting, at fixed radius $\hat{r}$, the function $c_0(\hat{r}) + \sum c_n(\hat{r})\,\cos(n\psi) + s_n(\hat{r})\,\sin(n\psi)$ to $v_{obs}(\hat{r},\psi)$. Repeating the operation for all radii one obtains the harmonics $(c_n(r), s_n(r))$. Subsequently we recursively calculate, for $N = 1$ to 10, the deviations of v_{obs} from v_{harm} using:

$$\chi^2(N) = \sum_{r,\psi} [v_{obs}(r,\psi) - v_{harm,\,N}(r,\psi)]^2, \tag{3.34}$$

where N is the order of the last term in the equation:

$$v_{harm,\,N}(r,\psi) = c_0(r) + \sum_{n=1}^{N} [c_n(r)\,\cos(n\psi) + s_n(r)\,\sin(n\psi)] \tag{3.35}$$

Additionally, for $N = 1$ we set $s_1 = 0$ and $c_0 = \text{const}$, since in an unperturbed velocity field we expect that the sole non-zero terms are $c_0 = v_{sys}$ and $c_1 = v_c \sin i$. As N increases, the quality of the harmonic reconstruction $v_{harm,\,N}$ of the velocity field improves, since the model can mimic higher frequency features, and thus $\chi^2(N)$ decreases. The limit of $\chi^2(N)$ for $N \gg 1$ is basically given by the RMS of the data. The goal is to determine for which N_{limit} $\chi^2(N)$ decreases the most rapidly (and assume $N_{limit} - 1$ as the order of the perturbation). Note that $v_{harm,\,N}$ represents only a smoothed version of v_{obs} and there is no physical model behind this procedure.

Model of the Velocity Field: Bar Perturbation

The harmonics $(c_n, s_n)_{obs}$ expressed as function of radius are independent to each others. Our goal is to find a smoothed function (of R) that describes the $(c_n, s_n)_{obs}$. For a given perturbation of order m the harmonics $(c_n, s_n)_{mod}$ are formally expressed by Eqs. 3.31. In order to obtain a map v_{mod} we do χ^2 fitting of the model $(c_n, s_n)_{mod}$ to the observed $(c_n, s_n)_{obs}$ as function of R, where the model depends on a set of parameters, in particular, the pattern speed Ω_p, the damping constant $\lambda \equiv \Lambda/\Omega_0$, the initial position ψ_0, and the amplitude ε_0.

We apply these prescription to the H I velocity field of the galaxy NGC 3184. In Fig. 3.3 we plot the integrated H I column density and the velocity field. For comparison, we also plot a circular velocity field model and the corresponding residuals map. Here, we use a model of a perturbation of order $m = 2 + 4$, constituted by a bar ($m = 2$) and a thin component ($m = 4$) with the same pattern speed Ω_p, end-on position ψ_0, scale parameter a, and damping constant λ. Each component is characterized by an amplitude $\varepsilon_{0,m}$ for the perturbation. The results of the best fit model for the harmonics are plotted in Fig. 3.1. The maps of the model and the velocity residuals are plotted on top side of Fig. 3.4. The residuals are of amplitude comparable to those of the simple circular velocity model in Fig. 3.3.

Following the same procedure, we also apply a model of a double bar perturbation of order $m = 2 + 4$ each to the galaxy NGC 2903. The observed harmonics and the best fit model harmonics are plotted in Fig. 3.8. The two pattern speeds resulting from the fit have amplitude $\Omega_p \simeq 18\,\mathrm{km\,s^{-1}\,kpc^{-1}}$ and

$\Omega_p \simeq 90\ \mathrm{km\,s^{-1}\,kpc^{-1}}$. Note that the faster pattern speed is consistent with a small bar, whose maximum influence to the velocity field occurs near corotation (e.g. Zhang & Buta 2007), that is ~ 4 kpc, as indicated by the harmonics in Fig. 3.8. Consistently, the H band image (specifically from 2MASS) displays a central thin bar of ~ 4 kpc of radius. The velocity field, the circular velocity model, the perturbation model, and the corresponding residual maps are plotted in Fig. 3.5. Apparently, the location of the spiral arms, indicated by the contours in Fig. 3.5, does not seem to be strongly related to the pattern of the residuals map.

3.4.2 Spiral Perturbation

We consider a spiral perturbation as a perturbation whose angular phase is non-constant (cf. Canzian & Allen 1997, for a similar analysis), which, in particular, has a monotonic phase shift $f_R(R)$ expressed as sole function of radius:

$$\Phi_1(R,\varphi) = \Phi_R(R)\,\cos(m\,\varphi - f_R), \tag{3.36}$$

which is a generalization for the Eq. 3.6. We use the expression for a logarithmic spiral:

$$f_R = \log\left(1 + \frac{R}{R_w}\right), \tag{3.37}$$

where the parameter R_w denotes the spiral winding. Using this form for the perturbation in Eq. 3.3 and Eq. 3.4 we obtain:

$$\begin{aligned} \ddot{R}_1 + \Lambda\,\dot{R}_1 + \kappa_0^2\,R_1 = \quad & - \left[\frac{\partial\Phi_R}{\partial R} + \frac{2\,\Omega\,\Phi_R}{R\,(\Omega-\Omega_p)}\right]_{R_0} \cos(m\varphi_0 - f_R) \;+ \\ & - \left[\Phi_R\,\frac{\partial f_R}{\partial R}\right]_{R_0} \sin(m\varphi_0 - f_R), \end{aligned} \tag{3.38}$$

$$\dot{\varphi}_1 + 2\,\Omega_0\,\frac{R_1}{R_0} = -\frac{\Phi_R}{R_0^2\,(\Omega_0-\Omega_p)}\;\cos(m\varphi_0 - f_R). \tag{3.39}$$

Solving for the harmonic oscillator equation similarly as for Eq. 3.7 and Eq. 3.8, we find a solution for Eq. 3.38 in the form:

$$R_1(t) = A\,\cos(m\varphi_0 - f_R - \delta) \tag{3.40}$$

where:

$$\delta = \gamma + \eta \tag{3.41}$$

$$\tan\gamma = \frac{-\Phi_R\;\left.\frac{\partial f_R}{\partial R}\right|_{R_0}}{-\left[\frac{\partial\Phi_R}{\partial R} + \frac{2\,\Omega\,\Phi_R}{R\,(\Omega-\Omega_p)}\right]_{R_0}} \tag{3.42}$$

$$\tan\eta = \frac{m\,\lambda\,(1-\omega_p)}{1+\alpha-\frac{m^2}{2}\,(1-\omega_p)^2} \tag{3.43}$$

$$A = \frac{\left|\frac{\partial \Phi_R}{\partial R} + \frac{2\,\Omega\,\Phi_R}{R\,(\Omega-\Omega_p)}\right|_{R_0}}{|\Delta|} \sqrt{\frac{1+\tan^2\gamma}{1+\tan^2\eta}}. \tag{3.44}$$

Substituting Eq. 3.40 into Eq. 3.39 we find a solution of Eq. 3.39 of the form:

$$\varphi_1(t) = -B\,\sin(m\varphi_0 - f_R - \beta), \tag{3.45}$$

where:

$$B = |E|\,\sqrt{1+F^2+2F\,\cos(\gamma+\eta)} \tag{3.46}$$

$$E = \frac{2A\,\Omega_0}{m\,R_0\,(\Omega_0-\Omega_p)} \tag{3.47}$$

$$F = \frac{\Phi_R}{2A\,v_c\,(\Omega_0-\Omega_p)} \tag{3.48}$$

$$\tan\beta = \frac{\sin\delta}{\cos(\gamma+\eta)+F}. \tag{3.49}$$

Analytic Form for the Perturbation

The analytic expression of the non-axisymmetric potential Φ_R is given by $\Phi_R = \varepsilon_R\,\Phi_0$, where we choose a functional form for ε_R, such that the model Φ_R can mimic the type of perturbation, e.g. the effect of a bar has a maximum amplitude towards the center and fades rapidly out with the radius, whereas the effect of spiral arms remains constant also at large radii. Therefore we use two types of functions ε_R:

$$\varepsilon_R = \begin{cases} \varepsilon_0\,\frac{a^{2\nu-2}\,R^2}{(R^2+a^2)^\nu} & \text{(central)} \\ \varepsilon_0\,\frac{R^{2\nu}}{(R^2+a^2)^\nu} & \text{(constant)} \end{cases} \tag{3.50}$$

Using Eq. 3.50 with Eq. 3.20 and adopting $\nu = 2$ we obtain the functional form for the non-axisymmetric part:

$$\Phi_R = \begin{cases} -\varepsilon_0\,\frac{a^2}{R^2+a^2}\,v_c^2 & \text{(central)} \\ -\varepsilon_0\,\frac{R^2}{R^2+a^2}\,v_c^2 & \text{(constant)} \end{cases} \tag{3.51}$$

Harmonic Expansion of the Velocity Field

The derivation of the final expressions of the harmonic coefficients can be carried out similarly as for the previous case. Using the new solutions into v_θ and v_R, and substituting into Eq. 3.29, it can be shown that the Eqs. 3.31 now become:

$$\begin{aligned} c_0 &= v_{sys} \\ c_1(r) &= v_\star(r) \equiv v_c(r)\,\sin i \\ c_{m-1}(r) &= v_\star \left\{ \frac{A}{2r}\,[1-\alpha-m(1-\omega_p)]\,\cos(m\psi_0 - f_R - \gamma - \eta) + \right. \end{aligned} \tag{3.52}$$

$$
\begin{aligned}
& -\frac{1}{2}\, B\, m(1-\omega_p)\, \cos(m\psi_0 - f_R - \beta)\Big\} \\
s_{m-1}(r) &= -v_\star \left\{ \frac{A}{2r}\, [1-\alpha-m(1-\omega_p)]\, \sin(m\psi_0 - f_R - \gamma - \eta) + \right. \\
& \left. -\frac{1}{2}\, B\, m(1-\omega_p)\, \sin(m\psi_0 - f_R - \beta) \right\} \\
c_{m+1}(r) &= v_\star \left\{ \frac{A}{2r}\, [1-\alpha+m(1-\omega_p)]\, \cos(m\psi_0 - f_R - \gamma - \eta) + \right. \\
& \left. -\frac{1}{2}\, B\, m(1-\omega_p)\, \cos(m\psi_0 - f_R - \beta) \right\} \\
s_{m+1}(r) &= -v_\star \left\{ \frac{A}{2r}\, [1-\alpha+m(1-\omega_p)]\, \sin(m\psi_0 - f_R - \gamma - \eta) + \right. \\
& \left. -\frac{1}{2}\, B\, m(1-\omega_p)\, \sin(m\psi_0 - f_R - \beta) \right\}.
\end{aligned}
$$

Model of the Velocity Field: Spiral Perturbation

Similarly to the previous section we operate a χ^2 fitting of the model coefficients $(c_n, s_n)_{mod}$, formally expressed by Eqs. 3.52, to the observed coefficients $(c_n, s_n)_{obs}$, where the model will depend on the set of parameters: the pattern speed Ω_p, the damping constant λ, the initial position ψ_0, and the amplitude ε_0, and the spiral winding R_w.

We apply these prescription again to the velocity field of NGC 3184. In particular, the model is described by two independent components of order $m = 1 + 2$, where for each component we adopted individual parameters for $\Omega_{p,m}$, $\psi_{0,m}$, $\varepsilon_{0,m}$, a_m, and $R_{w,m}$. The harmonics of the overall model are the sum of the harmonics of each individual perturbation, as described in § 3.3.4. The resulting best fit model for the harmonics is plotted in Fig. 3.2, and the maps of the field model and the velocity residuals are plotted on bottom of Fig 3.4. Apparently, even by rendering the perturbation more and more complex, the amplitude of the residuals does not decreases accordingly. This issue can be visualized in Fig. 3.6. The discrepancy $v_{obs} - v_{harm,m}$, between the observed velocity field and the harmonic reconstruction field up to a generic order m from Eq.3.35, decreases in terms of χ^2 (see Eq. 3.34) as a function of m. In comparison to pure reconstruction, which represents the lower limit discrepancy, the two presented models, $m = 2+4$ and $m = 1+2$ (indicated in Fig. 3.6 with a diamond and a square, respectively), do not reproduce substantial improvement, since the residual map still exhibits large residuals.

3.4.3 Second Order Corrections

Using Schoenmakers et al. (1997) corrections of Eq. 3.25 we derived in § 3.3.2 the expressions for v_θ and v_R approximated to the first order. Now if we repeat

the calculations retaining also the second order terms, we obtain:

$$v_R = -v_c \frac{A}{R_0} m \sin(m\varphi_0 - \delta) \left[1 - \omega_p + \frac{A}{R_0}(\omega_p - \alpha) \cos(m\varphi_0 - \delta)\right] \quad (3.53)$$

and

$$\begin{aligned} v_\theta &= v_c \left\{1 + \frac{A}{R_0} \cos(m\varphi_0 - \delta) \left[1 - \alpha - \alpha \frac{A}{R_0} \cos(m\varphi_0 - \delta)\right] + \right. \quad (3.54) \\ &- \left. B\, m \cos(m\varphi_0 - \beta) \left[1 - \omega_p + \frac{A}{R_0}(\omega_p - \alpha) \cos(m\varphi_0 - \delta)\right]\right\}. \end{aligned}$$

Harmonic Expansion of the Velocity Field

Similarly to the first order case, we substitute v_θ and v_R into Eq. 3.29. The non-zero Fourier coefficients in the velocity field for a perturbation of order m are therefore:

$$\begin{aligned} c_0 &= v_{sys} \quad (3.55) \\ v_\star(r) &\equiv v_c(r) \sin i \\ c_1(r) &= v_\star \left[1 - \frac{1}{2}\alpha \frac{A^2}{R_0^2} - \frac{1}{2} m\, B \frac{A}{R_0} \sin(m\psi_0 - \beta) \sin(m\psi_0 - \delta)\right] \\ s_1(r) &= v_\star \left[\frac{1}{2} m\, B \frac{A}{R_0} \cos(m\psi_0 - \beta) \sin(m\psi_0 - \delta)\right] \\ c_{m-1}(r) &= v_\star \left\{\frac{1}{2}\frac{A}{R_0}[1 - \alpha - m(1 - \omega_p)] \cos(m\psi_0 - \delta) + \right. \\ &- \left. \frac{1}{2} m\, B (1 - \omega_p) \cos(m\psi_0 - \beta)\right\} \\ s_{m-1}(r) &= -v_\star \left\{\frac{1}{2}\frac{A}{R_0}[1 - \alpha - m(1 - \omega_p)] \sin(m\psi_0 - \delta) + \right. \\ &- \left. \frac{1}{2} m\, B (1 - \omega_p) \sin(m\psi_0 - \beta)\right\} \\ c_{m+1}(r) &= v_\star \left\{\frac{1}{2}\frac{A}{R_0}[1 - \alpha + m(1 - \omega_p)] \cos(m\psi_0 - \delta) + \right. \\ &- \left. \frac{1}{2} m\, B (1 - \omega_p) \cos(m\psi_0 - \beta)\right\} \\ s_{m+1}(r) &= -v_\star \left\{\frac{1}{2}\frac{A}{R_0}[1 - \alpha + m(1 - \omega_p)] \sin(m\psi_0 - \delta) + \right. \\ &- \left. \frac{1}{2} m\, B (1 - \omega_p) \sin(m\psi_0 - \beta)\right\} \\ c_{2m-1}(r) &= -v_\star \left\{\frac{1}{4}\frac{A^2}{R_0^2}[\alpha - m(\omega_p - \alpha)] \cos 2(m\psi_0 - \delta) + \right. \\ &+ \left. \frac{1}{4} m\, B \frac{A}{R_0}(\omega_p - \alpha) \cos(\delta + \beta)\right\} \end{aligned}$$

$$
\begin{aligned}
s_{2m-1}(r) &= v_\star \left\{ \frac{1}{4}\,\frac{A^2}{R_0^2}\,\left[\alpha + m\,(\omega_p - \alpha)\right]\,\sin 2(m\psi_0 - \delta) + \right. \\
&- \left. \frac{1}{4}\,m\,B\,\frac{A}{R_0}\,(\omega_p - \alpha)\,\sin(\delta + \beta) \right\} \\
c_{2m+1}(r) &= -v_\star \left\{ \frac{1}{4}\,\frac{A^2}{R_0^2}\,\left[\alpha + m\,(\omega_p - \alpha)\right]\,\cos 2(m\psi_0 - \delta) + \right. \\
&- \left. \frac{1}{4}\,m\,B\,\frac{A}{R_0}\,(\omega_p - \alpha)\,\cos(\delta - \beta) \right\} \\
s_{2m+1}(r) &= v_\star \left\{ \frac{1}{4}\,\frac{A^2}{R_0^2}\,\left[\alpha - m\,(\omega_p - \alpha)\right]\,\sin 2(m\psi_0 - \delta) + \right. \\
&+ \left. \frac{1}{4}\,m\,B\,\frac{A}{R_0}\,(\omega_p - \alpha)\,\sin(\delta - \beta) \right\} .
\end{aligned}
$$

The coefficients c_1 and s_1 of Eqs. 3.31 differ with those in Eqs. 3.55 by second order terms. The coefficients in $m \pm 1$ have remained unchanged. In Eqs. 3.55 the new coefficients in $2m \pm 1$ depend on second order terms. A perturbation of order $m = 2$ as such a bar would produce non-zero harmonics of order $m = 1$, $m = 3$, and $m = 5$, where the dominant harmonics are $m = 1$ and $m = 3$.

The application of this last example to the velocity field of NGC 3184 does not improve the residual map. In particular, we used two independent bar perturbations of order $m = 2$ each, described with a set of parameters $\Omega_{p,m}$, $\psi_{0,m}$, $\varepsilon_{0,m}$, and a_m. The resulting model is plotted in Fig. 3.7. Apparently, higher order corrections do not seem to influence much the amplitude of the harmonics.

3.5 Summary

Since a simple axisymmetric model for the velocity map v_{mod} does not accurately describe the observed velocity field v_{obs}, as shown e.g. in the residual map in Fig. 3.3 (bottom row) for the galaxy NGC 3184 and in Fig. 3.5 (central row) for the galaxy NGC 2903, we tried to devise an approach that could identify which wiggles and deviations from circular motions in the v_{obs} are due to the non-axisymmetry of the potential. In this aspect, we model the velocity maps v_{mod} using the perturbation formalism, where a perturbation to the potential reflects into v_{mod} producing the harmonic terms as in Eqs. 3.31, or Eqs. 3.52, or Eqs. 3.55. Subsequently, we estimate the order of the perturbation by evaluating the discrepancy between v_{obs} and $v_{harm,\,N}$ in terms of χ^2, where $v_{harm,\,N}$ is the harmonic reconstruction of v_{obs} up to the order N. Given that the perturbation is of order m, we derive from v_{obs} the coefficients $(c_n, s_n)_{obs}$ for $n = 0, \cdots, m+1$, or $n = 0, \cdots, 2m + 1$ if we use the second order corrections. Ultimately, we fit the harmonic terms $(c_n, s_n)_{mod}$ given by Eqs. 3.31, or Eqs. 3.52, or 3.55 to the observed harmonic terms $(c_n, s_n)_{obs}$ as function of R, where the model depends on a set of analytical parameters, in particular, Ω_p, λ, ψ_0, ε_0, a, and R_w. The best fit yields the harmonics to reconstruct v_{mod}, and the residuals are given by

$v_{obs} - v_{mod}$.

After subtracting from the observed velocity field the best fit model, obtained with different specifications, the residuals for the galaxy NGC 3184 are characterized by structures as large as few arcmin, corresponding to ~ 10 kpc, with a non-deprojected amplitude of $5-10$ km s^{-1} and without clear correspondence with the H I spiral arms. The three adopted methods, circular orbits, bar and spiral perturbations give similar results. The observed and the model coefficient for the galaxy NGC 3184 are plotted in Fig. 3.1 for a bar perturbation of order $m = 2 + 4$ and in Fig. 3.2 for a spiral perturbation of order $m = 1 + 2$ with two independent terms. The bar and the spiral perturbed velocity field model and the corresponding residuals are plotted in Fig. 3.4, and are in part resembling the distortions observed in Fig. 3.3. The residuals map obtained for the galaxy NGC 2903 exhibits non-deprojected deviations of $10 - 20$ km s^{-1} over few tens of kiloparsec scales, as large as the extent of the spiral arms. However, the deviations do not evidence a clear one-to-one correspondence with the spiral structure. For the galaxy NCG 2903, whose best fit model harmonics are plotted in Fig. 3.8, we attempt a bar model of two independent components of order $m = 2 + 4$ each. The model, as shown in Fig. 3.5, resembles in part the complexity of the observed velocity field. The kinematics of the model implies a bar with a pattern speed of $\Omega_p \simeq 90$ km s^{-1} kpc^{-1}, which seems consistent with the appearance of a bar in the stellar image traced by the H band.

3.5.1 Limitations of the Approach

Clearly, the attempts of fitting of the velocity fields using different models do not provide satisfactory results. In fact, the residuals for the galaxy NGC 3184 appear still as high as $\sim \pm 5 - 10$ km s^{-1} (non deprojected), not much lower than the residual were after subtracting a model of circular motions. Although, at first order, our kinematic prescriptions are able to recognize the small bar in NGC 2903 independently of the stellar image. Instead of the velocity residuals, we examine in Chap. 5 the velocity dispersion defined by the variance of the signal along the spectral dimension, which represents the minimum level of non laminar gas flows, typically ~ 10 km s^{-1}. Whilst, the mass-weighted residuals would add to the velocity dispersion a value of $\sim 5 - 10$ km s^{-1}, assuming that the deviations are in average isotropic, or $\sim 15 - 30$ km s^{-1}, assuming that the deviations are co-planar and considering an inclination $i = 16°$ for NGC 3184. We now discuss a few potential limitations of our approach.

On the one hand, there are some strong reservations with the assumptions for the analytic derivation of the potential. For instance, the perturbative potential could not be as smooth as in Eq. 3.21 and Eq. 3.51, but it has possibly higher radial variations. More importantly, the solutions of the harmonic oscillator obtained with the perturbational theory produces temporal dependences in the solutions of the orbits in a non-stationary regime for the perturbation. While the assumption of stationarity can in principle hold for a bar, which could maintain its structure over several orbital times, it is possibly not valid for spiral arms, since there are no confirmations that the spiral structure remains

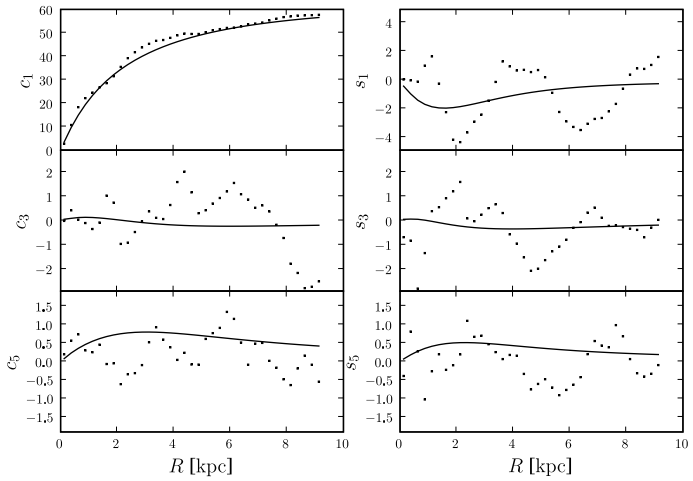

Figure 3.1: NGC 3184 – Harmonics for a model bar perturbation of order $m = 2 + 4$, following § 3.4. The dots represent the observed $(c_n, s_n)_{obs}$ (not deprojected by inclination), and the solid lines the best fit model $(c_n, s_n)_{mod}$.

stable. Moreover, not necessarily the perturbations have azimuthal harmonic order $m = 2$ or $m = 4$, but could even have a power spectrum with a whole distribution of higher orders (e.g. Elmegreen, Elmegreen, & Leitner 2003).

On the other hand, disk instabilities can produce deviations from the orbits induced by the gravitational potential of the galaxy. These instabilities have been described and numerically studied as magneto-rotational (Balbus & Hawley 1991; Piontek & Ostriker 2007) and magneto-hydrodynamical instabilities (Kim & Ostriker 2002, 2006; Kim, Ostriker, & Stone 2002), where magnetic fields buckle together large regions of orbiting gas, producing cloud collapse on large scales and/or reducing the shear in the spiral arms, whose motions deviate therefore from circular motions, and more importantly, from the orbits imposed by the potential. Even neglecting the influence of magnetic fields, large scale gravitational instabilities in (non-magnetized) gas are able to ensue deviations from a laminar flow of the gas orbiting in the galaxy potential (Li, Mac Low, & Klessen 2005, 2006). In this last case, spiral arms could be the source and the location of such deviations. Disk instabilities can not be easily modeled, and could have uncontrollable effects on the gas kinematics, and are difficult to be tackled analytically. Clearly, this class of deviation effects is related to star formation, since disk instabilities induce cloud collapse, but does not provide signatures of star formation feedback.

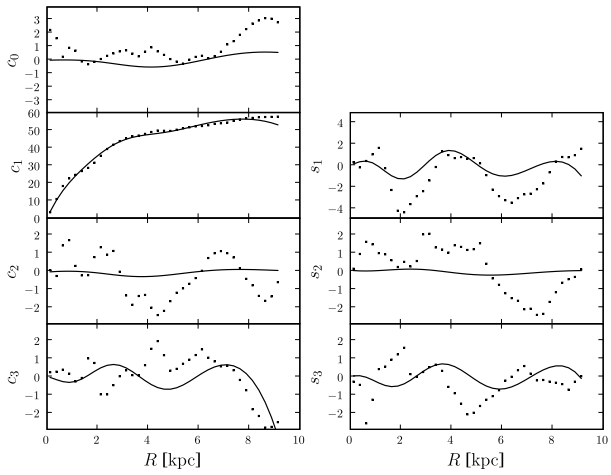

Figure 3.2: NGC 3184 – Harmonics for a model spiral perturbation of order $m = 1 + 2$, following § 3.4.2. The dots represent the observed $(c_n, s_n)_{obs}$, and the solid lines represent the best fit model $(c_n, s_n)_{mod}$.

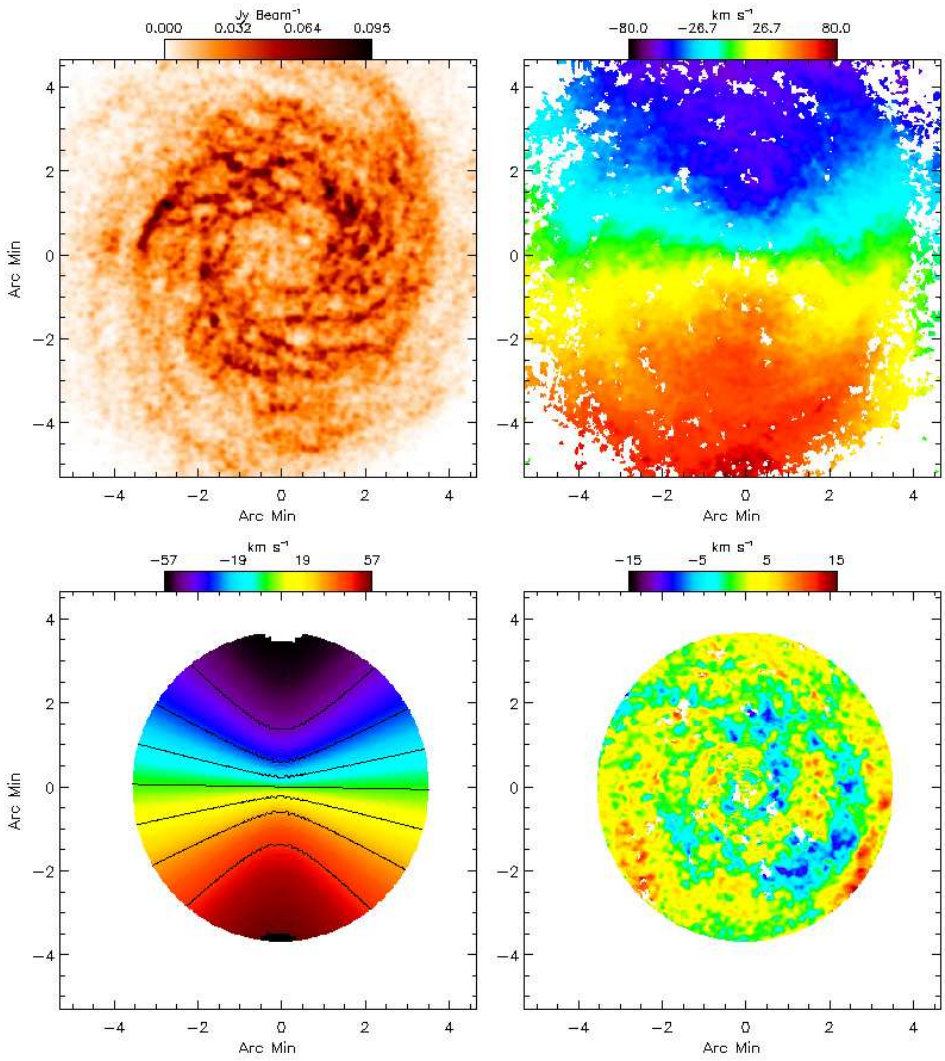

Figure 3.3: NGC 3184 – Top left: the H I integrated column density. Top right: the observed velocity field. Bottom left: the circular velocity field model. Bottom right: the residual map of a circular velocity field model $v_{obs} - v_{mod}$. The width of the ellipse encompasses the galaxy up to a galactocentric radius of $\sim 1\, r_{25}$.

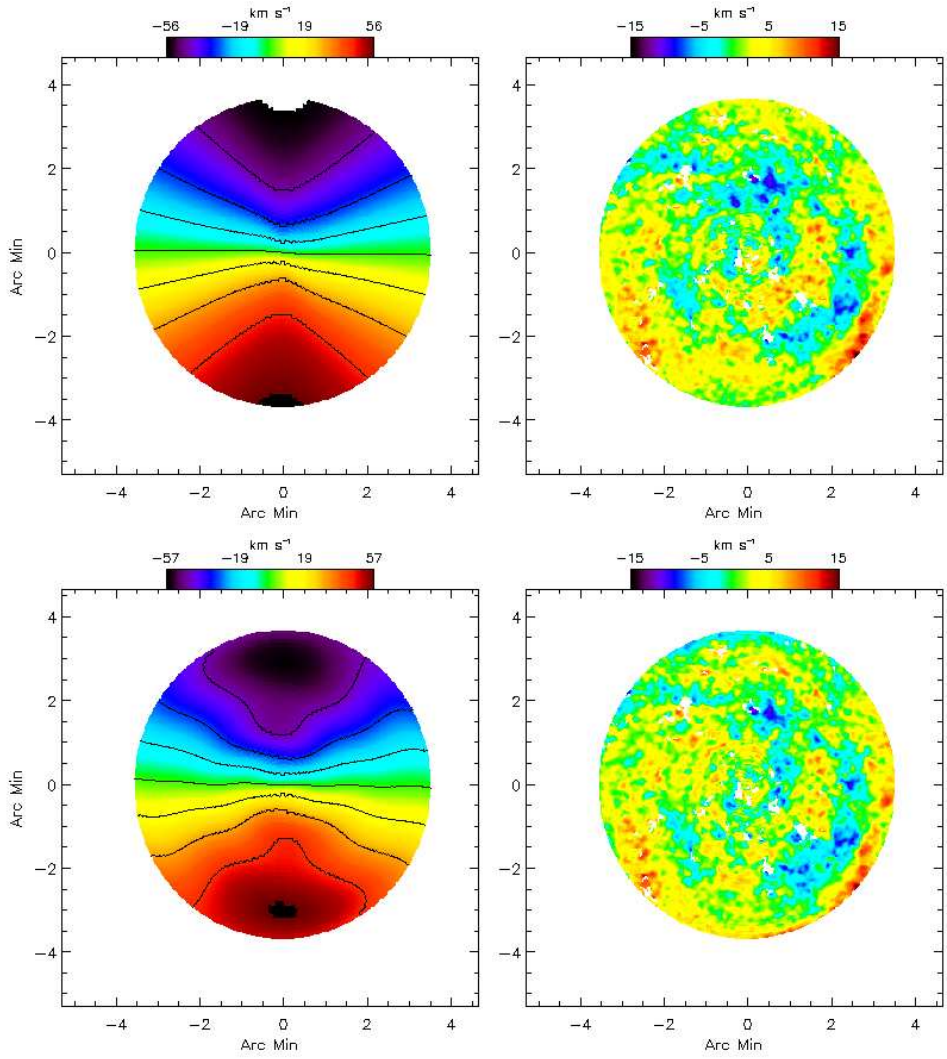

Figure 3.4: NGC 3184 – Top left: velocity field of a bar perturbation model (see § 3.4). Top right: residual map of a bar perturbation model. Bottom left: velocity field of a spiral perturbation model (see § 3.4.2). Bottom right: residual map of a spiral perturbation model.

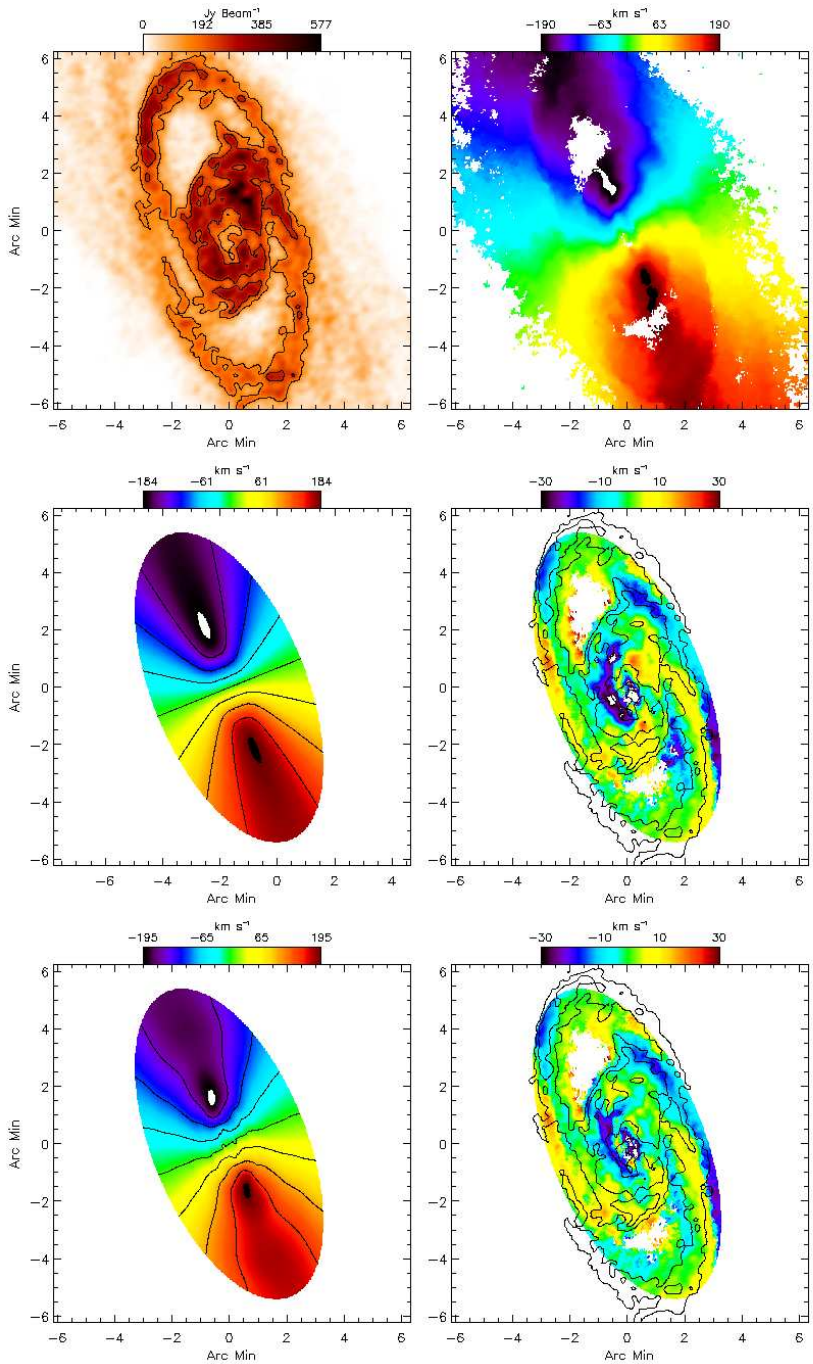

Figure 3.5: NGC 2903 – Top row: the H I integrated column density, and the observed velocity field. Central row: the circular velocity field model, and the corresponding residual map of the model $v_{obs} - v_{mod}$. Bottom row: the velocity field of a bar perturbation model (§ 3.4), and the corresponding residual map of the model. The contours indicate levels of H I column density.

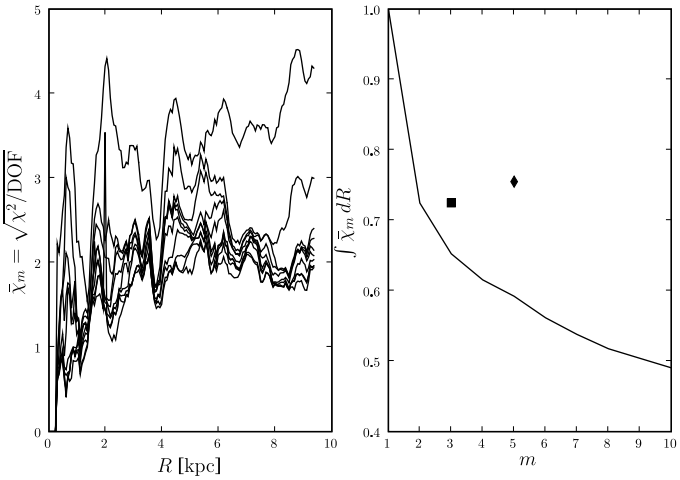

Figure 3.6: NGC 3184 – Left: the solid lines represent the reduced $\bar{\chi}_m = \sqrt{\chi^2/\mathrm{DOF}}$ as function of radius, where χ^2 is expressed by Eq. 3.34, the values for m going from 1 to 10 orderly denote the lines from the uppermost to the lowest. Right: the solid line represents the radial integral of $\bar{\chi}_m$ as function of m; the resulting discrepancies for a thin bar perturbation (§ 3.4) and a spiral perturbation (§ 3.4.2) are plotted for comparison with a diamond and square, respectively.

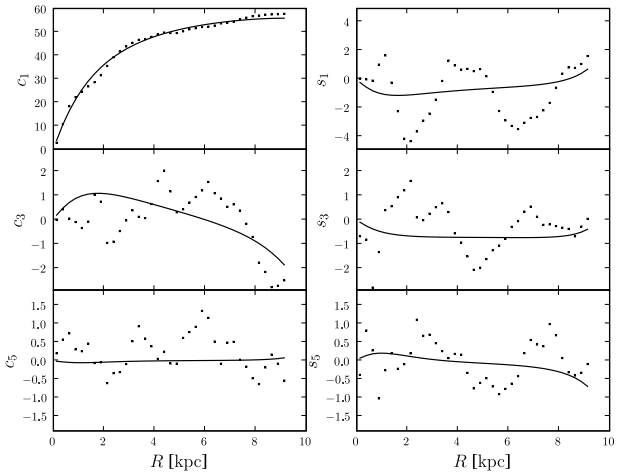

Figure 3.7: NGC 3184 – Harmonics for a model bar perturbation of order $m = 2 + 2$, using second order corrections, following § 3.4.3. The dots represent the observed $(c_n, s_n)_{obs}$, and the solid lines represent the best fit model $(c_n, s_n)_{mod}$.

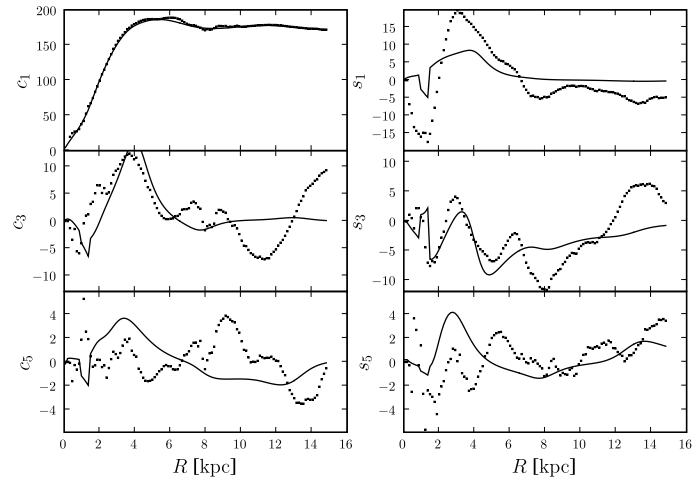

Figure 3.8: NGC 2903 – Harmonics for a model of a double bar perturbation of order $m = 2 + 4$ each, following § 3.4. The dots represent the observed $(c_n, s_n)_{obs}$ (not deprojected by inclination), and the solid lines the best fit model $(c_n, s_n)_{mod}$.

Bibliography

Balbus, S. A., & Hawley, J. F. 1991, ApJ, 376, 214

Begeman, K. G. 1989, A&A, 223, 47

Binney, J., & Tremaine, S. 1987, Princeton, NJ, Princeton University Press, 1987, 747 p.,

Byrd, G. G., Ousley, D., & dalla Piazza, C. 1998, MNRAS, 298, 78

Canzian, B., & Allen, R. J. 1997, ApJ, 479, 723

Elmegreen, B. G., Elmegreen, D. M., & Leitner, S. N. 2003, ApJ, 590, 271

Kennicutt, R. C., Jr., et al. 2003, PASP, 115, 928

Kim, W.-T., & Ostriker, E. C. 2002, ApJ, 570, 132

Kim, W.-T., & Ostriker, E. C. 2006, ApJ, 646, 213

Kim, W.-T., Ostriker, E. C., & Stone, J. M. 2002, ApJ, 581, 1080

Li, Y., Mac Low, M.-M., & Klessen, R. S. 2005, ApJL, 620, L19

Li, Y., Mac Low, M.-M., & Klessen, R. S. 2006, ApJ, 639, 879

Lindblad, P. O., & Lindblad, P. A. B. 1994, Physics of the Gaseous and Stellar Disks of the Galaxy, 66, 29

Piontek, R. A., & Ostriker, E. C. 2007, ApJ, 663, 183

Sakamoto, K., Okumura, S. K., Ishizuki, S., & Scoville, N. Z. 1999, ApJS, 124, 403

Sanders, R. H. 1977, ApJ, 217, 916

Schoenmakers, R. H. M., Franx, M., & de Zeeuw, P. T. 1997, MNRAS, 292, 349

Swaters, R. A., Schoenmakers, R. H. M., Sancisi, R., & van Albada, T. S. 1999, MNRAS, 304, 330

Wada, K. 1994, PASJ, 46, 165

Walter, F., et al. 2008, AJ, submitted

Wong, T., Blitz, L., & Bosma, A. 2004, ApJ, 605, 183

Zhang, X., & Buta, R. J. 2007, AJ, 133, 2584

Chapter 4

Timescales for Star Formation in Spiral Galaxies

based on D. Tamburro, H.-W. Rix, F. Walter, E. Brinks, W.J.G. de Blok, R.C. Kennicutt, and M.-M. Mac Low, 2008, AJ, submitted.

Abstract

We estimate a characteristic time-scale for star formation in the spiral arms of disk galaxies, going from atomic hydrogen (H I) to dust enshrouded massive stars. Drawing on high-resolution H I data from The H I Nearby Galaxy Survey (THINGS) and 24μm images from the Spitzer Infrared Nearby Galaxies Survey (SINGS) for a sample of 14 nearby disk galaxies, we measure the average angular offset between the H I and 24μm emissivity peaks as a function of radius. We model these offsets assuming an instantaneous kinematic pattern speed, Ω_p, and a time-scale, $t_{\mathrm{HI}\mapsto 24\,\mu\mathrm{m}}$, for the characteristic time-span between the dense H I phase and the existence of massive stars that heat the surrounding dust. Fitting for Ω_p and $t_{\mathrm{HI}\mapsto 24\,\mu\mathrm{m}}$, we find that the radial dependence of the observed angular offset (of the H I and 24μm emission) is consistent with this simple prescription; the resulting corotation radii of the spiral patterns are typically $R_{\mathrm{cor}} \simeq 2.7\,R_s$, consistent with methodologically independent estimates. The resulting values of $t_{\mathrm{HI}\mapsto 24\,\mu\mathrm{m}}$ for the sample are in the range 1–4 Myrs. We have explored the possible impact of non-circular gas motions on the estimate of $t_{\mathrm{HI}\mapsto 24\,\mu\mathrm{m}}$ and have found it to be substantially less than a factor of 2. This implies a rapid time-scale for massive star formation in spiral arm environments.

4.1 Introduction

Roberts (1969, hereafter R69) was the first to develop the scenario of spiral arm driven star formation in galaxy disks. In this picture a spiral density wave induces gravitational compression and shocks in the neutral hydrogen gas, which in turn leads to the collapse of (molecular) gas clouds that results in star formation. This work already pointed out the basic consequences for the relative geometry of the dense cold gas reservoir[1] from which to make the stars *vis-a-vis* the emergent young stars: when viewed from a reference frame that corotates with the density wave, the densest part of the H I lies at the shock (or just upstream from it), while the young stars lie downstream from the density wave. Using H I and the Hα as the tracers of the cold gas and Hα as the tracers of the young stars, respectively, R69 saw qualitative support in the data available at the time. In this picture, the characteristic timescale for this sequence of events is reflected in the typical angular offset, at a given radius, between tracers of the different stages of spiral arm driven star formation.

While this qualitative picture has enjoyed continued popularity, quantitative tests of the importance of spiral density waves as star formation trigger (Lin & Shu 1964) and of the time scales for the ensuing star formation have proven complicated. First, it has become increasingly clear that even in galaxies with grand design spiral arms, about half of the star formation occurs in locations not near the spiral arms (Elmegreen & Elmegreen 1986). Second, stars form from molecular clouds (not directly from H I) and very young star clusters are dust enshrouded at first. Moreover, the actual physical mechanism that appears to control the rate and overall location of star formation in galaxies is the gravitational instability of the gas and existing stars (e.g. Li, Mac Low, & Klessen 2005): stars only form above a critical density (Martin & Kennicutt 2001) which is governed by the Toomre (1964) criterion for gravitational instability as generalized by Rafikov (2001), although in galaxies with prominent spiral structure local gas condensations are governed by magneto-rotaional instabilities - spiral arms are regions of low shear where the tranfer of angular momentum is carried out by magnetic fields (Kim & Ostriker 2002, 2006). Obtaining high resolution, sensitive maps of all phases in this scenario (H I, molecular gas, dust enshrouded young stars, unobscured young stars) has proven technically challenging.

If the star formation originates from direct collapse of gravitationally unstable gas, and if the rotation curve and approximate pattern speed of the spiral arms are known, the geometric test suggested by R69 provides a time scale for the end-to-end (from H I to star formation) process of star formation, including an upper limit on the characteristic lifetime of molecular clouds prior to the peak of star formation. Of course, there are other ways of estimating the time scales that characterize the evolutionary sequence of the ISM, based on other physical arguments. However, other lines of reasoning have led to quite a wide range of varying lifetime estimates as discussed below.

[1] This paper pre-dates observational studies of molecular gas in galaxies.

Offsets between components such as CO and Hα emission in the disks of spiral galaxies have indeed been observed (Vogel, Kulkarni, & Scoville 1988; Garcia-Burillo, Guelin, & Cernicharo 1993; Rand & Kulkarni 1990; Scoville et al. 2001). Mouschovias, Tassis, & Kunz (2006) remarked that the angular separation between the dust lanes and the peaks of Hα emission found for nearby spiral galaxies (e.g. observed by Roberts 1969; Rots 1975) implied time scales of the order of 10 Myr. More recently Egusa, Sofue, & Nakanishi (2004), using the angular offset between CO and Hα in nearby galaxies, derived $t_{\mathrm{CO}\mapsto\mathrm{H}\alpha}$ to fall between values of 4 to 7 Myr.

Observationally, the H I surface density is found to correlate well with sites of star formation and emission from molecular clouds (Wong & Blitz 2002; Kennicutt 1998). The conversion time scale of H I$\mapsto$H$_2$ is a key issue since it determines how well the peaks of H I emission can be considered as potential early stages of star formation. H_2 molecules only form on dust grain surfaces in dusty regions that shield the molecules from ionizing UV photons. Their formation facilitates the subsequent building up of more complex molecules (e.g. Williams 2005). Within shielded clouds the conversion time scale H I$\mapsto$H$_2$ is given by $\tau_{\mathrm{H}_2} \sim 10^9/n_0$ yr, where n_0 is the proton density in cm^{-3} (Hollenbach & Salpeter 1971; Jura 1975; Goldsmith & Li 2005; Goldsmith, Li, & Krčo 2007). Given the inverse proportionality with n_0, the conversion time scale can vary from the edge of a molecular cloud ($\tau \simeq 4 \times 10^6$ yr, $n_0 \sim 10^3$) to the central region ($\tau \sim 10^5$ yr, $n_0 \sim 10^4$) where the density is higher. Local turbulent compression can further enhance the local density, and thus decrease the conversion timescale (Glover & Mac Low 2007). Thus, even short cloud formation timescales remain consistent with the H I$\mapsto$H$_2$ conversion timescale.

The subsequent evolution (see e.g. Beuther et al. 2007, for a review) involves the formation of cloud cores, initially starless, and then star cluster formation through accretion onto protostars, which finally become main sequence stars. High-mass stars evolve more rapidly than low-mass stars. Stars with $M \geq 5$ M$_\odot$ reach the main sequence in less than 1 Myr (Hillenbrand et al. 1993), while they are still deeply embedded and actively accreting. The O and B stars begin to produce an intense UV flux that photoionises the surrounding dusty environment within a few Myr, and subsequently become visible in the optical (Thronson & Telesco 1986). A different scenario is suggested by Allen (2002), in which young stars in the disks of galaxies produce H I from their parent H_2 clouds by photodissociation. According to this scenario, the H I should not be seen furthest upstream in the spiral arm, but rather between the CO and UV/Hα regions. Allen et al. (1986) indeed report observation of H I downstream of dust lanes in M83.

Several lines of reasoning, however, point towards longer star formation timescales and molecular cloud lifetimes, much greater than 10 Myr. Krumholz & McKee (2005) conclude that the star formation rate in the solar neighborhood is low. In fact, they point out that the star formation rate in the solar neighborhood is ~ 100 times smaller than the ratio of the masses of nearby molecular clouds to their free fall time $M_{\mathrm{MC}}/\tau_{\mathrm{ff}}$, which also indicates the rate of compression of molecular clouds. Individual dense molecular clouds have been argued

to stay in a fully molecular state for about 10-15 Myr before their collapse (Tassis & Mouschovias 2004), and to transform about 30% of their mass into stars in $\geq 7\,\tau_{\rm ff}$ ($\sim 10^6$ yr e.g. considering the mass of the Orion Nebula Cluster, ONC Tan, Krumholz, & McKee 2006). Large molecular clouds have been calculated to survive 20 to 30 Myr before being destroyed by the stellar feedback by Krumholz, Matzner, & McKee (2006). Based on observations, Palla & Stahler (1999, 2000) argue that the star formation rate in the ONC was low 10^7 yr ago, and that it increased only recently. Blitz et al. (2007), using a statistical comparison of cluster ages in the Large Magellanic Cloud to the presence of CO, found that the life time for giant molecular clouds is 20 to 30 Myr.

Other studies conclude that the timescales for star formation are rather short, however. Hartmann (2003) pointed out that the Palla-Stahler model is not consistent with observations since most of the molecular clouds in the ONC are forming stars at the same high rate. The stellar age or the age spread in young open stellar clusters is not necessarily a useful constraint on the star formation timescale: the age spread for example may result from independent and non simultaneous bursts of star formation (Elmegreen 2000). Ballesteros-Paredes & Hartmann (2007) pointed out that the molecular cloud life time must be shorter than the value of $\tau_{\rm MC} \simeq 10$ Myr suggested by Mouschovias, Tassis, & Kunz (2006). Also subsequent star formation must proceed very quickly, within a few Myr (Vázquez-Semadeni et al. 2005; Hartmann, Ballesteros-Paredes, & Bergin 2001). Prescott et al. (2007) found strong association between 24 μm sources and optical H II regions in nearby spiral galaxies. This provides constraints on the lifetimes of star forming clouds: the break out time of the clouds and their parent clouds is less or at most of the same order as the life time of the H II regions, therefore a few megayears. Dust and gas clouds must dissipate on a time scale not longer than 5–10 Myr.

In conclusion, all the previous studies here listed aim to estimate the life times of molecular clouds and/or the time scale separation between the compression of neutral gas and newly formed stars. Most of these studies are based on observations of star forming regions both in the Milky Way and in external galaxies, and in all cases the derived time scales lie in a range between a few megayears and several tens of megayears.

In this paper we examine a new method, described in § 4.2, for estimating the timescale to proceed from H I compression to star formation. We compare Spitzer Space Telescope/MIPS 24 μm data from the Spitzer Near Infrared Galaxies Survey (SINGS; Kennicutt et al. 2003) to 21-cm maps from The H I Nearby Galaxy Survey (THINGS; Walter et al. 2008) aided by the proximity of our targets, which allows for high spatial resolution. In § 4.3 we give a description of the data. The MIPS bands (24, 70 and 160 μm) are tracers of hot dust heated by UV and are therefore good indicators of recent star formation activity (see for example Dale et al. 2005). We used the band with the best resolution, 24 μm, which has been recognized as the best of the Spitzer bands for tracing star formation (Calzetti et al. 2005, 2007); the 8 μm Spitzer/IRAC band has even higher resolution but is contaminated by PAH features that undergo strong depletion in presence of intense UV radiation (Dwek 2005; Smith et al.

2007). In § 4.4 we describe how we use azimuthal cross-correlation to compare the H I and 24 μm images and derive the angular offset of the spiral pattern. This algorithmic approach minimizes possible biases introduced by subjective assessments. We describe our results in § 4.5 where we derive $t_{\mathrm{HI}\mapsto 24\,\mu\mathrm{m}}$ for our selection of objects. Finally we discuss the implications of our results in § 4.6 and draw conclusions in § 4.7.

4.2 Methodology

The main goal of this paper is to to estimate geometrically the timescales for spiral arm driven star formation using a simple kinematic model, examining the R69 arguments in light of state-of-the-art data. Specifically, we set out to determine the relative geometry of two tracers for different stages of star formation sequence in a sample of nearby galaxies, drawing on the SINGS and THINGS data sets (see § 4.3): the 24μm and the H I emission.

While the angular offset between these two tracers is an empirical model-independent measurement, a conversion into a SF timescale assumes *a)* that peaks of the H I trace material that is about to form a molecular cloud, and *b)* that the peaks of the 24μm emission trace the very young, still dust-enshrouded star-clusters, where their UV emission is absorbed and re-radiated into the mid- to far-infrared wavelength range ($\sim$ 5 μm to $\sim$ 500 μm). The choice of these particular tracers was motivated by the fact that they should tightly bracket the lifetime of molecular clouds, and by the availability of high-quality data from the SINGS and THINGS surveys. Note that a number of imaging studies in the near-IR have shown (e.g. Rix & Zaritsky 1995) that the large majority of luminous disk galaxies have a coherent, dynamically relevant spiral arm density perturbation. Therefore, this overall line of reasoning can sensibly be applied to a sample of disk galaxies.

We consider a radius in the galaxy disk where the spiral pattern can be described by a kinematic pattern speed, Ω_p, and the local circular velocity $v_c(r) \equiv \Omega(r) \times r$. Then two events separated by a time $t_{\mathrm{HI}\mapsto 24\,\mu\mathrm{m}}$will have a phase offset of:

$$\Delta\phi(r) = (\Omega(r) - \Omega_p)\, t_{\mathrm{HI}\mapsto 24\,\mu\mathrm{m}}, \tag{4.1}$$

where $t_{\mathrm{HI}\mapsto 24\,\mu\mathrm{m}}$ denotes the time difference between two particular phases that we will study here. If the spiral pattern of a galaxy indeed has a characteristic kinematic pattern speed, the angular offset between any set of tracers is expected to vary as a function of radius in a characteristic way. Considering the chronological sequence and defining the angular phase difference $\Delta\phi \equiv \phi_{24\,\mu\mathrm{m}} - \phi_{\mathrm{HI}}$ and adopting the convention that ϕ increases in the direction of rotation, we expect the qualitative radial dependence plotted in Figure 4.2: $\Delta\phi > 0$ where the galaxy rotates faster than the pattern speed, otherwise $\Delta\phi < 0$. Where $\Omega(R_{\mathrm{cor}}) = \Omega_p$, at the so-called corotation radius, we expect the sign of $\Delta\phi$ to change.

4.3 Data

The present analysis is based on the 21-cm emission line maps for the 14 disk galaxies listed in Table 4.1, which are taken from THINGS. These high quality Very Large Array observations provide data cubes with an angular resolution of $\simeq 6''$ and spectral resolution of 2.6 or 5.2 km s^{-1}. Since the target galaxies are nearby, at distances of 3 to 10 Mpc, the linear resolution of the maps corresponds to 100–300 pc. The H I data cubes of our target galaxies are complemented with near-IR images, which are in part public data. In particular, the majority of the THINGS galaxies (including all those in Table 4.1) have also been observed within the framework of the SINGS and we make extensive use of the 24 μm MIPS images. (see § 4.4.2). Figure 4.1 illustrates our data for one of the sample galaxies, NGC 5194. The 24 μm band image is shown in color scale, and the contours show the H I emission map. To obtain the exponential scale length of the stellar disk (see § 4.4), we used 3.6 μm IRAC images when available, otherwise we used H band images taken from the 2 Micron All-sky Survey (2MASS; Jarrett et al. 2003). To check the consistency of our results we used CO maps from the Berkeley Illinois Maryland Array Survey Of Nearby Galaxies (BIMA-SONG Helfer et al. 2003) for some of our target galaxies.

4.4 Analysis

All analysis in this paper started from fully reduced images and data cubes. On this data we carried out two main steps. First, we derived the rotation curve $v_c(r)$ of the H I and the geometrical projection parameters of the galaxy disk, and used these parameters to de-project the maps of the galaxies to face-on (see Table 4.1). Second, we sampled the face-on maps in concentric annuli. For each annulus we cross-correlated the corresponding pair of H I and 24 μm fluxes, in order to derive the angular offset between the H I and the 24 μm patterns as a function of radius.

For three of the galaxies listed in Table 4.1 (NGC 628, NGC 5194, and NGC 3627) we also measured the angular offset between the CO and 24 μm emission maps. If the ISM evolves sequentially from atomic into molecular gas, and subsequently initiates the formation of stars then, considering the kinematics expressed in Eq. 4.1, we expect the CO emission to lie in between the H I and the 24 μm.

4.4.1 Analysis of the H I Kinematics

For each object we applied the same general approach: we first performed adaptive binning of the H I data cube regions with low signal-to-noise (S/N) ratio using the method described by Cappellari & Copin (2003). From the resulting spatially binned data cubes we fit the 21-cm emission lines with a single Gaussian profile and use the parameterization to derive 1) the line of sight velocity map $v(x, y)$, given by the line centroid, and 2) the flux maps

$\mu_0(x,y) \equiv a(x,y)/(\sqrt{2\pi}\,\sigma(x,y))$, where a and σ are the Gaussian peak amplitude and width, respectively. Since we do not need to derive the rotation curve with high accuracy for the purpose of this paper, we limit our model to a co-planar rotating disk with circular orbits described by

$$v(x,y) = v_{\rm sys} + v_c(r)\,\sin i \cos\psi \tag{4.2}$$

where $v(x,y)$ is the observed velocity map along the line of sight (see Begeman 1989). For simplicity we assume here that the orbits are circular, though we address the issue of non-circular motions in § 4.5.4. By χ^2 minimization fitting[2] of the model function in Eq. 4.2 to the observed velocity map $v(x,y)$ we obtain the systemic velocity $v_{\rm sys}$, the inclination i and the position angle (PA) of the geometric projection of the disk on to the sky. Here ψ is the azimuthal angle on the plane of the inclined disk (not the sky) and is a function of i and PA. The line where $\psi = 0$ denotes the orientation of the line of nodes on the receeding side of the disk. The kinematic center (x_0, y_0) is fixed a priori and was defined as the central peak of either the IRAC 3.6 μm or the 2MASS H band image. The positions of the dynamical centers used here are consistent with those derived in Trachternach et al. (2008). We parameterized the deprojected rotation curve v_c with a four parameter arctan-like function (e.g., Rix et al. 1997)

$$v_c(r) = v_0\ (1+x)^{\beta}\ (1+x^{-\gamma})^{-1/\gamma} \tag{4.3}$$

where $x = r/r_0$. Here, r_0 is the turn-over radius, v_0 is the scale velocity, γ determines the sharpness of the turnover and β is the asymptotic slope at larger radii.

The values for the projection parameters i, and PA, the systemic velocity $v_{\rm sys}$, and the asymptotic velocity that have been obtained applying the approach here described, are consistent with the values reported in Table 4.1, obtained by de Blok et al. (2008).

4.4.2 Azimuthal Cross-Correlation

The central analysis step is to calculate by what angle $\Delta\phi$ the patterns of H I and 24 μm need to be rotated with respect to each other in order to best match. We used the kinematically determined orientation parameters, i and PA, to deproject both the H I and 24 μm images to face-on. To estimate the angular offset $\Delta\phi$ between the two flux images at each radius, we divide the face-on images into concentric rings of width $\sim 5''$ and extracted the flux within this annulus as function of azimuth. We then use a straightforward cross-correlation (CC) to search for phase lags in $f_{\rm HI}(\phi|r)$ versus $f_{24\,\mu{\rm m}}(\phi|r)$. In general, the best match between two discrete vectors x and y is realized by minimizing as function of the phase shift ℓ (also defined as *lag*) the quantity

$$\chi^2_{x,y}(\ell) = \sum_k [x_k - y_{k-\ell}]^2, \tag{4.4}$$

[2]The fitting has been performed with the `mpfit` IDL routine found at the URL: http://cow.physics.wisc.edu/∼craigm/idl/fitting.html

where the sum is calculated over all the N elements of x and y with $k = 0, 1, 2, ...N-1$. Specifically here, for a given radius $r = \hat{r}$ we consider for all discrete values of azimuth ϕ:

$$x_k = f_{\rm HI}(\phi_k|\hat{r}) \quad \text{and} \quad y_{k-\ell} = f_{24\,\mu{\rm m}}(\phi_{k-\ell}|\hat{r}) \tag{4.5}$$

Expanding the argument of the sum in Eq. 4.4 one obtains that $\chi^2(\ell)$ is independent of the terms $\sum_k x_k^2$ and $\sum_k y_{k-\ell}^2$, and χ^2 is minimized by maximization of:

$$cc_{x,y}(\ell) = \sum_k \left[x_k\, y_{k-\ell}\right], \tag{4.6}$$

which is defined as the CC coefficient. Here we used the normalized CC

$$cc_{x,y}(\ell) = \frac{\sum_k \left[(x_k - \bar{x})\,(y_{k-\ell} - \bar{y})\right]}{\sqrt{\sum_k (x_k - \bar{x})^2 \;\sum_k (y_k - \bar{y})^2}} \tag{4.7}$$

where $\bar{x}$ and $\bar{y}$ are the mean values of x and y respectively. Here the slow, direct definition has been used and not the fast Fourier transform method. The vectors are wrapped around to ensure the completeness of the comparison. With this definition the CC coefficient would have a maximum value of unity for identical patterns, while for highly dissimilar patterns it would be much less than one. We applied the definition in Eq. 4.7 using the substitutions of Eq. 4.5 to compute the azimuthal CC coefficient $cc(\ell)$ of the H I and the 24 μm images. The best match between the H I and the 24 μm signals is realized at a value $\ell_{\rm max}$ such that $cc(\ell_{\rm max})$ has its peak value. Since the expected offsets are small (only a few degrees) we search the local maximum around $\ell \simeq 0$. The method is illustrated in Figure 4.3, which shows that $cc(\ell)$ has several peaks, as expected due to the self-similarity of the spiral pattern.

We considered a range that encompasses the maximum of the $cc(\ell)$ profile, i.e. the central $\sim$ 100–150 data points around $\ell_{\rm max}$. This number, depending on the angular size of the ring, is dictated by the azimuthal spread of the spiral arms and the number of substructures (e.g. dense gas clouds, star clusters, etc.) per unit area. This corresponds, for example, to a width in ℓ of a few tens of degrees at small radii ($\sim 1'$), depending on the distance of the object, and a range in width of ℓ decreasing linearly with the radius. We interpolated $cc(\ell)$ around $\ell_{\rm max}$ with a fourth-degree polynomial using the following approximation: $cc(\ell) \simeq p_4(\ell) = \sum_{n=0}^{4} a_n\, \ell^n$ and calculated numerically (using the Python[3] package `scipy.optimize`) the peak value at $\ell_{\rm max}$, $p_4(\ell_{\rm max})$. By repeating the procedure for all radii, the angular offset H I$\mapsto$24 μm results in $\Delta\phi(r) = -\ell_{\rm max}(r)$. The direction or equivalently the sign of the lag $\ell_{\rm max}$ between two generic vectors x and y depends on the order of x and y in the definition of the CC coefficient. Notice that $cc_{x,y}(\ell)$ in Eq. 4.6 is not commutative, being $cc_{y,x}(\ell) = cc_{x,y}(-\ell)$. For $\ell_{\rm max} = 0$ the two patterns best match at zero azimuthal phase shift. The error bars for $\delta\ell_{\rm max}(r)$ have been evaluated through a Monte Carlo approach, adding normally distributed noise and assuming the expectation values of $\ell_{\rm max}$

[3] http://www.python.org

and $\delta\ell_{\rm max}$ as the mean value and the standard deviation, respectively, after repeating the determination $N = 100$ times.

Our analysis is limited to the radial range between low S/N regions at the galaxy centers and their outer edges. In the H I emission maps the S/N is low near the galaxy center, where the H I is converted to molecular H_2, whereas for the 24 μm band the emission map has low S/N near R_{25} (and in most cases already at $\sim 0.8\,R_{25}$). Regions with S/N < 3 in either the H I or 24 μm images have been clipped. We also ignore those points $\ell_{\rm max}$ with a coefficient $cc(\ell_{\rm max})$ lower than a threshold $cc \simeq 0.2$. We further neglect any azimuthal ring containing less than a few hundred points, which occurs near the image center and near R_{25}. The resulting values $\Delta\phi(r)$ are shown in Figure 4.4.

4.4.3 Disk Exponential Scale Length

We also determined the disk exponential scale length R_s for our sample using the `galfit`[4] algorithm (Peng et al. 2002). In particular, we fitted an exponential disk profile and a de Vaucouleurs profile to either the IRAC 3.6 μm or to the 2MASS H band image. As `galfit` underestimates the error on R_s (as recognized by the author of the algorithm), typically $\delta R_s/R_s < 1$ %, we therefore also used the IRAF task `ellipse` (Jedrzejewski 1987) to derive the radial surface brightness profile and fit R_s. After testing the procedure on a few objects, we noticed only small differences (of the order of the error bars in Table 4.1) when deriving R_s from the H band and the 3.6 μm band.

4.5 RESULTS

4.5.1 Angular Offset

With the angular offset $\Delta\phi(r) \equiv \langle\phi_{24\,\mu{\rm m}} - \phi_{\rm HI}\rangle(r)$, where ϕ increases in the direction of rotation, and the rotation curve $v_c(r)$ for each radial bin, we can rewrite Eq. 4.1 as:

$$\Delta\phi(r) = \left(\frac{v_c(r)}{r} - \Omega_p\right) \times t_{\rm HI\mapsto 24\,\mu m}, \tag{4.8}$$

where $\Omega(r) \equiv v_c/r$. Since $\Omega(r) > \Omega_p$ inside the corotation radius $R_{\rm cor}$, and $\Omega(r) < \Omega_p$ outside corotation, we expect $\Delta\phi(r) > 0$ for $r < R_{\rm cor}$ and $\Delta\phi(r) < 0$ for $r > R_{\rm cor}$. At corotation, where $\Delta\phi(R_{\rm cor}) = 0$, the two components H I and 24 μm should have no systematic offset. We assume $t_{\rm HI\mapsto 24\,\mu m}$ and $\Omega_{\rm p}$ to be constant for any given galaxy, and that all the spirals are trailing, since the only spiral galaxies known to have a leading pattern are NCG 3786, NGC 5426 and NGC 4622 (Thomasson et al. 1989; Byrd, Freeman, & Buta 2002). By χ^2 fitting the model prediction of Eq. 4.8 to the measured angular offsets $\Delta\phi(r)$ in all radial bins of a galaxy, we derive best fit values for $t_{\rm HI\mapsto 24\,\mu m}$ and $\Omega_{\rm p}$.

[4]Found at URL:
http://zwicky.as.arizona.edu/∼cyp/work/galfit/galfit.html

The $\Delta\phi(r)$ data and the resulting best fits are shown in Figure 4.4, with the resulting best fit values listed in Table 4.2. In Figure 4.4 we plot for all objects the radial profile of the angular offsets $\Delta\phi(r)$. The solid line represents the best fit model proscribed by Eq. 4.8. The square symbols in the plot represent the fitted data points from § 4.4.2; the diamonds are reported for completeness, but excluded from the fit since they are not reliable enough (the CC coefficient is too low, see § 4.4.2). Looking at the ensemble results in Figure 4.4, two points are noteworthy: 1) the geometric offsets are small, typically a few degrees and did need high resolution maps to become detectable; 2) the general radial dependence follows overall the simple prescription of Eq. 4.8 quite well.

4.5.2 $t_{\mathrm{HI}\mapsto 24\,\mu\mathrm{m}}$ and R_{cor}

Because $\Delta\phi(r)$ is consistent with (and follows) the predictions of the simple geometry and kinematics in Eq. 4.8, the procedure adopted here turns out to be an effective method to derive:

- the time lag $t_{\mathrm{HI}\mapsto 24\,\mu\mathrm{m}}$, which should bracket the time scale needed to compress the gas clouds, trigger star formation, and heat the dust;
- the kinematic pattern speed Ω_p of the galaxy spiral pattern and, equivalently, the corotation radius R_{cor}.

We now look at the ensemble properties of the resulting values for $t_{\mathrm{HI}\mapsto 24\,\mu\mathrm{m}}$ and R_{cor}. The scatter of the individually fitted $\Delta\phi$ points is significantly larger than their error bars (as shown in Fig. 4.4), which may be due to the galactic dynamics being more complex than our simple assumptions. For example the pattern speed may not be constant over the entire disk or there may be multiple corotation radii and pattern speeds, as for example found by numerical simulations (Sellwood & Sparke 1988) and observed in external galaxies (Hernández et al. 2005).

Even though a considerable intrinsic scatter characterizes $\Delta\phi(r)$ for most of our sample galaxies, and the error bars of $t_{\mathrm{HI}\mapsto 24\,\mu\mathrm{m}}$ listed in Table 4.2 are typically $> 15\,\%$, the histogram of the characteristic timescales $t_{\mathrm{HI}\mapsto 24\,\mu\mathrm{m}}$ in Figure 4.5 shows overall a relatively small spread for a sample of 14 galaxies of different Hubble types: the timescales $t_{\mathrm{HI}\mapsto 24\,\mu\mathrm{m}}$ occupy a range between 1 and 4 Myr for almost all the objects.

The solid curve in Figure 4.4, representing the prescription of Eq. 4.8, intersects the horizontal axis at the corotation radius R_{cor}, which can be formally derived by inverting Eq. 4.8 at $\Delta\phi = 0$. We report in Table 4.2 the ratio between R_{cor} and the exponential scale length R_s for each object and show this result in Figure 4.6. Comparisons of our pattern speed Ω_p measurements with other methodologies (e.g. Tremaine & Weinberg 1984) are listed in Table 4.2. The differences with our results may arise since the Tremaine-Weinberg method assumes the continuity condition of the tracer, which may break down for the gas as it is easily shocked, it changes state, and it is converted into stars (Hernández et al. 2005; Rand & Wallin 2004), or it can be ob-

scured by dust (Gerssen & Debattista 2007). Comparison of the observed non-axisymmetric motions with hydrodynamical models based on the actual stellar mass distribution (Kranz, Slyz, & Rix 2003) have found a characteristic value of $R_{\rm cor}/R_s \simeq 2.7 \pm 0.4$ for a sample of spirals. We plot this range with dashed vertical lines in Figure 4.4, whereas the solid curve in each panel denotes the actual fit value of $R_{\rm cor}/R_s$ for each object. Figure 4.6 illustrates the remarkable fact that the corotation values found in the present paper, $R_{\rm cor}/R_s \simeq 2.7 \pm 0.2$, agree well with the completely independent estimates that Kranz, Slyz, & Rix (2003) derived by a different approach and for a different sample. Therefore, a generic value for the pattern speed of the dominant spiral feature of $R_{\rm cor}/R_s \simeq 2.7 \pm 0.4$ seems robust.

4.5.3 Comparison with CO Data

If the basic picture outlined in the introduction is correct, then the molecular gas traced by the CO, as an intermediate step in the star formation sequence, should lie in between and have a smaller offset from the H I than the 24 μm does, but in the same direction. To check this qualitatively, we retrieved the BIMA-SONG CO maps (Helfer et al. 2003) for the galaxies NGC 628, NGC 5194, and NGC 3627. For comparison we derived the angular offset between the CO emission and the 24 μm, applying the same method described above for the H I. The results are plotted in Figure 4.7. The scarcity of data points (e.g. NGC 628) and their scatter, which is typically larger than the error bars, make estimates of $t_{\rm CO \mapsto 24\,\mu m}$ and $R_{\rm cor}$ rather uncertain. Therefore, we simply focus on $\Delta\phi_{\rm CO-24}(r)$ vs. $\Delta\phi_{\rm HI-24}(r)$, which is shown in Figure 4.7. This figure shows that the values of $\Delta\phi_{\rm CO-24}$ all lie closer to zero than the values of $\Delta\phi_{\rm HI-24}$.

Hence this check shows that the peak location of the molecular gas is consistent with the evolutionary sequence where the H I represents an earlier phase than the CO. In this picture the H I has a larger spatial separation with respect to the hot dust emission, except at corotation, where the three components are expected to coincide. However it is clear that higher sensitivity CO maps are needed to improve this kind of analysis.

4.5.4 Analysis of Non-Circular Motions

So far we have carried out an analysis that is based on the assumption of circular motions. We quantify here non-circular motions and determine to what extent their presence affects the estimate of the timescales $t_{\rm HI \mapsto 24\,\mu m}$, which scale with $\Delta\phi$. In the classic picture (e.g. R69), the radial velocity of the gas is reversed around the spiral shock, so that the material is at nearly the same galactocentric radius before and after the shock. Gas in galaxies with dynamically important spiral arms does not move on circular orbits, though. Shocks and streaming motions transport gas inwards, and gas orbits undergo strong variations of direction. If a continuity equation for a particular gas phase applies, it implies that in the rest frame of the spiral arm, the change of relative velocity perpendicular to the arm $v_\perp$ is proportional to the arm to pre-arm mass flux

ratio (for a recent illustration in M51 see Shetty et al. 2007, hereafter S07). For example for an orbit passing through an arm with mass density contrast of 10, $v_\perp$ would drop by the same factor, producing a net inward deflection of the orbit. We do note that the gas continuity equation may not actually be valid, since stars may form, or the gas may become molecular or ionized. Non-circular motions could modify the simplified scheme of Fig. 4.2. If the orbit is inward bound near the arm, the path of the material between the H I and the 24 μm arm components is larger than that previously assumed for circular orbits. We reconsider the scheme of Fig. 4.2 for a non-circular orbit in the frame corotating with the spiral pattern as illustrated in Fig. 4.8. There, the material moves not along a line at constant radius r, but along a line proceeding from a larger radius $r+dr$, specifically from the point A (see Fig. 4.8) on the H I arm towards the point B on the 24 μm arm, where the two parallel horizontal lines denote the galactocentric distances $r+dr$ and r. The material departs from A with an angle α inwards (if the material were to proceed instead from an inner radius, then α is directed outwards). If α is large, the measurement of the spatial shift $\overline{A'B} \simeq r\,\Delta\phi'$ in the simple scheme of circular (deprojected) rings no longer represents the actual value of the spatial offset $\overline{AB} \propto \Delta\phi$, but rather is only a lower limit. Consequently, the measurement of the time scale $t_{\mathrm{HI}\mapsto 24\,\mu\mathrm{m}}$ would be underestimated, since $t_{\mathrm{HI}\mapsto 24\,\mu\mathrm{m}} \propto \Delta\phi$ from Eq. 4.8. From the geometry of the triangle ABA' in Fig. 4.8, and since $\overline{A'B} \propto \Delta\phi'$ and $\overline{AB} \propto \Delta\phi$, it can be straightforwardly shown that

$$\Delta\phi(r) = \Delta\phi'(r)\,\frac{\cos\beta}{\cos(\beta+\alpha)}, \tag{4.9}$$

where

$$\tan\alpha = \left.\frac{-v_R}{v'_\phi}\right|_{r+dr}, \tag{4.10}$$

$v_R(r)$ and $v'_\phi(r) = v_\phi - \Omega_p\, r$ are the radial and tangential velocity components of the gas in the arm frame, respectively, and β is the H I arm pitch angle defined by

$$\tan\beta = \left.\frac{d\phi_{\mathrm{arm}}}{dr}\right|_r, \tag{4.11}$$

with $\beta \to 90^\circ$ for a tightly wound spiral. Note that the radial and the azimuthal dependences of v_R and v'_ϕ are anchored with respec to each other at the spiral arms through Eq. 4.11. It follows that if the radial and tangential components of the gas velocity, and the pitch angle of the H I spiral arms are known, the actual value of $\Delta\phi$ can be calculated by applying the correction factor

$$k(r) = \frac{\cos\beta}{cos(\beta+\alpha)} \tag{4.12}$$

to the directly measured quantity $\Delta\phi'$.

We selected a few strong arm spiral galaxies to see how much these effects ultimately affect our prior estimates of $t_{\mathrm{HI}\mapsto 24\,\mu\mathrm{m}}$. Specifically, we adopted the

prescriptions for non-circualr streaming motions analysis from § 3 of S07. We define a narrow region along the H I arms interpolated with a logarithmic spiral (see Fig. 3 and 4 in S07), which turns out to rather well describe the arms over a wide radial range. For the case of NGC 5194 we find a logarithmic slope of 26°, similar to the 21° found by S07. Subsequently, we calculate the velocity components v_R and v_ϕ, as function of radius for a few galaxies from our data set with prominent spiral arms: NGC 5194 (M51), NGC 628, and NGC 6946. Also consistent with Gómez & Cox (2002) and S07, we find in these galaxies that the locations of the spiral arms coincide with a net drop-off of the tangential velocity and negative radial velocity, as illustrated in Fig. 4.9 for the specific case of NGC 5194, indicating that near the arms the orbits bend inwards. We then calculate the correction $k(r)$ at the position of the arms, where we expect the largest variations for v_R and v_ϕ. Even so, except where v'_ϕ approaches zero (which does not necessarily coincide with corotation, but rather where the division in Eq. 4.10 diverges and the approximation breaks down) we find for the three considered galaxies that $k(r)$ hovers around unity for all radii. In particular, for NGC 5194, where $|\alpha| < 20°$, the correction $k(r)$ ranges from 0.7 to 1.2, while for NGC 628 and NGC 6946 $k(r)$ ranges between 0.9 and 1.5 (see Fig. 4.10). After fitting Eq. 4.8 to the corrected offset values, we find that the timescale $t_{\mathrm{HI}\mapsto 24\,\mu\mathrm{m}}$ and the pattern speed Ω_p do not change significantly - the differences are lower than the error bars for the three galaxies. The results of these fits are listed in Table 4.3 and plotted in Fig. 4.10. We also find that the radial displacements

$$dr \simeq r\, \tan[\Delta\phi'(r)]\, k(r)\, \sin[\alpha(r)], \tag{4.13}$$

are typically small compared to the radial steps of $\Delta\phi'$, i.e. $|dr| < 70$ pc for NGC 5194.

In § 4.4.2 we calculated $\Delta\phi'$ through Eq. 4.7, hence not only within the spiral arms, but as intensity-weighted mean across the all azimuthal values. If we were to calculate the angle averaged value $\Delta\phi'$ from the average $\langle v_R \rangle$ and $\langle v_\phi \rangle$ weighted by the product H I × 24 μm - which is the weighting function of the cross-correlation, we find $\alpha \simeq 0$ for all radii and a correction $k(r)$ even closer to unity than over a region limited to the arms. With this approach we obtain $0.95 < k(r) < 1.05$ for NGC 5194.

After estimating the streaming motions in three galaxies from our data set, we find that the correction $k(r)$ that we must apply to the angular offset measurements in the scheme of circular orbits is generally near unity. In conclusion, since non-circular motions do not affect much the offset measurements for the galaxies with the most prominent spiral arms of our data set, namely where we expect indeed the highest deviations from circular orbits. Since $t_{\mathrm{HI}\mapsto 24\,\mu\mathrm{m}} \propto \Delta\phi$, we also expect that the time scales $t_{\mathrm{HI}\mapsto 24\,\mu\mathrm{m}}$ will not vary by more than a factor of 1.5.

4.6 Discussion

By analyzing the angular offsets between H I and 24 μm in the context of a simple kinematic model, we found short timescales, $t_{\mathrm{HI}\mapsto 24\,\mu\mathrm{m}}$, as summarized in the histogram of Figure 4.5 and in Table 4.2. The implied characteristic timescales for almost all sample galaxies lie in the range 1–4 Myr. This result sets an upper limit to the timescale for star formation under these circumstances, since we are observing the time lag between two phases: *a*) the atomic gas phase, which subsequently is compressed into molecular clouds and forms clusters of young, embedded, massive stars, and *b*) the hot dust phase, produced by heating from young stars, whose UV radiation is reprocessed by the dust into the mid-IR, as observed at 24 μm. For the few objects where there are suitable CO data, we checked that this geometric picture also holds for the molecular phase.

4.6.1 Time Scales Derived from Pattern Offsets

Egusa, Sofue, & Nakanishi (2004) used the same angular offset technique to compare CO and Hα emission. They report time scales $t_{\mathrm{CO}\mapsto\mathrm{H}\alpha}$ between 4 and 7 Myr for a small sample of nearby galaxies. The Hα traces a later evolutionary stage than the warm dust emission, which can indicate the presence of a young cluster still enshrouded by dust. Therefore the Hα and the dust emission are expected to be separated by the time needed to remove the dusty envelope, though they are observed to be spatially well correlated (Wong & Blitz 2002; Kennicutt 1998). Prescott et al. (2007) found a strong association between 24 μm sources and optical H II regions in SINGS galaxies. Also infrared sources located on top of older, UV-bright, clusters that do not have Hα emission are rare. Since Prescott et al. (2007) suggest that the break out time from dust clouds is short ($\sim$ 1 Myr), we do not expect a strong offset. Egusa, Sofue, & Nakanishi (2004) derived the angular offset by subjective assessment of the separation of the intensity peaks. They report that this may be a source of systematic errors, since they cannot detect by eye angular phase differences less than a certain threshold, so their results would possibly be an upper limit. Given these considerations, the time scales derived in this paper are likely consistent with the conclusions of Egusa, Sofue, & Nakanishi (2004).

Rots (1975) and Garcia-Burillo, Guelin, & Cernicharo (1993) found time lags of $\sim$ 10 Myr for M81 and M51, respectively. In particular, Rots applied the angular offset method to the dust lanes and Hα. This may be in part problematic since the dust absorption in the optical bands only traces the presence of dust and it is unrelated to the warm dust emission due to star formation onset. Garcia-Burillo et al. measured the spatial separation projected on the sky between CO and Hα and not the azimuthal offset.

Allen (2002) has argued that H I is a photodissociation product of UV shining on molecular gas, so it should be seen between the CO and UV/Hα regions. Allen et al. (1986) observed H I between spiral arm dust lanes and H II regions. However Elmegreen (2007) points out that there is no time delay between dust lanes and star formation: dust lanes may only represent a heavy visual extinction

effect and may not be connected to star formation onset. Our finding that CO is situated between H I and hot dust (i.e. Fig. 4.7) stands in conflict with the predictions of the model proposed by Allen (2002).

Photodissociation of H_2

We argue that illumination effects of UV radiation shining on molecular and dusty regions can not photodissociate molecules in order to produce the observed peaks of H I - which correspond to typical surface densities of several solar masses per pc^2. First, the mean free path of the UV photons is remarkably short - typically $\sim$ 100 pc. The presence of dust, particularly abundant in disk galaxies, is the main source of extinction in particular within spiral arms, where we observe the peak of dust emission. Second, none of the galaxies from our data set presents prominent nuclear activity, whose UV flux could ionize preferentially the inner surfaces of the molecular clouds. Also, we exclude that UV radiation from young stellar concentrations can ionize preferentially one side of the clouds causing H I and CO emissions to lie offset with respect to each other, which we instead interpret as due to an evolutionary sequence. In fact, if the light from young stars effectively produces H I by photodissociation of H_2, then the neutral to molecular gas fraction is espected to increase with star formation rate per unit area, $\Sigma_{\rm SFR}$, as a consequence of the increasing UV radiation flux. Yet, the H I to H_2 ratio decreases with increasing $\Sigma_{\rm SFR}$, as also shown for example in Kennicutt et al. (2007) for the galaxy M51. Moreover, the H I density does not vary much as function of $\Sigma_{\rm SFR}$ (Kennicutt 1998).

4.6.2 Can we rule out Timescales of 10 Myr?

Since the 24 μm emission traces the mass-weighted star formation activity, the time scale $t_{\rm HI\mapsto 24\,\mu m}$ measures the time for star clusters to form from H I gas, but it does not show that all molecular clouds live only $\sim$ 2 Myr. It might show that the bulk of massive stars that form in disks has emerged from molecular clouds that only lived $\sim$ 2 Myr, though there could still be molecular clouds that live an order of magnitude longer. Blitz et al. (2007) estimated that the full molecular cloud life times in the Large Magellanic Cloud are 20–30 Myr. In the Milky Way this time scale is estimated to be a few megayears (e.g. Hartmann, Ballesteros-Paredes, & Bergin 2001), but the examined cloud complexes, such as Taurus and Ophiuchus, have low star formation rate and masses more than an order of magnitude lower than those studied by Blitz et al. (2007). Thus, it remains possible that our results and these previous arguments are all consistent. At high density star formation also occurs at higher rate. Blitz et al. (2007) also find that the time scales for the emergence of the first H II regions traced by Hα in molecular clouds is $t_{\rm HII} \sim 7$ Myr, which does not exclude that $t_{\rm HII} \geq t_{\rm HI\mapsto 24\,\mu m}$, but it could be problematic if the break out time is short, as suggested by Prescott et al. (2007), since the time delay which is required between the onset of star formation (as traced by 24 μm from obscured H II regions) and the emergence of Hα emission would need to be large.

In conclusion, we note that the timescale $t_{\mathrm{HI}\mapsto 24\,\mu\mathrm{m}}$ results from a χ^2 fit to all the data, and it is treated as a global constant individually for each galaxy, so it is not a function of radius. Globally, all the characteristic timescales $t_{\mathrm{HI}\mapsto 24\,\mu\mathrm{m}}$ listed in Table 4.2 are $\leq 4\,\mathrm{Myr}$, except one single case (NGC 925). The error bars are also relatively small: $< 1\,\mathrm{Myr}$ for the majority of the cases. These results clearly exclude characteristic timescales $t_{\mathrm{HI}\mapsto 24\,\mu\mathrm{m}}$ of the order of $\sim 10\,\mathrm{Myr}$, even for the highest value recorded in our data set which is NGC 925.

4.6.3 Theoretical Implications

The short time found here between the peak of H I emission and the peak of emission from young, dust-enshrouded stars has implications for two related theoretical controversies. First is the question of whether molecular clouds are short-lived, dynamically evolving objects (Ballesteros-Paredes, Hartmann, & Vázquez-Semadeni 1999, Hartmann et al. 2001; Elmegreen 2000; Ballesteros-Paredes & Hartmann 2007; Elmegreen 2007) or quasi-static objects evolving over many free-fall times (Matzner 2002; Krumholz, Matzner, & McKee 2006). The second, related question is what the rate-limiting step for star formation in galaxies is: formation of gravitationally unstable regions in the H I that can collapse into molecular clouds (Elmegreen 2002; Kravtsov 2003; Li, Mac Low, & Klessen 2005, Li, Mac Low, & Klessen 2006; Elmegreen 2007); or formation of dense, gravitationally unstable cores within quasi-stable molecular clouds (Krumholz & McKee 2005; Krumholz, Matzner, & McKee 2006; Krumholz & Tan 2007).

The short timescales found here for the bulk of massive star formation in regions of strong gravitational instability appears to support the concept that molecular cloud evolution occurs on a dynamical time once gravitational instability has set in, and that the rate-limiting step for star formation is the assembly of H I gas into gravitationally unstable configurations. Our work does not, however, address the total lifetime of molecular gas in these regions, as we only report the separation between the peaks of the emission distributions. Molecular clouds may well undergo an initial burst of star formation that then disperses fragments of molecular gas that continue star formation at low efficiency for substantial additional time (Elmegreen 2007). Averaging over the efficient and inefficient phases of their evolution might give the overall low average values observed in galaxies (e.g. Krumholz & Tan 2007).

4.7 Conclusion

We have derived characteristic star formation time scales for a set of nearby spiral galaxies, using a simple geometric approach based on the classic Roberts (1969) picture that star formation occurs just downstream from the maximal gas compression induced by a spiral arm. This derived time scale, $t_{\mathrm{HI}\mapsto 24\,\mu\mathrm{m}}$, refers to the processes from the densest H I to the molecular phase to enshrouded hot stars heating the dust. The analysis is based on high resolution 21-cm maps from THINGS, which we combined with 24 μm maps from SINGS. We assume

Figure 4.1: NGC 5194: the 24 μm band image is plotted in color scale; the H I emission map is overlayed with green contours (see also Kennicutt et al. 2007).

that the observed spiral arms have a pattern speed Ω_p. Given the rotation curve, $v_c(r) = r\,\Omega(r)$, this allows us to translate angular offsets at different radii between the H I flux peaks and the 24 μm flux peaks in terms of a characteristic time difference.

At each individual point along the spiral arm we found considerable scatter between the H I and 24 μm emission peaks. However, for each galaxy we could arrive at a global fit, using a cross-correlation technique, and derive two characteristic parameters, $t_{\mathrm{HI}\mapsto 24\,\mu\mathrm{m}}$ and R_{cor}. For our 14 objects we found the general relation $R_{\mathrm{cor}} = (2.7 \pm 0.2)\,R_s$, which is consistent with previous studies (e.g. Kranz, Slyz, & Rix 2003) and, more importantly, we found $t_{\mathrm{HI}\mapsto 24\,\mu\mathrm{m}}$ to range between 1 and 4 Myr. Even when accounting for uncertainties, timescales as long as $t_{\mathrm{HI}\mapsto 24\,\mu\mathrm{m}} \sim 10\,\mathrm{Myr}$, which have been inferred from other approaches, do not appear consistent with our findings. At least for the case of nearby spiral galaxies, our analysis sets an upper limit to the time needed to form massive stars (responsible for heating the dust) by compressing the (atomic) gas. It therefore points to a rapid procession of star formation through the molecular cloud phase in spiral galaxies. If star formation really is as rapid as our estimate of $t_{\mathrm{HI}\mapsto 24\,\mu\mathrm{m}}$ suggests, it must be relatively inefficient to avoid the short term depletion of gas reservoirs.

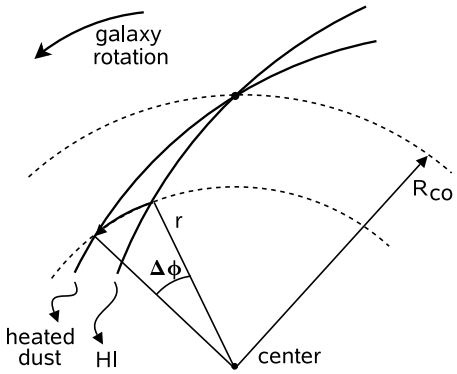

Figure 4.2: Geometry of the scheme adopted to derive the azimuthal phase difference $(\phi_{24\,\mu\mathrm{m}} - \phi_{\mathrm{HI}})(r) \equiv \Delta\phi(r)$ between the H I and the 24 μm emission adopting by convention that ϕ increases in the direction of rotation. Part of a face-on galaxy rotating anti-clockwise is plotted in the panel with the center as indicated. In this plot ϕ increases anti-clockwise. The solid curved lines represent the two components within one spiral arm, namely the H I and the heated dust. The angular separation between the two components is exaggerated for clarity. We measured the deprojected phase difference $\Delta\phi(r)$ at a given radius. Inside corotation, R_{cor}, the material is rotating faster than the pattern speed and the 24 μm emission lies ahead of the H I ($\phi_{\mathrm{HI}} < \phi_{24\,\mu\mathrm{m}}$). At corotation the two patterns coincide, and outside R_{cor} the picture is reversed since the pattern speed exceeds the rotation of the galaxy.

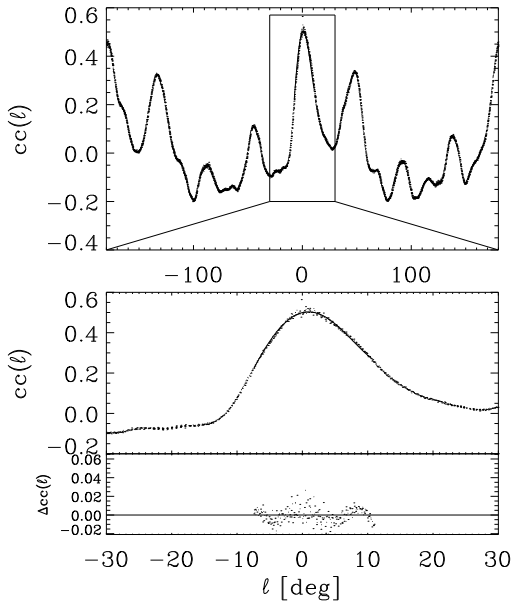

Figure 4.3: Representative example for the determination of the azimuthal offset based on calculating the cross-correlation $cc(\ell)$ of the two functions $f_{\rm HI}(\phi_k, \hat{r})$ and $f_{24\,\mu{\rm m}}(\phi_{k-\ell}, \hat{r})$ as function of azimuth ϕ and at a fixed radius $\hat{r}$. The present example shows the $cc(\ell)$ profile calculated for NGC 628 at $\hat{r} \simeq 2'$ ($\simeq 4.2$ kpc). Top panel: the $cc(\ell)$ profile in the entire range $[-180°, 180°]$; bottom panel: a zoom of the range $[-30°, 30°]$. We considered an adequate range greater than the width of the $cc(\ell)$ profile around $\ell_{\rm max}$ and interpolated $cc(\ell)$ locally ($\pm 10°$ in the example plot) with a fourth-degree polynomial $p_4(\ell) = \sum_{n=0}^{4} a_n\, \ell^n$, and calculated numerically the peak value $\ell_{\rm max}$. The bottom panel shows the fit residuals overplotted around the zero level.

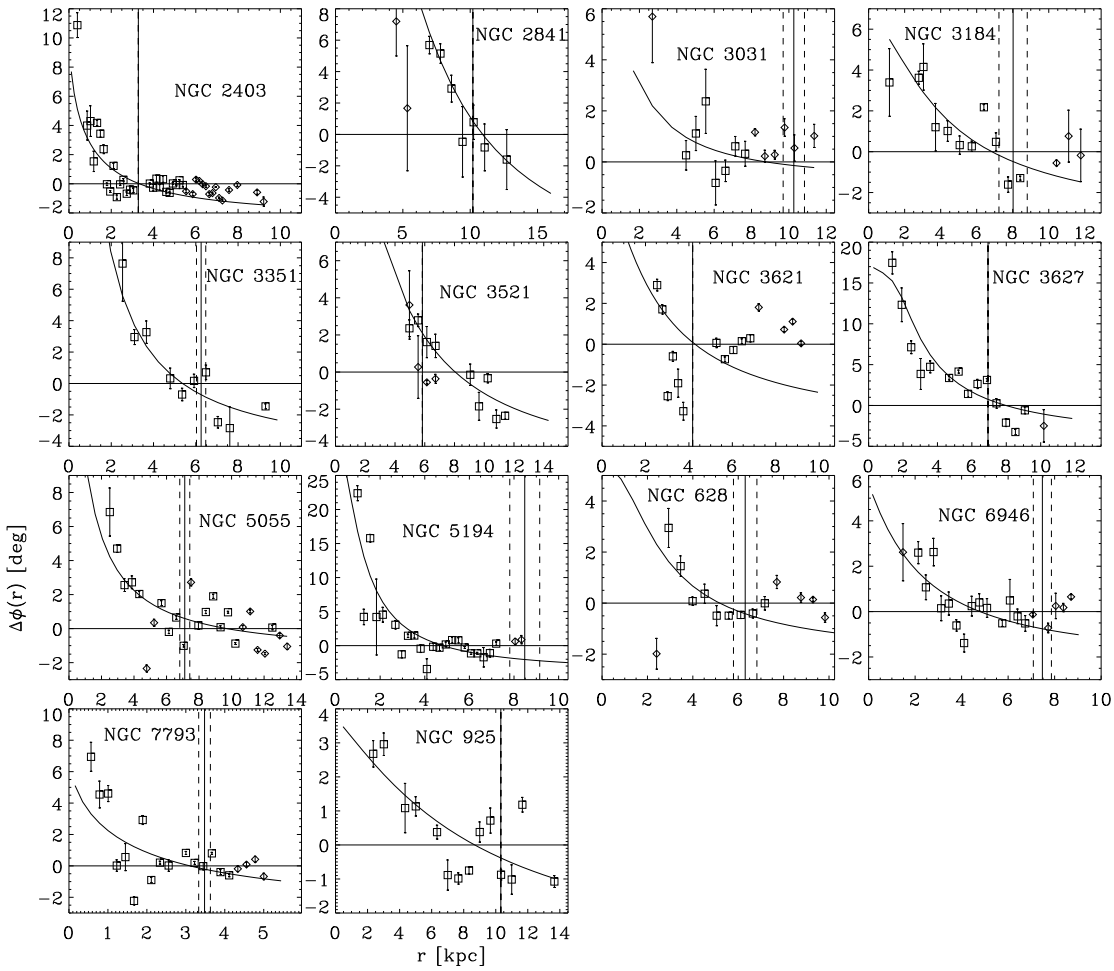

Figure 4.4: Radial profiles for the angular offset H I↦24 μm for the entire sample, obtained by sampling face-on H I and 24 μm maps concentric rings and cross-correlating the azimuthal profiles for each radius. The solid line is the best fit model obtained by χ^2 minimization of Eq. 4.8; the solid curve intersects the horizontal axis at corotation (defined as $\Delta\phi = 0$). The solid and dashed vertical lines indicate the 2.7 $R_s \simeq R_{\rm cor}$ value and error bars, derived by Kranz, Slyz, & Rix (2003). The squares denote points that were included in the fit, the diamonds were excluded from the fit (see text).

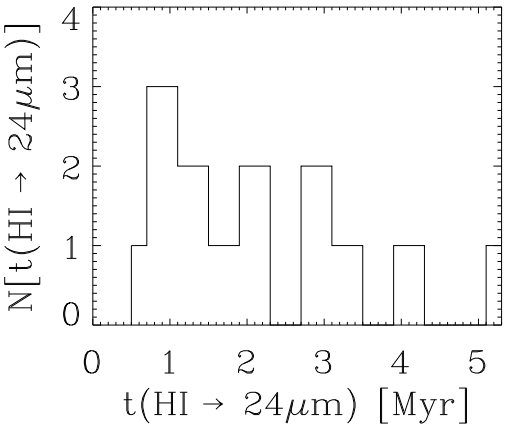

Figure 4.5: Histogram of the time scales $t_{\mathrm{HI}\mapsto 24\,\mu\mathrm{m}}$ derived from the fits in Figure 4.4 and listed in Table. 4.2 for the 14 sample galaxies listed in Table. 4.1. The timescales range between 1 and 4 Myr for almost all galaxies.

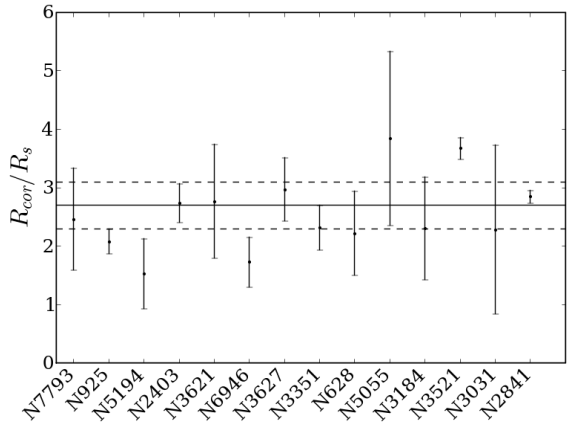

Figure 4.6: The best fit for the spiral arm corotation radius (in units of exponential scale radii) obtained by inverting the best fit model of Eq. 4.1 at $\Delta\phi(r) = 0$, and evaluating R_s via a bulge-disk decomposition on either H band or 3.6 μm band images. The solid and dashed horizontal lines represents the $R_{\mathrm{cor}}/R_s = 2.7 \pm 0.4$ value found by Kranz, Slyz, & Rix (2003). The galaxies in the plot are sorted by asymptotic rotation velocity (see Table 4.1), showing that there is no clear correlation between dynamical mass and R_{cor}/R_s ratio.

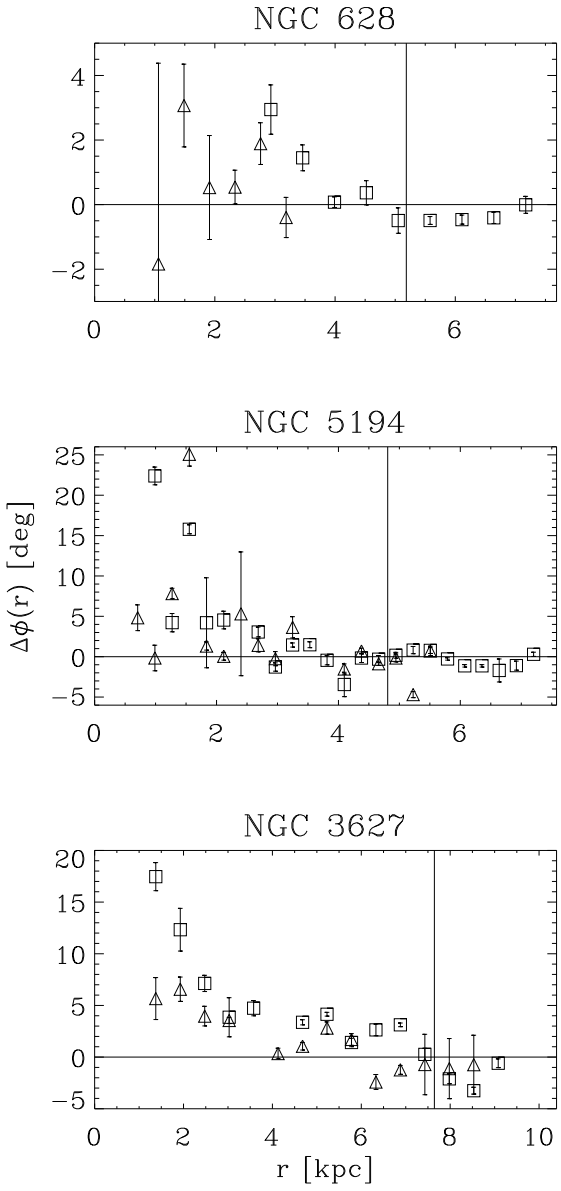

Figure 4.7: Comparison of the angular offsets obtained for H I↦24 μm and CO↦24 μm plotted as squares and triangles, respectively, for the galaxies NGC 628, NGC 5194, and NGC 3627. CO maps are taken from the BIMA-SONG survey. The solid vertical line in each panel indicates the position of corotation as obtained by χ^2 fitting of Eq. 4.1 for the H I.

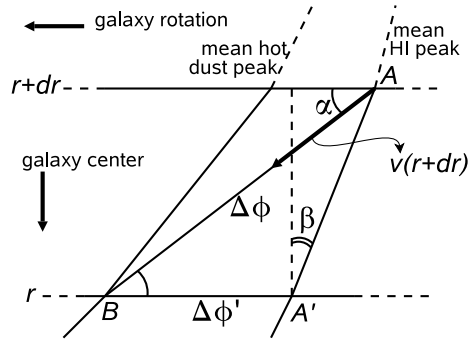

Figure 4.8: Accounting for non-circular motions in the frame corotating with the spiral pattern, the two horizontal lines denoted with r and $r + dr$ represent two galactocentric distances. Gas (and the resulting young stars) move along the line $\overline{AB} \propto \Delta\phi$, proceeding from the mean location of dense H I to the mean 24 μm peak, both denoted with solid lines, where β is the H I pitch angle. The the gas velocity vector is at an angle α with respect to the circle at radius $r+dr$. The line $\overline{A'B}$ denotes the (biased) measure of $\Delta\phi'$ at constant radius r, which we actually estimate in our data analysis, and which is shorter than the actual shift value $\overline{AB} \propto \Delta\phi$ by a factor of $\cos\beta/\cos(\beta + \alpha)$, as explained in the text.

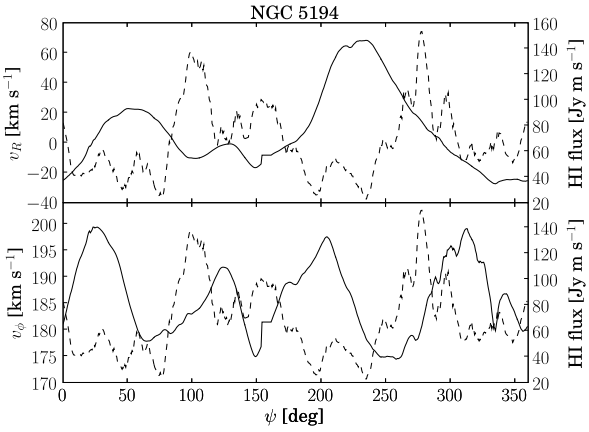

Figure 4.9: Radial and tangential H I velocities, v_R and v_ϕ, as function of azimuth at galactocentric distance of 90" are plotted in the top and bottom panel, respectively, for the galaxy NGC 5194. The dashed line shows the azimuthal profile of the H I flux map at the same radius. Note that the radial veocities are quite small near the H I peaks.

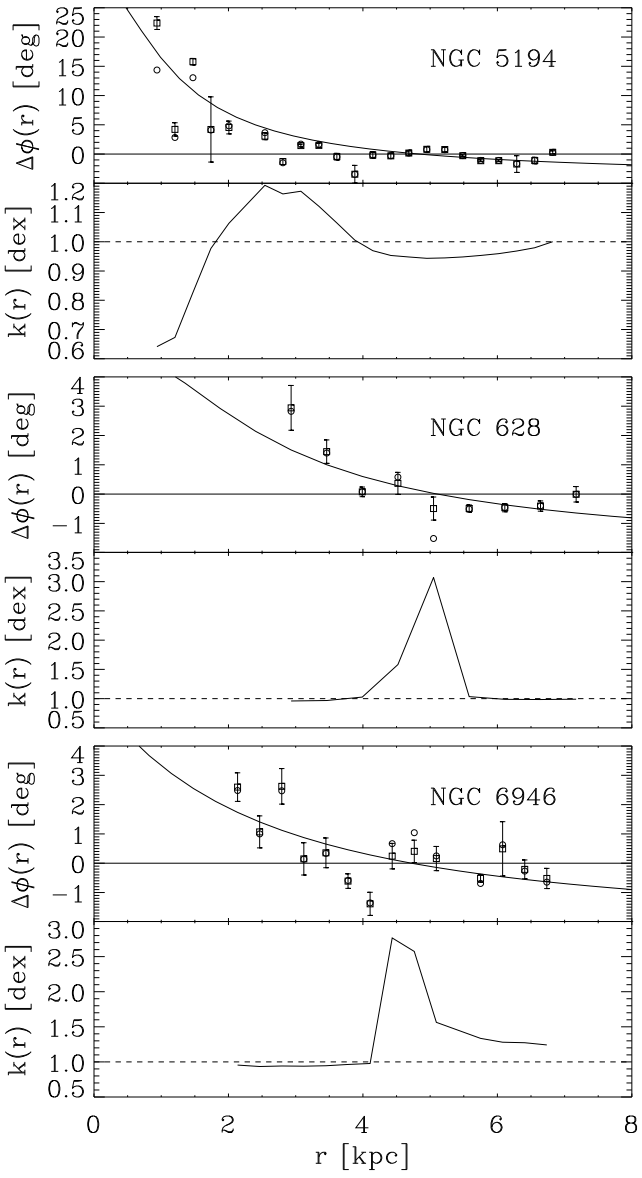

Figure 4.10: Correction factor $k(r)$ from Eq. 4.12, as applied to the angular offset measurement for the galaxies NGC 5194, NGC 628, and NGC 6946. Bottom panels: the solid curve represents the correction factor $k(r) = \cos\beta/\cos(\beta + \alpha)$ as function of radius. Top panels: the squares denote the angular offset measurements $\Delta\phi'$ of Fig. 4.4 calculated assuming circular orbits, the circles denote $\Delta\phi$ after correction, and the solid curve represents the model fit of Eq. 4.8 to the corrected offset values.

Obj. name	Alt. name	R_{25} ($'$) (1)	R_s ($'$) (2)	band (3)	i ($^\circ$) (4)	PA ($^\circ$) (5)	D (Mpc) (6)	v_m (km s^{-1}) (7)
NGC 2403		9.98	1.30*	H	63	124	3.22	128
NGC 2841		3.88	0.92*	3.6	74	153	14.1	328
NGC 3031	M81	10.94	3.63 ± 0.2	3.6	59	330	3.63	253
NGC 3184		3.62	0.92 ± 0.09	H	16	179	11.1	224
NGC 3351		3.54	0.86 ± 0.03	3.6	41	192	9.33	208
NGC 3521		4.8	0.74 ± 0.02	3.6	73	340	10.05	231
NGC 3621		5.24	0.80*	H	65	345	6.64	138
NGC 3627	M66	4.46	0.95*	3.6	62	173	9.25	202
NGC 5055	M63	6.01	1.16 ± 0.05	H	59	102	7.82	209
NGC 5194	M51	4.89	1.39 ± 0.11	H	42	172	7.77	119
NGC 628	M74	4.77	1.10 ± 0.09	H	7	20	7.3	209
NGC 6946		5.35	1.73 ± 0.07	H	32.6	242	5.5	177
NGC 7793		5.0	1.16 ± 0.05	H	50	290	3.82	113
NGC 925		5.23	1.43*	3.6	66	286	9.16	115

Table 4.1: THINGS and SINGS target galaxies. (1): semi-major axis of the 25 mag arcsec^{-2} isophote in the B band obtained from the LEDA database (URL: http://leda.univ-lyon1.fr/); (2): exponential scale length derived in this paper as described in § 4.4 using either IRAF or `galfit` (values tagged with *), where the error bars are $\delta R_s/R_s < 1$ % ; (3): image band used (2MASS H or IRAC 3.6 μm band) to derive R_s; (4) and (5): kinematic inclination and PA, respectively; (6): adopted distance; (7): maximum amplitude of the rotation velocity corrected for inclination. The values in columns (4) to (7) are adopted from de Blok et al. (2008).

Obj. name	Alt. name	$t_{\mathrm{HI}\mapsto 24\,\mu\mathrm{m}}$ [Myr]	Ω_p [km s^{-1} kpc^{-1}]	R_{cor}/R_s	Ω_p [km s^{-1} kpc^{-1}]
NCG 2403		1.4 ± 0.5	30 ± 4	2.8 ± 0.3	
NCG 2841		4.4 ± 0.5	42 ± 2	2.8 ± 0.1	
NGC 3031	M81	0.5 ± 0.3	27 ± 13	2.3 ± 1.4	24^a
NCG 3184		1.8 ± 0.4	38 ± 5	2.3 ± 0.5	
NGC 3351	M95	2.2 ± 0.3	38 ± 3	2.3 ± 0.4	
NGC 3521		2.9 ± 0.4	32 ± 2	3.6 ± 0.2	
NGC 3621		2.3 ± 1.3	31 ± 11	2.8 ± 1.0	
NGC 3627	M66	3.1 ± 0.4	25 ± 4	3.0 ± 0.5	
NCG 5055	M63	1.3 ± 0.3	20 ± 5	3.8 ± 1.5	$30 - 40^b$
NCG 5194	M51	3.4 ± 0.8	21 ± 4	1.5 ± 0.6	38 ± 7^c, 40 ± 8^d
NGC 628	M74	1.5 ± 0.5	26 ± 3	2.2 ± 0.4	
NCG 6946		1.3 ± 0.3	36 ± 4	1.7 ± 0.4	39 ± 9^c, 42 ± 6^d
NGC 7793		1.2 ± 0.5	40 ± 10	2.5 ± 0.9	
NCG 925		5.7 ± 1.6	11 ± 1.0	2.1 ± 0.2	7.7^e

Table 4.2: Characteristic time scales $t_{\mathrm{HI}\mapsto 24\,\mu\mathrm{m}}$ and pattern speed Ω_p resulting from a χ^2 fit of the observed angular offset via Eq. 4.1. The error bars are evaluated via a Monte Carlo method. The timescales $t_{\mathrm{HI}\mapsto 24\,\mu\mathrm{m}}$ listed in this table are summarized in the histogram in Figure 4.5. The corotation radius to exponential scale radius R_{cor}/R_s ratios are summarized in Figure 4.6. We list for comparison in the last column other measurements of the pattern speed: a) Westpfahl (1991); b) Thornley & Mundy (1997); c) Zimmer, Rand, & McGraw (2004); d) Hernández et al. (2004); e) Elmegreen, Wilcots, & Pisano (1998).

Obj. name	Alt. name	$t_{\mathrm{HI}\mapsto 24\,\mu\mathrm{m}}$ [Myr]	Ω_p [km s^{-1} kpc^{-1}]
NGC 5194	M51	3.3 ± 0.6	20 ± 3
NGC 628	M74	1.4 ± 0.5	26 ± 3
NGC 6946		1.1 ± 0.3	36 ± 4

Table 4.3: Characteristic time scales $t_{\mathrm{HI}\mapsto 24\,\mu\mathrm{m}}$ and pattern speed Ω_p resulting from a χ^2 fit to the angular offsets $\Delta\phi$ after correction for non-circular motions following the prescriptions in § 4.5.4. The best fits and the corrections are plotted in Fig. 4.10. In comparison with the values listed in Table 4.2, $t_{\mathrm{HI}\mapsto 24\,\mu\mathrm{m}}$ and Ω_p differ by less than their corresponding error bars.

Bibliography

Allen, R. J. 2002, Seeing Through the Dust: The Detection of HI and the Exploration of the ISM in Galaxies, 276, 288

Allen, R. J., Atherton, P. D., & Tilanus, R. P. J. 1986, Nature, 319, 296

Ballesteros-Paredes, J., Hartmann, L., & Vázquez-Semadeni, E. 1999, ApJ, 527, 285

Ballesteros-Paredes, J., & Hartmann, L. 2007, RevMexA&A, 43, 123

Begeman, K. G. 1989, A&A, 223, 47

Beuther, H., Churchwell, E. B., McKee, C. F., & Tan, J. C. 2007, Protostars and Planets V, 165

Blitz, L., Fukui, Y., Kawamura, A., Leroy, A., Mizuno, N., & Rosolowsky, E. 2007, Protostars and Planets V, 81

Byrd, G., Freeman, T., & Buta, R. 2002, BAAS, 34, 1116

Calzetti, D., et al. 2005, ApJ, 633, 871

Calzetti, D., et al. 2007, ApJ, 666, 870

Cappellari, M., & Copin, Y. 2003, MNRAS, 342, 345

Dale, D. A., et al. 2005, ApJ, 633, 857

de Blok, W.J.G, et al. 2008, AJ, submitted

Dwek, E. 2005, AIP Conf. Proc. 761: The Spectral Energy Distributions of Gas-Rich Galaxies: Confronting Models with Data, 761, 103

Egusa, F., Sofue, Y., & Nakanishi, H. 2004, PASJ, 56, L45

Elmegreen, B. G. 2007, ApJ, 668, 1064

Elmegreen, B. G. 2000, ApJ, 530, 277

Elmegreen, B. G. 2002, ApJ, 577, 206

Elmegreen, B. G., & Elmegreen, D. M. 1986, ApJ, 311, 554

Elmegreen, B. G. , Wilcots, E., & Pisano, D. J. 1998, ApJL, 494, L37

Garcia-Burillo, S., Guelin, M., & Cernicharo, J. 1993, A&A, 274, 123

Gerssen, J., & Debattista, V. P. 2007, MNRAS, 378, 189

Glover, S. C. O., & Mac Low, M.-M. 2007, ApJ, 659, 1317

Goldsmith, P. F., & Li, D. 2005, ApJ, 622, 938

Goldsmith, P. F., Li, D., & Krčo, M. 2007, ApJ, 654, 273

Gómez, G. C., & Cox, D. P. 2002, ApJ, 580, 235

Hartmann, L. 2003, ApJ, 585, 398

Hartmann, L., Ballesteros-Paredes, J., & Bergin, E. A. 2001, ApJ, 562, 852

Helfer, T. T., Thornley, M. D., Regan, M. W., Wong, T., Sheth, K., Vogel, S. N., Blitz, L., & Bock, D. C.-J. 2003, ApJS, 145, 259

Hernández, O., Carignan, C., Amram, P., & Daigle, O. 2004, Penetrating Bars Through Masks of Cosmic Dust, 319, 781

Hernández, O., Wozniak, H., Carignan, C., Amram, P., Chemin, L., & Daigle, O. 2005, ApJ, 632, 253

Hillenbrand, L. A., Massey, P., Strom, S. E., & Merrill, K. M. 1993, AJ, 106, 1906

Hollenbach, D., & Salpeter, E. E. 1971, ApJ, 163, 155

Jarrett, T. H., Chester, T., Cutri, R., Schneider, S. E., & Huchra, J. P. 2003, AJ, 125, 525

Jedrzejewski, R. I. 1987, MNRAS, 226, 747

Jura, M. 1975, ApJ, 197, 575

Kennicutt, R. C., Jr. 1998, ApJ, 498, 541

Kennicutt, R. C., Jr., et al. 2003, PASP, 115, 928

Kennicutt, R. C., Jr., et al. 2007, ApJ, accepted, (astro-ph/0708.0922)

Kim, W.-T., & Ostriker, E. C. 2002, ApJ, 570, 132

Kim, W.-T., & Ostriker, E. C. 2006, ApJ, 646, 213

Kranz, T., Slyz, A., & Rix, H.-W. 2003, ApJ, 586, 143

Kravtsov, A. V. 2003, ApJL, 590, L1

Krumholz, M. R., Matzner, C. D., & McKee, C. F. 2006, ApJ, 653, 361

Krumholz, M. R., & McKee, C. F. 2005, ApJ, 630, 250

Krumholz, M. R., & Tan, J. C. 2007, ApJ, 654, 304

Li, Y., Mac Low, M.-M., & Klessen, R. S. 2005, ApJL, 620, L19

Li, Y., Mac Low, M.-M., & Klessen, R. S. 2006, ApJ, 639, 879

Lin, C. C., & Shu, F. H. 1964, ApJ, 140, 646

Martin, C. L., & Kennicutt, R. C., Jr. 2001, ApJ, 555, 301

Matzner, C. D. 2002, ApJ, 566, 302

Mouschovias, T. C., Tassis, K., & Kunz, M. W. 2006, ApJ, 646, 1043

Palla, F., & Stahler, S. W. 1999, ApJ, 525, 772

Palla, F., & Stahler, S. W. 2000, ApJ, 540, 255

Peng, C. Y., Ho, L. C., Impey, C. D., & Rix, H.-W. 2002, AJ, 124, 266

Popescu, C. C., Tuffs, R. J., Völk, H. J., Pierini, D., & Madore, B. F. 2002, ApJ, 567, 221

Prescott, M. K. M., et al. 2007, ApJ, 668, 182

Rand, R. J., & Kulkarni, S. R. 1990, ApJL, 349, L43

Rand, R. J., & Wallin, J. F. 2004, ApJ, 614, 142

Rafikov, R. R. 2001, MNRAS, 323, 445

Rix, H.-W., Guhathakurta, P., Colless, M., & Ing, K. 1997, MNRAS, 285, 779

Rix, H.-W., & Zaritsky, D. 1995, ApJ, 447, 82

Roberts, W. W. 1969, ApJ, 158, 123

Rots, A. H. 1975, A&A, 45, 43

Scoville, N. Z., Polletta, M., Ewald, S., Stolovy, S. R., Thompson, R., & Rieke, M. 2001, AJ, 122, 3017

Sellwood, J. A., & Sparke, L. S. 1988, MNRAS, 231, 25P

Shetty, ., Vogel, S. N., Ostriker, E. C., & Teuben, P. J. 2007, ApJ, 665, 1138

Smith, J. D. T., et al. 2007, ApJ, 656, 770

Tan, J. C., Krumholz, M. R., & McKee, C. F. 2006, ApJL, 641, L121

Tassis, K., & Mouschovias, T. C. 2004, ApJ, 616, 283

Thomasson, M., Donner, K. J., Sundelius, B., Byrd, G. G., Huang, T. Y., & Valtonen, M. J. 1989, Ap&SS, 156, 205

Thornley, M. D. , & Mundy, L. G. 1997, ApJ, 484, 202

Thronson, H. A., Jr., & Telesco, C. M. 1986, ApJ, 311, 98

Toomre, A. 1964, ApJ, 139, 1217

Trachternach, C., et al. 2008, AJ, submitted

Tremaine, S., & Weinberg, M. D. 1984, ApJL, 282, L5

Vázquez-Semadeni, E., Kim, J., Shadmehri, M., & Ballesteros-Paredes, J. 2005, ApJ, 618, 344

Vogel, S. N., Kulkarni, S. R., & Scoville, N. Z. 1988, Nature, 334, 402

Walter, F., et al. 2008, AJ, submitted

Westpfahl, D. 1991, The Interpretation of Modern Synthesis Observations of Spiral Galaxies, ASPC, 18, 175

Williams, D. A. 2005, JPhCS, 6, 1

Wong, T., & Blitz, L. 2002, ApJ, 569, 157

Zimmer, P., Rand, R . J., & McGraw, J. T. 2004, ApJ, 607, 285

Chapter 5

Turbulence and Star Formation in Nearby Galaxies

Abstract

We investigate the interplay between turbulence in the atomic neutral (H I) gas and the star formation rate on local scales in a sample of nearby spiral and dwarf galaxies. In particular, we inquiry at what level the star formation activity is able (e.g. via supernovae explosions, winds, etc.) to inject energy into the interstellar medium that results in turbulent gas motions. To clarify this issue, we carry out a comparative study using maps of H I surface density mass, H I velocity dispersion, and surface density of star formation rate (SFR) obtained from THINGS and SINGS. We find that the sample galaxies exhibit a radial systematic decline of H I velocity dispersion, and a common value of velocity dispersion, 10 ± 1 km s^{-1}, at a galactocentric distance of r_{25}. Finally, we find that velocity dispersion and SFR are correlated for all the galaxies of our data sample. Drawing our first attempt of interpretation of the results, we propose that the star formation feedback could be driving a substantial portion of the observed H I velocity dispersion.

5.1 Introduction

Turbulence in the ISM plays a dual role, maintaining a pressure support on global scales, thus preventing star formation, and inducing collapse locally, promoting star formation (see, for extensive and detailed reviews, Mac Low & Klessen 2004; Elmegreen & Scalo 2004; McKee & Ostriker 2007).

Supersonic Turbulence

Molecular clouds are characterized by supersonic gas motions, which balance gravity on scales larger than 0.1 pc, therefore, inhibiting the global collapse (Williams, Blitz, & McKee 2000; Heitsch, Mac Low, & Klessen 2001; Ostriker, Stone, & Gammie 2001). While supersonic turbulence maintains apparent stability in molecular clouds against collapse on global scales, locally, it will establish a complex network of interacting shocks, which can grow supercritical, and ultimately collapse (Klessen, Heitsch, & Mac Low 2000). If the stochastic density fluctuations due to turbulent gas collisions within molecular clouds are sufficiently strong, low mass and self-gravitating dense cores can collapse and induce the formation of stars (Hunter et al. 1986; Bonazzola et al. 1987; Elmegreen 1993; Ballesteros-Paredes, Hartmann, & Vázquez-Semadeni 1999). However, if supersonic turbulence provides enough kinetic energy to disperse the density fluctuations on timescales shorter than their free-fall time, the local collapse of these clouds generated by random motions can be entirely arrested (Klessen et al. 2000; Elmegreen 2002).

Rapid Decay

Extensive efforts on numerical simulations have demonstrated that both hydrodynamical and magneto-hydrodynamical (MHD) supersonic turbulence decay over a relatively short time scale, comparable to the free-fall time (Mac Low et al. 1998; Stone, Ostriker, & Gammie 1998; Mac Low 1999; Padoan & Nordlund 1999; Avila-Reese & Vázquez-Semadeni 2001; Ostriker, Stone, & Gammie 2001), and that turbulence extends on a wide range of scales (Elmegreen, Kim, & Staveley-Smith 2001; Elmegreen, Elmegreen, & Leitner 2003). Consequently, supersonic turbulence requires a driving mechanism that continuously provides energy to the medium and maintains the turbulent regime (Gammie & Ostriker 1996; Mac Low 1999).

Sources of Continuous Turbulence Driving

To establish which of the available sources is or are driving the turbulence in the ISM is still matter of debate. The idea that star formation processes may drive the turbulence was first envisioned by Spitzer (1978). Star formation itself, injects energy back to the ISM through stellar winds of O-B type and Wolf-Rayet stars, and UV ionizing radiation. Turbulent motions might be attributed to supernova explosions (e.g. Kim, Balsara, & Mac Low 2001; Dib, Bell, & Burkert 2006; Joung & Mac Low 2006), whose influence is possibly more effective than other stellar sources (Mac Low & Klessen 2004; Kornreich & Scalo 2000). The same converging flows in the ISM, that induce the molecular clouds formation, might also generate turbulence (Elmegreen 1993; Ballesteros-Paredes, Hartmann, & Vázquez-Semadeni 1999).

Galactic rotation also contributes to the pressure disturbance through spiral wave shocks (Roberts 1969), rotational shear (Fleck 1981; Schaye 2004), swing amplified shear instabilities (Huber & Pfenniger 2001; Wada, Meurer, & Norman

2002), and gravitational potential energy of the arms (Elmegreen et al. 2003). In addition, large-scale disk instabilities are also considered to maintain the turbulent regime, e.g. magneto-rotational instability (Balbus & Hawley 1991; Sellwood & Balbus 1999; Dziourkevitch et al. 2004; Piontek & Ostriker 2005), MHD instabilities that occur within spiral shocks (Wada & Koda 2004; Kim & Ostriker 2006; Kim, Kim, & Ostriker 2006), galactic rotation coupled with self-gravity (Wada et al. 2002), thermal instability (Dib & Burkert 2005), and non linear development of gravitational instability (Li, Mac Low, & Klessen 2005, 2006). However, numerical work on MHD turbulence suggests that magnetic fields are not the most important source of energy injection (Passot & Vázquez-Semadeni 2003; Cho & Lazarian 2003; Heitsch et al. 2001; Ostriker et al. 2001).

Local Disk Stability

For a galactic disk in pressure equilibrium, the disk stability (Toomre 1964; Goldreich & Lynden-Bell 1965) is also set by the degree of turbulence as traced by the velocity dispersion. Several studies previously assumed the gas velocity dispersion as a constant parameter, and the onset of gravitational instability were basically set by a critical density value (Spitzer 1968; Quirk 1972; Kennicutt 1989, 1998; Martin & Kennicutt 2001; Hunter et al. 1998; Schaye 2004), which in principle could also explain the low SFR regime in low surface brightness galaxies (van der Hulst et al. 1993) and dwarf galaxies (van Zee et al. 1997). Yet, the velocity dispersion may considerably vary radially and azimuthally in disks (Wong & Blitz 2002), allowing for local instabilities and possibly inducing star formation.

Turbulence in the atomic gas

The two phases, atomic and molecular, coexist at two different regimes of turbulence, characterized by kinetic temperatures which hover around $\sim 10 - 100$ K for the (cold) molecular gas and $\sim 5\,10^3 - 10^4$ K for (warm) neutral atomic gas, suggesting that the ISM is composed by an extended component of H I and a very concentrated molecular component with a low filling factor. In fact, almost all the mass of interstellar molecular gas is concentrated in molecular clouds, which lie enclosed by an envelop of atomic gas (Wannier et al. 1991; Blitz 1993; Williams, Blitz, & Stark 1995). The compression of H I gas and the subsequent collapse through instabilities leads to the formation of molecular clouds (Blitz & Shu 1980; Rafikov 2001; Li et al. 2005; Blitz et al. 2007). While the molecular to atomic gas fraction varies as function of the galactocentric radius, with a predominance of molecular towards the center (Wong & Blitz 2002), the SFR is determined by the total (H I + H_2) gas mass, and only weakly by the H I mass (Kennicutt 1989; Kennicutt et al. 2007). However, if the turbulence is sufficiently high to prevent the collapse of clouds, galaxies could show little or no star formation even displaying substantial (H I) gas mass (Mac Low & Klessen 2004). On the contrary, if turbulence and random motions facilitate the cloud assembling, and consequently the star formation (Klessen et al. 2000), then the

gas velocity dispersion is expected to correlate with the SFR. According to the originary idea of Spitzer (1978), who envisioned that stellar processes (e.g. SNe, winds, radiation) might drive the turbulence in the ISM, the velocity dispersion must correlate with SN rate – as traced by SFR.

The H I disk of galaxies, which can be observed at high signal-to-noise over an extent of several tens of kiloparsecs, may provide a testbed for these statements. Observations have proven that, even beyond r_{25} (the radius where the B band surface brightness equals 25 mag arcsec^{-2}), where the SFR and consequently the SN rate are low, the H I velocity dispersion is significantly maintained at a constant regime between $\sim$ 6 km s^{-1} (Dickey, Hanson, & Helou 1990; Kamphuis 1993; Rownd, Dickey, & Helou 1994; Petric & Rupen 2001) and 10 km s^{-1} (van Zee & Bryant 1999; van der Kruit & Shostak 1982), or, in some observational cases, with a systematic decrease of the velocity dispersion with radius down to 6-8 km s^{-1} (Boulanger & Viallefond 1992; Petric & Rupen 2007).

Using high quality maps – in terms of spatial and spectral resolution, sensitivity, and wide field coverage – provided by the surveys THINGS and SINGS (§ 5.2), we study an heterogeneous sample nearby spiral and dwarf galaxies, mapped in emissions of the 21-cm wavelength, infra-red heated dust, and UV. We focus for our sample galaxies on the interplay between SFR and turbulent motions in the H I (§ 5.3), with particular regard to pixel-by-pixel relations and radial dependencies (§ 5.4). Finally, with the observed relations in hand, we attempt to interpret what mechanism is possibly driving turbulence in the ISM consistently with the star formation laws (§ 5.5).

5.2 The Data

In this chapter we carry out a localized comparison of the H I density and kinematics (especially the velocity dispersion) and SFR surface density in nearby spiral galaxies. We make use of The H I Nearby Galaxy Survey (THINGS; Walter et al. 2008) to obtain integrated column density and velocity dispersion maps of neutral hydrogen 21-cm emission line. In order to compare with SFR maps, we then combine the H I data with MIPS 24 μm emission maps, taken from the Spitzer Nearby Galaxies Survey (SINGS; Kennicutt et al. 2003), and far-UV (FUV) emission maps, taken from the Galaxy Evolution Explorer (GALEX; Gil de Paz et al. 2007), for a set of disk galaxies in common with the THINGS sample. To avoid that the velocity dispersion maps are affected by line of sight effects, we retain only those sample galaxies that are more face-on than $\sim 50^\circ$ (see e.g. Leroy et al. 2008), leaving 11 disk galaxies in total, including three dwarf galaxies, listed in Table 5.1.

In addition, we present a qualitative analysis for three galaxies of the THINGS sample observed by VLT/VIMOS with Integral Field Unit (IFU) spectroscopy, in order to probe the central star forming regions as traced by the ionized gas emission lines. The sample of galaxies observed with VIMOS is summarized in Table 5.2.

5.2.1 THINGS

The THINGS project, carried out with the NRAO[1] Very Large Array, aims at mapping 34 nearby galaxies in the 21-cm emission line, which is a tracer of the neutral atomic gas. These maps are characterized by an angular resolution of $\sim 7''$, and a velocity resolution of ~ 5 km s^{-1}, and have a $5\,\sigma$ sensitivity to a column density of $N(\mathrm{HI}) \geq 8 \times 10^9$ cm^{-2} per channel. The maps provide a large spatial coverage, encompassing the entire H I disk of almost all sample galaxies.

5.2.2 SINGS

A large fraction of the targets observed by THINGS overlap with the SINGS dataset, which mapped these galaxies from the far- and near-IR to the optical and UV wavelength bands. In particular, we make use of the MIPS 24 μm band images (Rieke et al. 2004), whose reduction is described by Gordon et al. (2005). The MIPS instrument has a resolution of $\simeq 6''$ at 24 μm, and a wide extent, which tipically covers $\sim 2\,r_{25}$. The FUV maps are taken with the GALEX satellite. These images have a resolution (FWHM) of $5.6''$ within the $\lambda = 1350 - 1750$ Å band and have a field of view of $\sim 1.25°$.

The 24 μm band emission indicates the re-processed radiation from hot dust heated by the UV light from young massive stars and, therefore, it also represent the optimal tracer of dust-enshrouded, ongoing star formation over a time scale $3 - 10$ Myr (Calzetti et al. 2005; Pérez-González et al. 2006; Tamburro et al. 2008), while the FUV emission complements the 24 μm emission in the regions poor in dust content, probing therefore low-metallicity and older regions of star formation over timescales of $\tau \sim 10 - 100$ Myr (Calzetti et al. 2005; Salim et al. 2007). Regions of low SFR and metallicity are characteristic of dwarf galaxies and of outermost regions of spiral galaxies. To estimate the SFR surface density maps, Σ_{SFR}, we use a combination of the MIPS 24 μm and the GALEX FUV maps following the method illustrated by Calzetti et al. (2007) and the discussion by Leroy et al. (2008):

$$\frac{\Sigma_{\mathrm{SFR}}}{[\mathrm{M_\odot yr^{-1} pc^{-2}}]} = \frac{3.6 \times 10^{-3}\, I_{24}}{[\mathrm{MJy\,sr^{-1}}]} + \frac{8.1 \times 10^{-2}\, I_{\mathrm{FUV}}}{[\mathrm{MJy\,sr^{-1}}]} \tag{5.1}$$

where further processing applied to the GALEX FUV and SFR maps, e.g. background subtraction and flagging of foreground field stars, is described by Bigiel et al. (2008).

5.2.3 Ionized Gas

The observations[2] of the central regions of three galaxies of the THINGS sample have been carried out in service mode at the Paranal Observatory using the

[1] The National Radio Astronomy Observatory is a facility of the National Science Foundation operated under cooperatice agreement by Associated Universities, Inc.

[2] Based on observations carried out at the European Southern Observatory (ESO 76.B-0756)

VIMOS instrument at the 8 m VLT. Among the galaxies of the VIMOS sample, only NGC 7793 overlaps with our primary sample of 11 galaxies.

The IFU mode of the VIMOS spectrograph, packed with a matrix of 40×40 lenslets + fibers covering a total field of view of $27'' \times 27''$, provides a set of 40×40 spectra with a spatial sampling of $0.66''$ each. The HR_red grism is characterized by a spectral resolution of $R \sim 2500$, which corresponds to a FWHM $\sim$ 65 km s^{-1}, and by wavelength coverage from $\sim \lambda$6300 Å to $\sim \lambda$8600 Å, which enables to target the spectral emission lines of Hα, [N II] $\lambda\lambda$6548.0, 6583.4 Å, and [S II] $\lambda\lambda$6716.4, 6730.8 Å in order to measure the kinematics of the ionized gas in the central regions. The observations consist in one 30 min exposure per target.

The data cubes are provided after basic processing of the raw data, wavelength calibration and spectra extraction, which are supported for service mode runs since period 73 by the Quality Control Garching at the ESO Headquarters. We further improve the wavelength calibration using a set of ~ 80 bright emission lines of the night sky (Osterbrock, Fulbright, & Bida 1997), from which we also estimate the instrumental width.

5.3 Analysis

We start the analysis from fully reduced H I data cubes for our sample of 11 galaxies, where the reduction steps of the raw data is described in Walter et al. (2008). In order to determine the moments maps relevant for our immediate goal, in particular the mass surface density $\Sigma_{\rm HI}$ and the velocity dispersion σ of the H I gas, we adopt two independent approaches, as we will explain in § 5.3.1: for every (x, y)-pixel location of the signal in the data cubes we perform (1) a direct numerical integration, and (2) a functional χ^2-fit.

Furthermore, we quantitatively test correlations among the three variables $\Sigma_{\rm HI}$, σ, and $\Sigma_{\rm SFR}$, for each galaxy of our sample. The analysis is carried out pixel-by-pixel and in radial bins. Ultimately, we present a qualitative analysis of the velocity dispersion on small (sub-kpc) scales for both the H I and the ionized gas.

5.3.1 Determination of the H I Moment Maps

The zero-th moment map is calculated by integrating the H I data cube along the velocity dimension for a total number N of velocity channels using:

$$\mu_0 = \sum_{i=1}^{N} S_i, \tag{5.2}$$

where S_i denotes the signal within the i-th velocity channel. For each sample galaxy, the spectral dimension of the H I data cubes is sufficiently broad to encompass all the corresponding velocity values. The first moment map, which

corresponds to the velocity field along the line of sight, is given by the intensity-weighted mean velocity:

$$\mu_1 = \frac{1}{\mu_0} \sum_{i=1}^{N} v_i \, S_i, \tag{5.3}$$

where v_i is the velocity value of the i-th channel, and the term $1/\mu_0$ expresses the normalization to the total signal. The variance, that corresponds to the square of the velocity dispersion, is given by the intensity-weighted mean deviation:

$$\sigma^2 = \frac{1}{\mu_0} \sum_{i=1}^{N} (v_i - \mu_1)^2 \, S_i. \tag{5.4}$$

By calculating these integrals over the data cubes for all the positions on the sky $S_i(x, y)$ and $v_i(x, y)$, we obtain the pixel-by-pixel maps of $\mu_0(x, y)$, $\mu_1(x, y)$, and $\sigma(x, y)$.

The H I emission lines can also be described through the functional parameterization of a Gaussian which best represents, in a χ^2 sense, the observed line profile. We adopt a Gaussian function with

$$g(v) = a_0 \exp\left(-\frac{v - v_0}{2\sigma^2}\right), \tag{5.5}$$

where a_0 is the peak amplitude of the Gaussian, v_0 is the central position, and σ is the width. Here, the Gaussian parameters can be interpreted as follows: $A_0 = \sqrt{2\pi}\, a_0$ corresponds to the formal integrated flux, v_0 represents the mean velocity, and σ the velocity dispersion. We recall that the data cubes are continuum subtracted, therefore the parameterization of Eq. 5.5 does not include an additive constant. By performing χ^2-fit of this Gaussian function to the observed emission lines within the data cubes for every sky positions (x, y) independently, we obtain the pixel-by-pixel maps of $A_0(x, y)$, $v_0(x, y)$, and $\sigma(x, y)$. The difference between deriving the H I mass surface density $\Sigma_{\rm HI}$ and the velocity dispersion σ by numeric integration and by functional fit will be discussed in § 5.4.1. Afterwards, all the surface density maps, obtained by direct integration and Gaussian fitting are corrected by inclination, whose adopted values are listed in Table 5.1.

Maximum Rotation Velocity – $v_{\rm max}$

From the velocity map as traced by the 1-st moment map in Eq. 5.3 we calculate the peak rotational velocity for each galaxy of our sample. We sample the velocity map in tilted rings (e.g. Begeman 1989) fitting to the observed velocity $v(\psi|r)$ the parameterization

$$v(\psi|r) = v_{\rm sys} + v_c(r) \, \sin i \cos\psi \tag{5.6}$$

as a function of azimuth ψ, where $\psi = 0$ denotes the kinematic position angle of the receding side of the galaxy, and the systemic velocity $v_{\rm sys}$, the inclination

i and the position angle are adopted from Table 5.1. Then, we determine the maximum value $v_{\rm max}$ of the deprojected velocity curve $v_c(r)$ parameterized with with a smooth functional form (cf. Rix et al. 1997):

$$v_c(r) = v_0 \left(1 + \frac{r}{r_0}\right)^{\beta} \left[1 + \left(\frac{r_0}{r}\right)^{\gamma}\right]^{-1/\gamma} \tag{5.7}$$

where r_0 and v_0 represent the scale parameters of radius and velocity, respectively, and β and γ denote the scaling slopes.

5.3.2 Are $\Sigma_{\rm HI}$, σ, and $\Sigma_{\rm SFR}$ Correlated?

Having determined the H I maps in § 5.3.1, through numerical integration and Gaussian fit, we consider the relations among the three variables $\Sigma_{\rm HI}$, σ, and $\Sigma_{\rm SFR}$ (1) in a pixel-by-pixel scatter plot (Figs. 5.3, 5.4, and 5.5), and (2) radial samples of tilted concentric rings (Figs. 5.7, 5.8, and 5.9). Since the pixel of our maps have a size of $1.5''$, note that the size of each sampling point is ~ 4 times smaller than the actual resolution of the H I maps.

Pixel-by-Pixel Relations

As we will discuss in § 5.4.1, we find correlation for σ vs $\Sigma_{\rm HI}$, $\Sigma_{\rm SFR}$ vs σ, and $\Sigma_{\rm SFR}$ vs $\Sigma_{\rm HI}$, for the galaxies of our dataset (Figs. 5.3, 5.4, and 5.5). Therefore, we assess the degree of correlation among these quantities using a simple linear fit in a log-log plane. We perform the linear fit through linear regression using the method of the orthogonal distance minimization following Isobe et al. (1990). Differently from the ordinary linear regression OLR($Y|X$) between an independent variable X and a dependent variable Y, and the inverse OLR($X|Y$), where X instead depends on the independent variable Y, the method of orthogonal regression does not depend on the assumption on how X and Y depend on each other. From these fits we obtain the slope indices and the zero-points of the power-law relations. Note that since the number of data points is remarkably large (several $\sim 10^4$), the formal error bars of the linear regression result very small.

Radial Relations

We will show in §§ 5.4.2 and 5.4.3 that the H I column density, the H I velocity dispersion and the SFR generally decrease with the distance r to the galaxy center. We test the validity and the radial dependence of the pixel-by-pixel relations for $\Sigma_{\rm HI}$, σ, and $\Sigma_{\rm SFR}$ within radial bins, in order to isolate r as a possible driver of correlations between $\Sigma_{\rm HI}$, σ, and $\Sigma_{\rm SFR}$ within an annulus of given r. First, we sample our maps with tilted rings using radial bins of $\sim 15''$ of width, and calculate the average value of the velocity dispersion for each bin. For all the galaxies of our data set we observe a systematic constant decrease of the velocity dispersion as a function of galactocentric radius. In a few cases the velocity dispersion mildly diverges towards the center, typically at $\sim 0.5\, r_{25}$.

Subsequently, we perform a linear fit to the radial profiles of σ for all $r \geq 0.5\, r_{25}$, specifically where $\sigma(r)$ is approximately linear with r for all the galaxies of the sample. Ultimately, we sample our maps with tilted rings using a radial width of $\sim 1'$, and for each radial bin we calculate the corresponding average values of $\Sigma_{\rm HI}$, σ, and $\Sigma_{\rm SFR}$, in a log-log plane similarly to the previous procedure adopted for the analysis of the pixel-by-pixel relations.

5.3.3 Analysis of the Ionized Gas

In contrast to the global trend that we will describe in § 5.4.1, regions smaller than a few hundred parsec evidence an inversion of the correlations involving the velocity dispersion, as we will qualitatively show in § 5.4.2, in particular, displaying an apparent regime of anti-correlation with the gas surface density. Remarkably, both the H I and the ionized gas exhibit this behavior, despite their distinct properties, for instance density and characteristic temperature, which for the ionized gas is higher than for the (warm) H I by a factor of $\sim 10 - 100$. We focus on the kinematics of the central regions of three galaxies (Table 5.2) of the THINGS sample by means of integral field spectroscopy, targeting the star forming regions, as traced by the H II regions. The physical size of the observed regions, considering that the VIMOS field of view is $27'' \times 27''$ wide, range between ~ 0.5 kpc and ~ 1.2 kpc, for distances of ~ 4 Mpc and ~ 9 Mpc, respectively, and have a physical sampling size between 13 pc and 30 pc.

Determination of the Ionized Gas Maps

First, we refine the wavelength calibration of the data cubes using a set of ~ 80 sky emission lines (Osterbrock et al. 1997). We use a sub-sample of these lines to estimate the instrumental width. Subsequently, we subtract pixel-by-pixel the background continuum from the data cubes. To determine maps of total flux, characteristic velocity, and σ-width, we target the set of spectral emission lines Hα λ6562.8 Å, [N II] $\lambda\lambda$6548.0, 6583.4 Å, and [S II] $\lambda\lambda$6716.4, 6730.8 Å, which are suitably bright within the available spectral range. For the galaxy NGC 2903 we only use the [S II] lines, since the Hα and [N II] lines are blended with bright sky emission lines. We simultaneously fit the emission lines adopting the same velocity and velocity dispersion, using a single Gaussian profile for each line. However, both the spectral emission lines width of the gas and the instrumental width have been calculated in terms of Gaussian-σ via auto-correlation, which reveals more robust than a direct Gaussian fitting method, being less sensitive to signal-to-noise variations. The observed width of the gas lines is then corrected by instrumental width using the approximation $\sigma_g = (\sigma^2_{g,obs} - \sigma^2_{instr})^{1/2}$, where σ_g is the effective with of the gas lines.

5.4 Results

The pixel-by-pixel scatter plots in a log-log plane for the $\Sigma_{\rm HI}$, σ, and $\Sigma_{\rm SFR}$ maps, although characterized by a considerable scatter, evidence positive mutual

correlations (§ 5.4.1), if considered over the whole galaxy disk, holding for all the galaxies of the sample. Since we find a systematic decline of the H I velocity dispersion with the radial coordinate (§§ 5.4.2 and 5.4.3), as shown in Fig. 5.1, and knowing that the SFR and the H I mass in spiral galaxies also typically decrease with radius, we question whether the observed relations are an effect of the radial coordinate, denoting systematic variations of the environmental conditions. We also show that on local scales, the velocity dispersion and the surface density of the (neutral and ionized) gas are manifestly anti-correlated (§ 5.4.4). This effect could possibly induce the observed scatter in the pixel-by-pixel relations.

5.4.1 Pixel-by-Pixel Relations

From a linear χ^2 fit to the pixel-by-pixel relations in a log-log plane, the observed variables $\Sigma_{\rm HI}$, σ, and $\Sigma_{\rm SFR}$ result correlated for all the galaxies of our sample, including dwarf galaxies. The scatter plots and the orthogonal regression of these relations are displayed in Figs. 5.3, 5.4, and 5.5. The results of the fits are summarized in Fig. 5.6 for all the galaxies of our sample. Here, we enumerate the average power-law indices for each analyzed relation:

- we find $d\log\sigma/d\log\Sigma_{\rm HI} \simeq 0.2$ using the numerical integrated maps, and $\simeq 0.3$ using the Gaussian moments, though we also note a scatter in the indices that overall vary between $\simeq 0.15-0.25$, and $\simeq 0.2-0.5$, respectively for the two considered methods;

- we find $d\log\Sigma_{\rm SFR}/d\log\sigma \simeq 10$, independently on the adopted method, with a general scatter in the indices of $\sim \pm 2$;

- ultimately, we find $d\log\Sigma_{\rm SFR}/d\log\Sigma_{\rm HI} \simeq 2 \pm 1$ using the numerical integrated maps, and $\simeq 3.5 \pm 1$ using the Gaussian moments. These values agree well with previous studies on the Kennicutt-Schmidt law (Murgia et al. 2002; Wong & Blitz 2002).

The resulting power-law slopes of these relations do not exhibit any remarkable dependence with the dynamical mass. Moreover, we note the overall constance of the zero-points of the power-law relations. In particular, for a fiducial value of surface density mass $\Sigma_{\rm HI} = 3\ {\rm M}_\odot\,{\rm pc}^{-2}$, we find that the velocity dispersion is $\simeq 10$ km s^{-1}, resulting from the numerical integrated maps, and $\simeq 7$ km s^{-1}, from the Gaussian moments, and a general value for the SFR of $\log\Sigma_{\rm SFR}[{\rm M}_\odot\,{\rm yr}^{-1}\,{\rm pc}^{-2}] \simeq -9.5$. The zero-points of these relations do not display a clear dependence with the dynamical mass.

The differences in the results from the two adopted independent methods, numerical direct integration and Gaussian fitting, could be due to some constraints that we applied to our galaxies. First, we only consider Gaussian fits with a signal-to-noise S/N ≥ 6, which generally clips out low values of $\Sigma_{\rm HI}$, and consequently of $\Sigma_{\rm SFR}$. However, we stress that after checking the fit quality at random (x, y) points in the data cubes, we note that a fiducial cut of

S/N ≥ 4 is sufficient to retain only good fits. Second, in the presence of tidal or extra-planar H I clouds or in general multiple kinematically disconnected clouds, the variance calculated by numerical integration overestimates the actual value of the line width, which instead can better recovered by a Gaussian fit. Note that a flat power spectrum noise has zero average signal, but non-zero variance. In contrast, any functional fit, and in particular the Gaussian one, generally smooths out these multiple features, underestimating the total column density $\Sigma_{\rm HI}$, and, consequently, for a fiducial S/N ≥ 6, low values of σ and $\Sigma_{\rm HI}$ are simultaneously preferred. Third, we remark that the $\Sigma_{\rm SFR}$ maps are possibly not sufficiently reliable at low regimes of SFR, due to contaminations in the 24 μm maps. We will discuss this aspect in the next section.

5.4.2 Radial Profiles of σ

An important result emerging from our analysis is the radial dependence of the H I velocity dispersion, common to all the sample galaxies. Through the tilted ring sampling of the σ maps we find that $\sigma(r)$ exhibits a radial decline with a slope approximately constant over several optical radii for $r \geq 0.5\, r_{25}$. The radial profiles of σ are plotted in Fig. 5.1 for all the galaxies in our sample. The velocity dispersion decreases with radius by $\simeq 3-5$ km s^{-1} every unit of r_{25}. Remarkably, we also find a general value of $\sigma_{25} \equiv \sigma(r = r_{25}) \simeq 10 \pm 1$ km s^{-1}, which displays no apparent trend with the dynamical mass. The mass-weighted median value of the velocity dispersion is also consistent with σ_{25}. The resulting values of the radial slopes, σ_{25}, and median of σ are summarized in Fig. 5.2. As we also show in § 5.4.1, this common value emerges in correspondence of the same value of stellar surface brightness as traced by r_{25}, indicating that similar environmental conditions reflect in similar common values of velocity dispersion, H I surface density, SFR and stellar surface density.

5.4.3 Relations in Radial Bins

After binning the maps in radial bins we note that the bin-by-bin relations, which are plotted in Figs. 5.7, 5.8, and 5.9, result considerably similar to the pixel-by-pixel relations, since the trends agree well with the slopes found in § 5.4.1. More importantly, the relations analyzed in radial bins indicate that the observed maps, $\Sigma_{\rm HI}$, σ, and $\Sigma_{\rm SFR}$ display a smooth transition between neighboring bins. In fact, the data points in the plot of Figs. 5.7, 5.8, and 5.9 are manifestly not sparse but orderly distributed, indicating a monotonic dependence of $\Sigma_{\rm HI}(r)$, $\sigma(r)$, and $\Sigma_{\rm SFR}(r)$ individually with radius, and consequently also mutually whit each other. Nevertheless, for a few galaxies of the sample, this monotonic dependence breaks for $\Sigma_{\rm HI}$ at small radii in correspondence with the central H I depression, where the gas is predominantly molecular.

5.4.4 Local (qualitative) Relations

In contrast to the pixel-by-pixel and radial bins relations, the H I velocity dispersion appears to be anti-correlated with the H I surface density map on small scales, and consequently also with the SFR map, since in Chapter 4 (Tamburro et al. 2008) we have shown that $\Sigma_{\rm HI}$ and 24 μm correlate well. Throughout the whole thickness of the H I spiral arms, on physical sizes of ~ 1 kpc, σ exhibits values lower than in the inter-arm regions by ~ 8 km s^{-1}, and the H I holes, on scales of ~ 2 kpc, are filled with higher values of σ. This pattern can be visualized i.e. for M51 and NGC 3134 in Fig. 5.12 and Fig. 5.13, respectively, by comparing σ and $\Sigma_{\rm HI}$ in a contour plot of the maps and pixel-by-pixel in concentric deprojected rings. The scatter plot σ-$\Sigma_{\rm HI}$, from a galactocentric radius of $\sim 0.5\,r_{25}$ up to $\sim 1.5\,r_{25}$ (corresponding to $\sim 4.6 \rightarrow 13$ kpc and $\sim 5.8 \rightarrow 17$ kpc for M51 and NGC 3184, respectively) , that is where the galaxies are not molecular gas dominated, and for individual concentric rings of $15''$ width each (~ 580 kpc and ~ 730 kpc for M51 and NGC 3184, respectively) display a relation different from the fit over the whole galaxy. While the resulting power-law slope for a global fit is ~ 0.15, slopes for individual rings range between -0.3 and 0.0 approximately, although NGC 3184 exhibits positive correlation σ-$\Sigma_{\rm HI}$ at about $r \sim 0.5\,r_{25}$. A similar conclusion has been also delineated by (Hunter, Elmegreen, & van Woerden 2001) in the irregular galaxy NGC 2366 (not in our sample), where peaks of Hα locally coincide with dips of H I velocity dispersion, and vice versa.

In addition, a similar pattern emerges from the ionized gas regions in the centers of the galaxies of our VIMOS sample, as traced by the recombination (and forbidden) lines and the associated velocity dispersion. The comparative plots of H II emission and corresponding σ are displayed in Fig 5.14. However, the physical scale sizes of the anti-correlated features evidenced by the ionized gas maps are smaller than those from the H I gas by a factor of ~ 10, being of the order of $\sim 100 - 300$ pc.

5.5 Discussion

Through a comparative study (§§ 5.4.1 and 5.4.2) of the observed maps of $\Sigma_{\rm HI}$, σ, and $\Sigma_{\rm SFR}$, we find on galactic scales a global trend of the H I velocity dispersion both with the H I gas surface density and with the SFR. Now, we consider four possible scenarios and discuss their expectations and feasibility in light of the empirical results enumerated in the previous section. (1) If star formation drives the turbulence of the ISM through stellar feedback and explosions of SNe, then $\Sigma_{\rm SFR}$ and σ are expected to be connected by an energy balance between the kinetic energy associated to the H I turbulence and the feedback $1/2\,\Sigma_{\rm HI}\,\sigma^2 = \epsilon\,E_{\rm SFR}$, where $E_{\rm SFR} \propto \Sigma_{\rm SFR}$, and $\epsilon = const$ is the feedback efficiency, which expresses the ability of the ISM to absorb energy from star formation processes feedback and convert it into turbulent motions. (2) If the interstellar turbulence drives the star formation by facilitating random density

enhancements, also in this case $\Sigma_{\rm SFR}$ and σ are expected to correlate, although it is not obvious how, analytically speaking. (3) If the turbulence operates against the cloud condensation and collapse, quenching star formation, then $\Sigma_{\rm SFR}$ and σ are expected to anti-correlate. (4) Ultimately, we also consider a scenario where turbulence and SFR are not directly coupled, but both $\Sigma_{\rm SFR}$ and σ independently correlate with $\Sigma_{\rm HI}$, ensuing their apparent mutual correlation. In these circumstances, the connection between $\Sigma_{\rm HI}$ and $\Sigma_{\rm SFR}$ is regulated by the onset of gravitational instability, and the amplitude of σ is regulated by the gravitational potential of the disk – in part traced by $\Sigma_{\rm HI}$.

In support of the assertions of point (4), we recall that the gravity alone can ensue the gas cloud collapse and reproduce the star formation laws – regardless whether the ISM is magnetized or not (e.g. Li et al. 2005, 2006). Moreover, the intensity of the gravitational potential along the vertical direction determines the pressure equilibrium, and, specifically, the regime of vertical velocities. Provided that the potential also establishes the strength of gravitational instability, a correlation between $\Sigma_{\rm SFR}$ and σ reveals reasonable. It is worth reminding that the gravitational potential constitutes a limit to the SFR, by setting the rotation velocity of the galaxy, and therefore the amplitude of the Coriolis force, which, unlike local self-gravity, acts against the cloud collapse.

In the next sections we discuss in detail the implications of the three sets of relationships. Before doing so, we must stress the following caveat. It is risky to assess and interpret the star formation laws if we only consider the H I gas, first, because the total gas mass (H I + H_2) establishes the rate of star formation at a level where the molecular fraction becomes important, while in H I dominated regions star formation proceeds at lower efficiency responding to a different empirical law (Heyer et al. 2004; Kennicutt et al. 2007; Bigiel et al. 2008), second, because a stability criterion Q_{sg} that includes both gas and stars (e.g. Rafikov 2001) can explain the star formation thresholds observed in galaxies, while a Toomre-Q_g parameter, that only takes into account the gas, has proven problematic (Boissier et al. 2003; Leroy et al. 2008). Though these issues do not directly relate to our primary goal, the H I mass – without stellar mass – is scarcely useful for tracing the vertical potential, and even if the stellar surface mass Σ_s is provided, the z-distribution of the stars is difficult to estimate, unless the velocity dispersion σ_s is known.

5.5.1 $\Sigma_{\rm HI}$-$\Sigma_{\rm SFR}$

The logarithmic slope $d\log\Sigma_{\rm SFR}/d\log\Sigma_{\rm HI} \simeq 2 \pm 1$ that we find for our sample galaxies (§ 5.4.1), and the global trends $\Sigma_{\rm HI}$ vs $\Sigma_{\rm SFR}$ (Figs. 5.5 and 5.9), are in agreement with previous similar studies as we discuss here. It has been well established that while the total gas (H I + H_2) mass on sub-kpc scales agrees with the Kennicutt-Schmidt law with a power-law index of 1.4, $\Sigma_{\rm SFR}$ has a steeper correlation with $\Sigma_{\rm HI}$ individually, or no correlation at all where the gas fraction is predominantly molecular, for instance towards the center of galaxies where the H I surface density saturates at $\sim 9\,{\rm M}_\odot\,{\rm pc}^{-2}$ (Murgia et al. 2002; Wong & Blitz 2002; Kennicutt et al. 2007; Bigiel et al. 2008). Moreover,

the large scatter observed in the relation might be due to real fluctuations of the SFR, and unlikely to observational uncertainties. The $\Sigma_{\rm HI}$-$\Sigma_{\rm SFR}$ relation plotted in radial bins is characterized by a smooth continuity, which has also been presented i.e. by Wong & Blitz (2002), throughout the whole disk for all the galaxies in our sample. In conclusion, not only the star formation law has to be cautiously interpreted at high regimes of $\Sigma_{\rm HI}$, but we also point out that the $\Sigma_{\rm SFR}$ maps are not fully reliable at low regime of SFR. At lower metalicity the UV photons have a longer mean free path, due to the lower dust content in the ISM. There, the 24 μm emission maps are possibly tracing dust heated by UV radiation in part from local and in part from neighboring star forming regions. This might change the correct interpretation of SFR maps obtained with 24 μm + FUV emission, thus influence the slopes of the $\Sigma_{\rm HI}$-$\Sigma_{\rm SFR}$ derived here. As an alternate possibility, the GALEX FUV emission could be used in order to trace the unobscured SFR at the level of low densities of dust.

The mechanism that drives the star formation laws is apparently due to the strength of gravitational instability, but the $\Sigma_{\rm HI}$-$\Sigma_{\rm SFR}$ relation and, in particular, the Kennicutt-Schmitt law for H I-dominated galaxies may have a slight different explanation, where also star formation efficiency is likely to play a determinant role.

5.5.2 $\Sigma_{\rm HI}$-σ

For all the galaxies in our sample we observe a correlation between H I surface density mass and the velocity dispersion that holds typically for all radii $r > 0.5\, r_{25}$ and in some cases down to smaller radial coordinates (Figs. 5.3 and 5.7). Specifically for a fraction of the sample galaxies, the central depression of H I – where the H I gas is converted into H_2 efficiently – produces a change in the gradient of the radial profile of $\Sigma_{\rm HI}$, which diminishes at small radii, while σ grows monotonically towards the center. The global trend that we measure in § 5.4.1 evidences a power-law $\Sigma_{\rm HI} \sim \sigma^{4-5}$. We question whether this relation is due to a pressure equilibrium condition.

The equilibrium condition of a fluid supported by pressure against the gravitational force is expressed by the equation (e.g. Binney & Tremaine 1987, p. 199):

$$\frac{1}{\rho_j}\,\frac{dp_j}{dz} = \sigma_{z,j}^2\,\frac{d\ln\rho_j}{dz} = \frac{d\phi}{dz} \tag{5.8}$$

where the pressure of the fluid is $p_j = \rho_j\,\sigma_{z,j}^2$, in the assumption that the system is isothermal, specifically where the vertical velocity dispersion σ_z is independent of z. According to Spitzer (1942) the pressure equilibrium equation (5.8) is valid for a system composed by more than one fluid, and for each j-th fluid independently, for instance gas and stars $j = g, s$. Subsequently, the Poisson equation for a flattened axisymmetric system (e.g. Binney & Tremaine 1987, p. 48),

$$\frac{d^2\phi}{dz^2} = 4\pi G\,\rho, \tag{5.9}$$

where $\rho = \rho_g + \rho_s$ is the total mass density, can be combined with Eq. 5.8. This, adopting a vertical distribution $\rho_j(z) = \rho_j(0)\,\exp(-z^2/h_j^2)$, where the effective width $2\,h_j$ is given by $h_j^2 = \sigma_{z,j}^2\,[2\pi G\,(\rho_g + \rho_s)]^{-1}$, yields the invariant (cf. Talbot & Arnett 1975):

$$\tau^{-1} = \frac{\sigma_{z,j}}{h_j} = \pi G\,\left(\frac{\Sigma_g}{\sigma_{z,g}} + \frac{\Sigma_s}{\sigma_{z,s}}\right) \tag{5.10}$$

where τ is the crossing time of the vertical motions along the z direction.

We assume hereafter assume that the H I velocity dispersion in the disk is isotropic. Since the galaxies in our sample are not highly inclined, this assumption should not influence much our results. In these circumstances, we expect that the H I velocity dispersion is indeed correlated with the H I surface density mass. In the simplistic case of a single component, the gas velocity dispersion relates to the surface density through $\sigma_g = (2\pi G\,\Sigma_g\,h_g)^{1/2}$. Yet, none of the galaxies of our sample exhibits a power-law index of 0.5 for σ vs $\Sigma_{\rm HI}$, rather, we observe indices of $\sim 0.2 \pm 0.05$, consistent with $\sigma_g \propto (\rho_g + \rho_s)^{1/2} \simeq (\Sigma_g\,h_g + \Sigma_s\,h_s)^{1/2}$. Accordingly, the relation σ_g-Σ_g, expressed in Eq. 5.10, is slightly more complex in the case where two fluids coexist in pressure equilibrium. Consequently, σ_g is sensitive, on the one hand, both to Σ_g and Σ_s, and, on the other hand, to the ratio Σ_s/σ_s, which denotes the strength of the potential in the vertical direction. In conclusion, the mechanism that is possibly establishing the regime of velocity dispersion in the gas disk is the gravity, which casts, although, a premature conjecture since σ_s is an unknown variable.

5.5.3 $\Sigma_{\rm SFR}$-σ

A direct interpretation for the observed correlation between SFR and velocity dispersion in the H I is apparently less obvious than the previously discussed relationships. Recalling the results for the $\Sigma_{\rm SFR}$-σ relations, (1) we obtain from the numerical integrated maps: $\Sigma_{\rm HI} \sim \sigma^{4-5}$ and $\Sigma_{\rm SFR} \sim {\Sigma_{\rm HI}}^2$, which combined yield $\Sigma_{\rm SFR} \sim \sigma^{8-10}$, approaching our empirical finding $\Sigma_{\rm SFR} \sim \sigma^{10}$, and (2) from the Gaussian moments maps we obtain $\Sigma_{\rm HI} \sim \sigma^3$ and $\Sigma_{\rm SFR} \sim {\Sigma_{\rm HI}}^{3.5}$, formally yielding $\Sigma_{\rm SFR} \sim \sigma^{10.5}$, which is also nearly resembling the empirical value $\Sigma_{\rm SFR} \sim \sigma^{10}$. Note, however, that the difference in the results between these two independent methods is likely due to a fiducial S/N cut for the Gaussian fit method, that causes a lack of data points at low regimes of $\Sigma_{\rm HI}$ and, consequently, of $\Sigma_{\rm SFR}$. Although, this is remarkably reducing the bias due to the 24 μm map at low regimes of SFR, in particular for the outermost regions of our sample galaxies. To summarize, the positive correlation $\Sigma_{\rm SFR}$-σ is compatible with star formation driving turbulence, but the power-law indices for the $\Sigma_{\rm SFR}$-σ relations are also compatible with an indirect connection between SFR and turbulence in the H I gas.

$\Sigma_{\rm SFR}$-E_k

Comparing pixel-by-pixel the SFR and the surface density of the H I kinetic energy of the turbulent motions implied by $E_k = 1/2\,\Sigma_{\rm HI}\,\sigma^2$ (see Fig. 5.10) we find that the global trend is consistent with the unity slope. We construct a data set of $\Sigma_{\rm HI}$, σ, and $\Sigma_{\rm SFR}$ maps composed of all the data points of the sample galaxies (last panel of Fig. 5.10). The fitted logarithmic slope to the overall set of data points yields $\Sigma_{\rm SFR} \sim E_k^{1.3}$, which we argue to be a lower limit, since the the data points at low regime of SFR could be flattening the fitted slope. To avoid this selection effect we suggest the following operation. We recalculate the SFR maps using 24 μm + FUV flux for $\Sigma_{\rm SFR24\mu m+FUV}$ higher than a fiducial threshold $\Sigma_{{\rm SFR}thresh} = 3 \times 10^{-10}$ M$_\odot$ year^{-1} pc^{-2}; for $\Sigma_{\rm SFR24\mu m+FUV} < \Sigma_{{\rm SFR}thresh}$ then $\Sigma_{\rm SFR}$ is calculated using the FUV flux only; we reject data points with $\Sigma_{\rm SFR24\mu m} < \Sigma_{{\rm SFR}thresh}$ and at a galactocentric distance $r > 1.5\,r_{25}$. This masking reduces the bias introduced by the 24 μm emission at low SFR. The trend in the pixel-by-pixel scatter plot (see Fig. 5.11) results in fact steeper than for the unmasked data, as also evidenced by the fitting to the overall set of data points, which yields $\Sigma_{\rm SFR} \sim E_k^{1.5}$ (last panel of Fig. 5.11). The results are compatible with star formation driving some part of the H I turbulence. Note however that the relation $\Sigma_{\rm HI} \sim \sigma^{4-5}$ also yields independently $E_k = 1/2\,\Sigma_{\rm HI}\,\sigma^2 \sim \sigma^{8-10}$, which is similar to our empirical result $\Sigma_{\rm SFR} \sim \sigma^{10}$, suggesting that an indirect connection between $\Sigma_{\rm SFR}$ and E_k also holds.

The relation $\Sigma_{\rm SFR}$-E_k qualitatively agrees with the (logarithmic) linear relation $\log \Sigma_{\rm SFR} = -12 + \log E_k$ (the dashed line in Fig. 5.10), where a value of $\Sigma_{\rm SFR} = 10^{-9}$ M$_\odot$ year^{-1} pc^{-2} implies $E_k = 10^{46}$ erg pc^{-2}, which is the energy release of 10^{-5} SNe pc^{-2}. Can a stellar population with a rate of star formation of 10^{-9} M$_\odot$ year^{-1} produce 10^{-5} SNe? Assuming a Salpeter initial mass function, the fraction of stars that end in (type II) SNe is

$$f_{*\rightarrow {\rm SN}} = \frac{\int_{8\,{\rm M}_\odot}^{100\,{\rm M}_\odot} m^{-2.35}\,dm}{\int_{0.1\,{\rm M}_\odot}^{100\,{\rm M}_\odot} m^{-2.35}\,dm}, \tag{5.11}$$

then the SN rate is

$$\eta = \frac{{\rm SFR} \times f_{*\rightarrow {\rm SN}}}{\langle m \rangle}, \tag{5.12}$$

where $\langle m \rangle$ is the average mass of the population

$$\langle m \rangle = \frac{\int_{0.1\,{\rm M}_\odot}^{100\,{\rm M}_\odot} m^{-1.35}\,dm}{\int_{0.1\,{\rm M}_\odot}^{100\,{\rm M}_\odot} m^{-2.35}\,dm}. \tag{5.13}$$

For a SFR of 10^{-9} M$_\odot$ year^{-1} the ratio between the total energy release in units of SN and the SN rate $(10^{-5}$ SNe$)/\eta \equiv \tau = \epsilon\,\tau_D$ results $\tau \simeq 1.3$ Myr, where $\epsilon = E_k/E_{\rm SFR}$ is the feedback efficiency and $\tau_D = E_k/\dot{E}_k$ is the decay time of the turbulence. Mac Low (1999) estimates the turbulence decay time for a driving scale of 100 pc size and $\sigma = 10$ km s^{-1} to be $\tau_D \simeq 9.8$ Myr, which yields $\epsilon \simeq 0.13$.

Implications

The positive relations $\Sigma_{\rm SFR}$-σ and $\Sigma_{\rm SFR}$-E_k are suggesting that star formation feedback could be effectively sustaining a substantial fraction of the velocity dispersion of the H I. Though the power-law slope implied by $E_k = \epsilon\, E_{\rm SFR}$ slightly conflicts with the observed one, ~ 1.5, we can not rule out star formation feedback as a potential driver of turbulence as long as $E_k < E_{\rm SFR}$. Moreover, the shallow dependence SFR with σ from $\sigma \sim \Sigma_{\rm SFR}^{1/10}$ precludes that turbulence is able to induce star formation by producing stochastic density enhancements. An alternate implication of these results is that SFR and σ are only indirectly connected with each other through two relations that are consequential of (1) the onset of gravitational instability, which is facilitated at high regimes of gas mass, and (2) the dynamical velocity dispersion which is maintained by the vertical gradient of the gravitational potential. Alternatively, large scale gravitational instability, or disk instabilities in general, are able to produce large scale deviations from the laminar flow of the gas orbiting in the galactic potential. Note, in fact, that the velocity dispersion would increase accordingly with the strength of the onset of gravitational instability, traced only in part by $\Sigma_{\rm HI}$, but sensibly by $\Sigma_{\rm SFR}$. This last picture would also be consistent with out results. However, it is difficult to irrefutably assess to which of the available processes has to be attributed the label of driving mechanism, since different logical lines of reasoning potentially arrive at analogous logical conclusions.

5.6 Conclusions

We investigate the H I velocity dispersion as function of the environmental conditions – surface density maps of H I mass and SFR. In particular, we focus on the interplay between σ and SFR in order to understand the long-standing question: at what level is star formation activity, through SNe explosions, hot stars winds, etc., able to inject energy into the ISM? With this purpose, we test the relationships among the observed variables $\Sigma_{\rm HI}$, σ, and $\Sigma_{\rm SFR}$, using H I maps from THINGS, and SFR tracer maps from SINGS.

For our sample galaxies we find that the H I velocity dispersion and SFR are correlated with the power-law $d\log\Sigma_{\rm SFR}/d\log\sigma \simeq 10 \pm 2$. Moreover, we find radial systematic decline of H I velocity dispersion which varies from galaxy to galaxy between 2 and 5 km s^{-1} per unit r_{25}, but a common value for all the galaxies of the sample of $\sigma_{25} \equiv \sigma(r = r_{25}) \simeq 10$ km s^{-1}.

Our results are open to the possibility that star formation feedback could be effectively driving the observed regime of σ, although, we note a small discrepancy between the observed power-law indices and those expected from this scenario. Also, provided that $\sigma \sim \Sigma_{\rm SFR}^{1/10}$, it proves unlikely that turbulence could ensue star formation via stochastic density waves – although it is not obvious how to test this analytically – since, according to the relation $\Sigma_{\rm SFR}$-σ, for slightly different values of σ any corresponding regime of SFR is allowed. Ultimately, we consider the emergent possibility, although premature, that SFR and

Obj. name	Alt. name	R_{25} ($'$)	i ($^\circ$)	PA ($^\circ$)	D (Mpc)	$v_{\rm max}$ (km s^{-1})
		(1)	(2)	(3)	(4)	(5)
NGC 3184		3.62	16	179	11.1	260
NGC 3351	M95	3.54	41	192	9.33	210
NGC 4214		3.38	43.7	65	2.94	56
NGC 4736	M94	3.88	41.4	296.1	4.66	167
NGC 5055	M63	6.01	59	102	7.82	209
NGC 5194	M51	4.89	42	172	7.77	241
NGC 628	M74	4.77	7	20	7.3	219
NGC 6946		5.35	32.6	242	5.5	201
NGC 7793		5.0	50	290	3.82	109
IC 2574		6.44	53.4	55.7	4.02	73
HOII		3.3	41	177	3.39	38

Table 5.1: THINGS and SINGS target galaxies. (1): semi-major axis of the 25 mag arcsec^{-2} isophote in the B band obtained from the LEDA database (URL: http://leda.univ-lyon1.fr/); (2) and (3): kinematic inclination and PA, respectively; (4): adopted distance; (5): maximum amplitude of the rotation velocity corrected for inclination.

Obj. name	Alt. name	R_{25} ($'$)	i ($^\circ$)	PA ($^\circ$)	D (Mpc)	Note
		(1)	(2)	(3)	(4)	
NGC 2903		5.6	65.2	204.3	8.9	not in SINGS
NGC 5236	M83	7.06	24	225	4.47	not in SINGS
NGC 7793		5.0	50	290	3.82	in main sample

Table 5.2: THINGS target galaxies observed with VIMOS-IFU. (1): r_{25}; (2) and (3): kinematic inclination and PA, respectively; (4): adopted distance.

σ are independently connected with each other, and they only couple through relations due to the gravitational instability and the local gravity. Note, in fact, that the the highest probability for gravitational instability to set on is where the gravity is sufficiently strong in order to prevail on the forces that disperse the gas.

For the immediate future, we propose a few follow-up procedures. First, we stress the need to improve our estimate of the $\Sigma_{\rm SFR}$ maps at low regimes of SFR. Second, it is essential to examine how the considered relationships hold both within radial bins and, more interestingly, on small sub-samples. Third, we recall that we have not considered yet completeness effects while fitting the power-law slopes. Last, in order to establish the validity of the condition, where the two components (warm) H I gas, and stars are coexisting in equilibrium at two different regimes of velocity dispersion, we need to measure the stellar velocity dispersion.

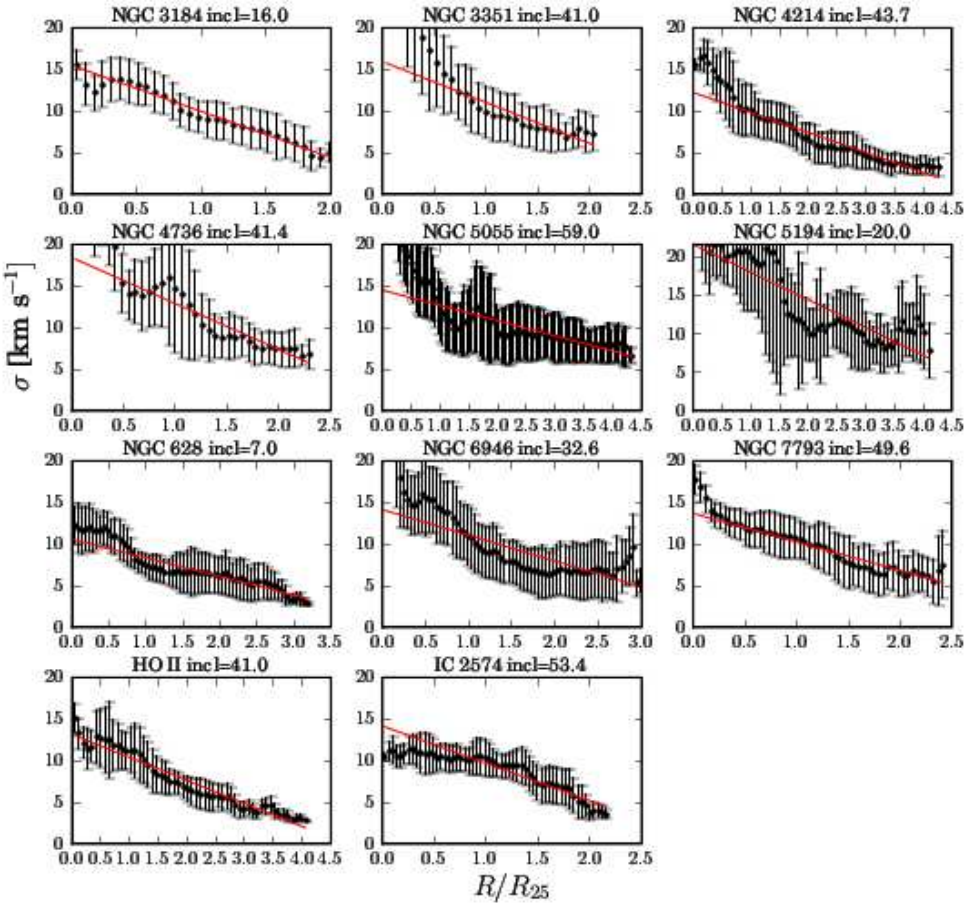

Figure 5.1: Radial profiles of σ for the galaxies of our sample. The symbols represent the average value of σ as function of radius r in units of r_{25}. The error bars denote the 1-standard deviation scatter of σ for te corresponding r. The solid lines denote the linear fit to $\sigma(r)$ for all $r > r_{25}$.

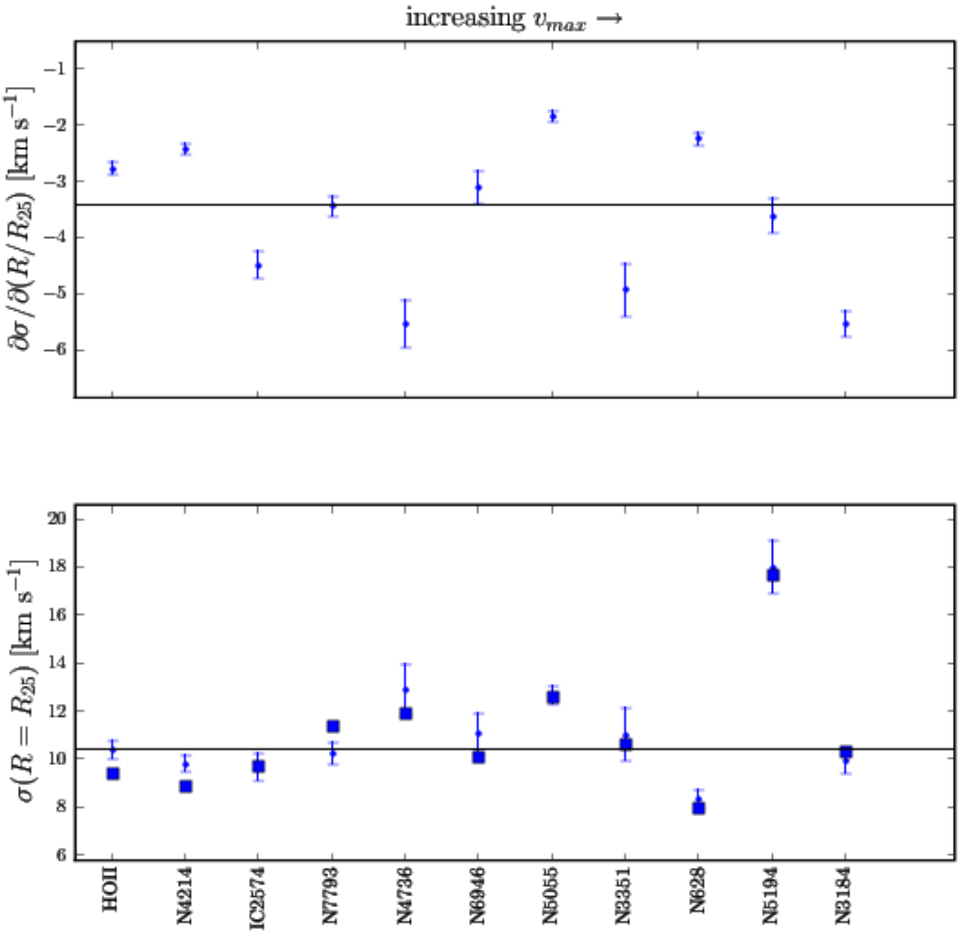

Figure 5.2: Top: the symbols represent the slope in units of r_{25} of the linear fit to the radial profile of σ, or, in other words, the decrease in km s^{-1} for every radial outward step of r_{25}. Bottom: the circles and the corresponding error bars represent the value of $\sigma_{25} \equiv \sigma(r = r_{25})$ resulting from the linear fit for each individual galaxy of the sample; the square symbols represent the $\Sigma_{\rm HI}$-weighted median of σ. The labeled galaxies are sorted by increasing dynamical mass ($v_{\rm max}$).

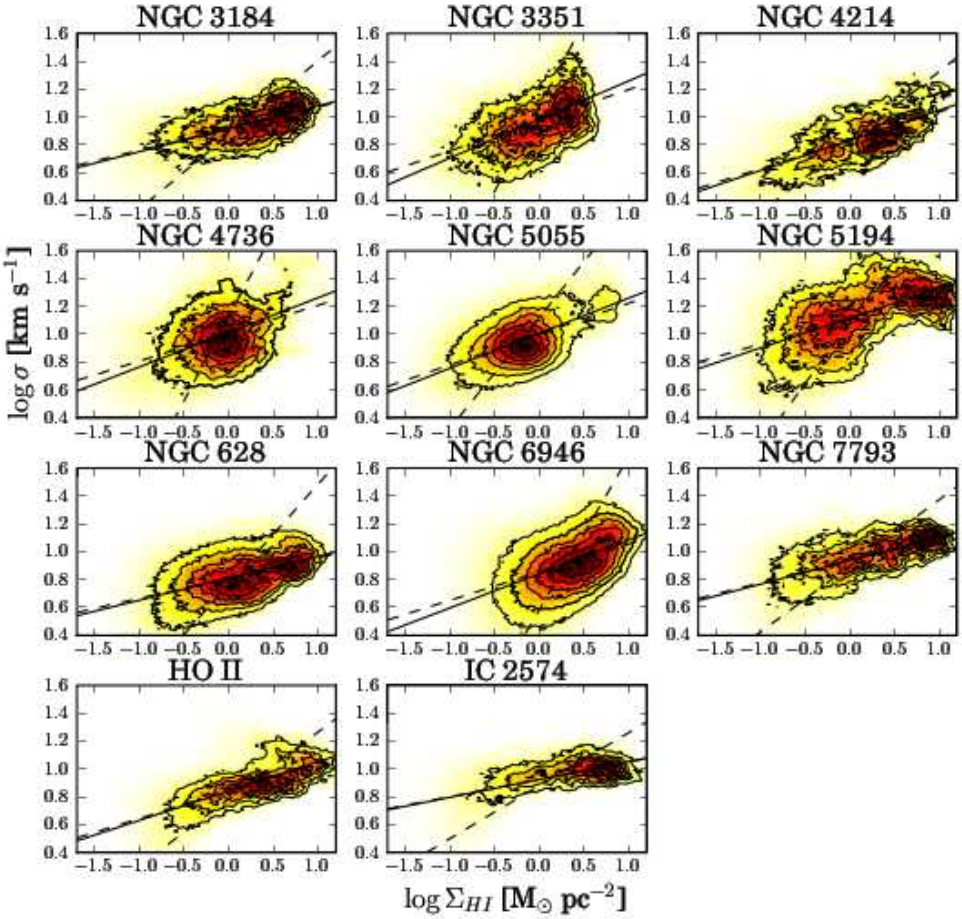

Figure 5.3: Pixel-by-pixel scatter plot of σ vs $\Sigma_{\rm HI}$ for all the galaxies of our sample. The solid line represents the orthogonal regression line (see text). The two dashed lines represent the OLS($Y|X$) and OLS($X|Y$) lines.

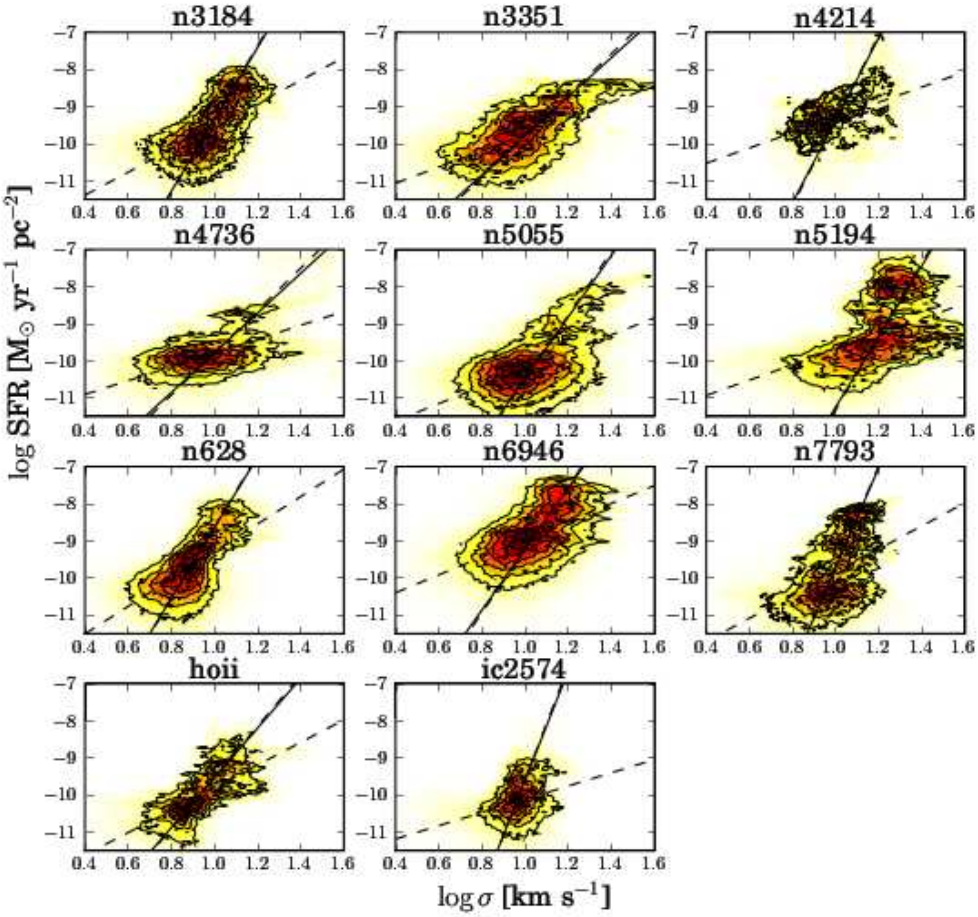

Figure 5.4: Pixel-by-pixel scatter plot of $\Sigma_{\rm SFR}$ vs σ. See Fig. 5.3 for further description.

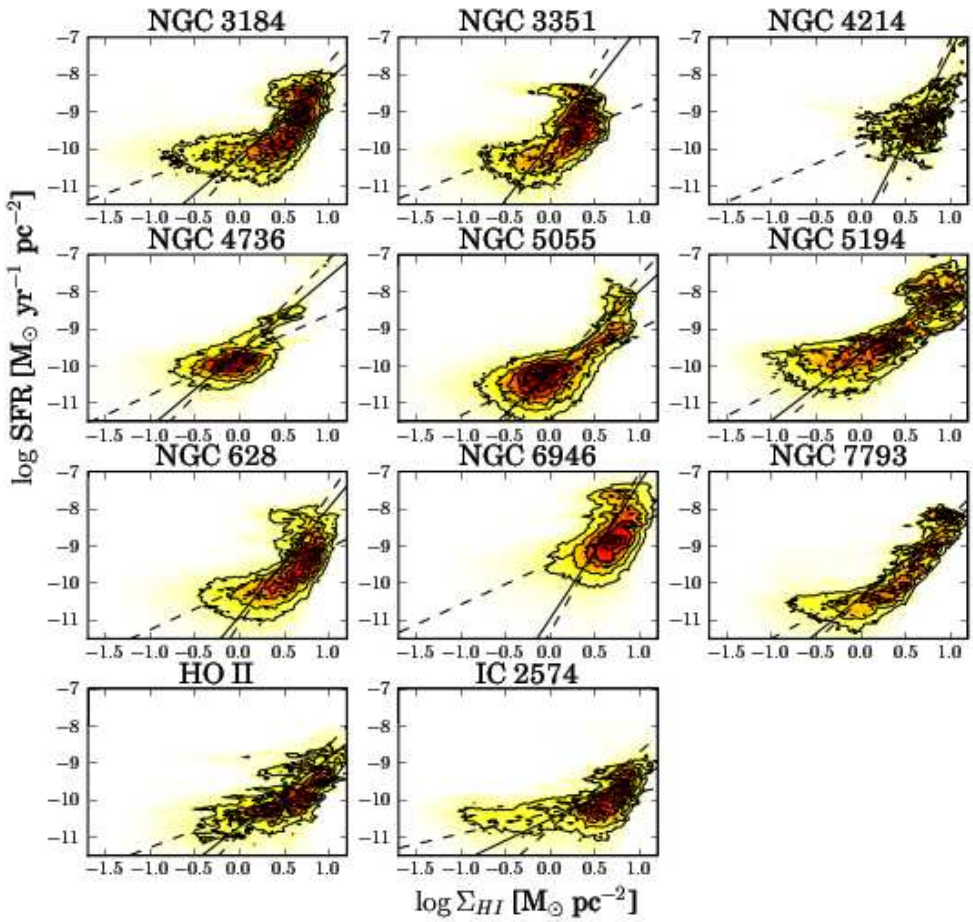

Figure 5.5: Pixel-by-pixel scatter plot of $\Sigma_{\rm SFR}$ vs $\Sigma_{\rm HI}$. See Fig. 5.3 for further description.

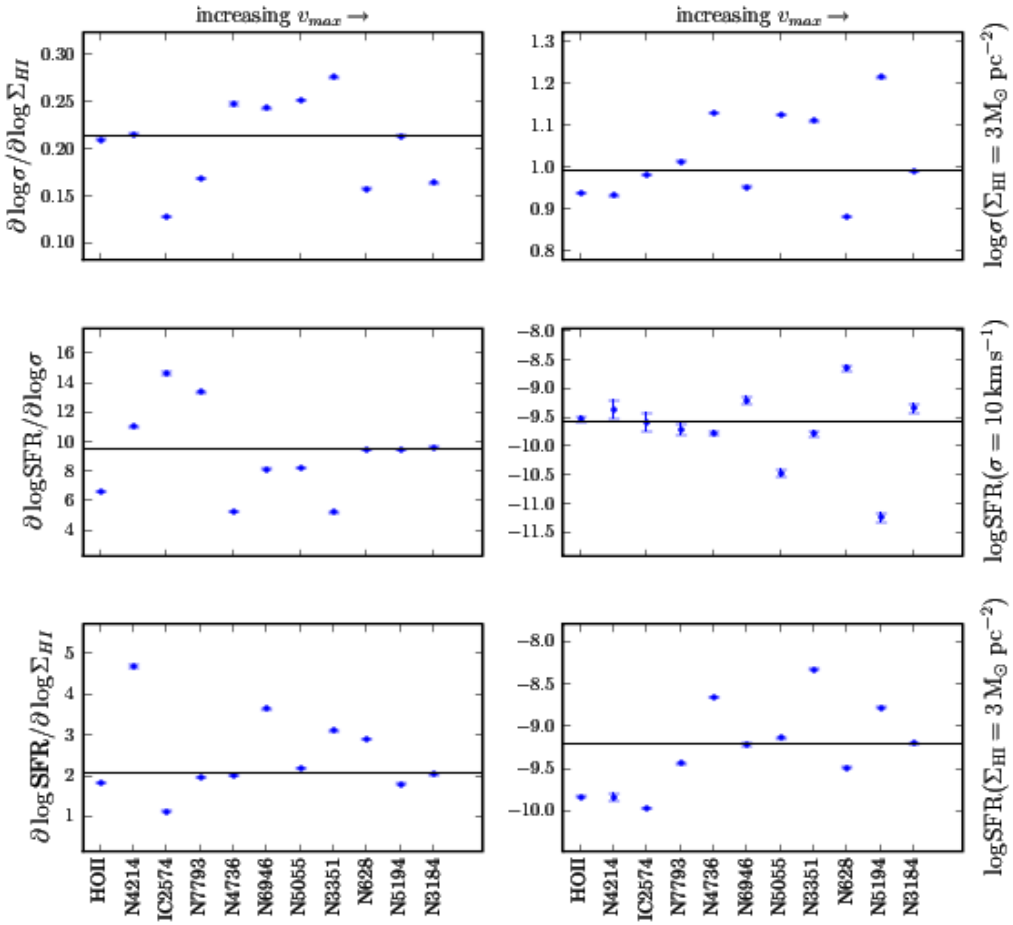

Figure 5.6: Left column: the symbols represent the logarithmic slopes of the relations σ-$\Sigma_{\rm HI}$, $\Sigma_{\rm SFR}$-σ, and $\Sigma_{\rm SFR}$-$\Sigma_{\rm HI}$ for each individual galaxy of the sample. Right column: the symbols represent thezero-points of these relations, where σ is expresed in km s^{-1} and $\Sigma_{\rm SFR}$ in units of M$_\odot$ yr^{-1} pc^{-2}; in each panel the solid horizontal lines represents the median value of the corresponding plotted variable. The labeled galaxies are sorted by increasing dynamical mass ($v_{\rm max}$).

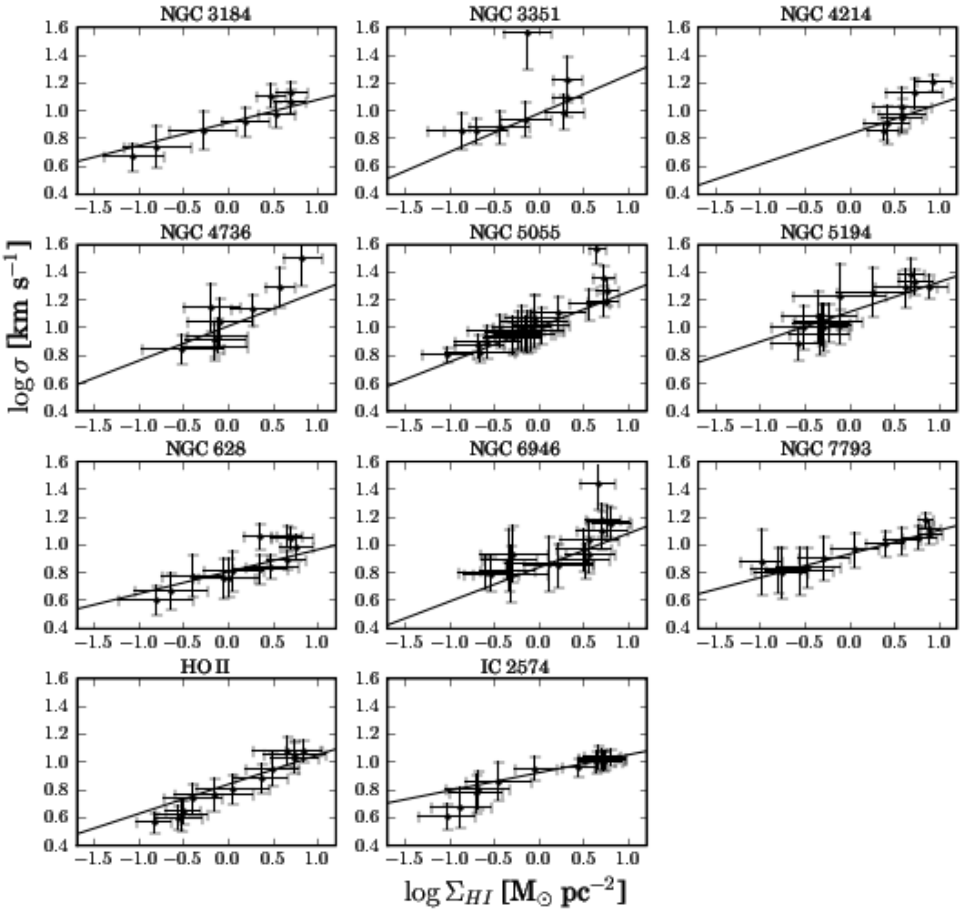

Figure 5.7: The symbols resample the σ vs $\Sigma_{\rm HI}$ relation similarly to Fig. 5.3, but in radial bins; the error bars indicate the 1-standard deviation scatter of the corresponding variables. The innermost to the outermost bins are orderly denoted by highest to the lowest values of σ. For comparison, the solid line denotes the best fit to the pixel-by-pixel scatter plots.

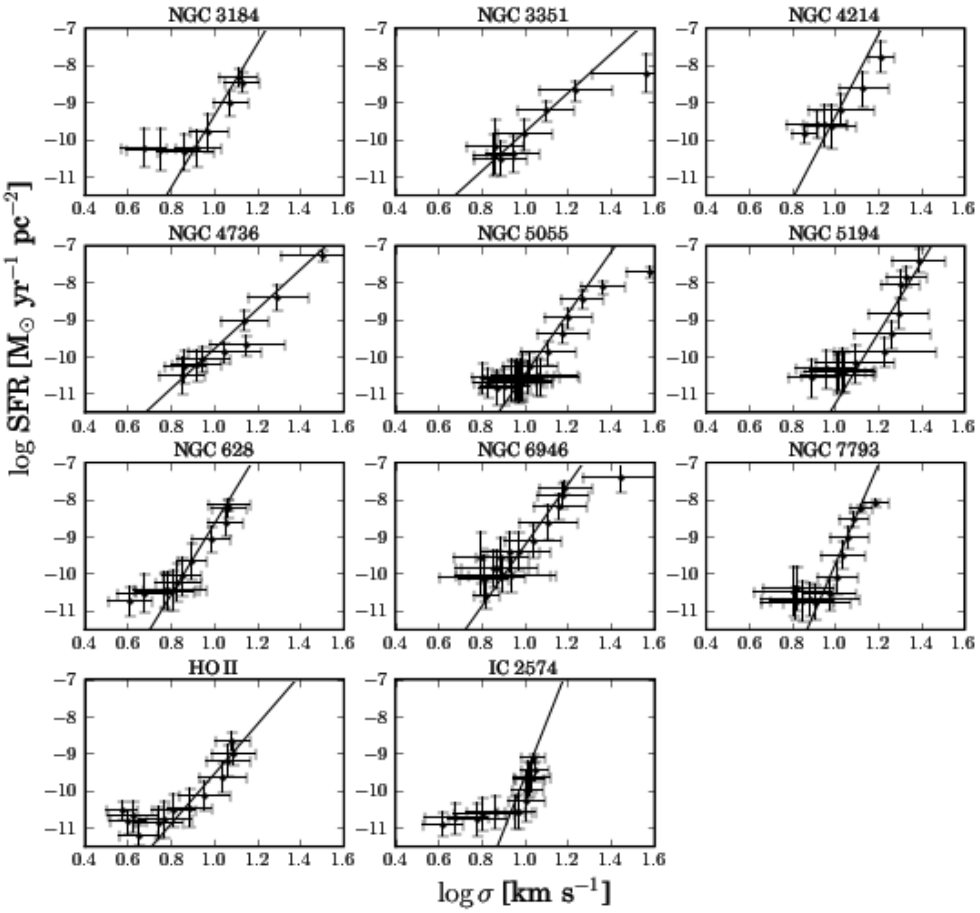

Figure 5.8: The $\Sigma_{\rm SFR}$ vs σ relation in radial bins. See Fig. 5.7 for further description.

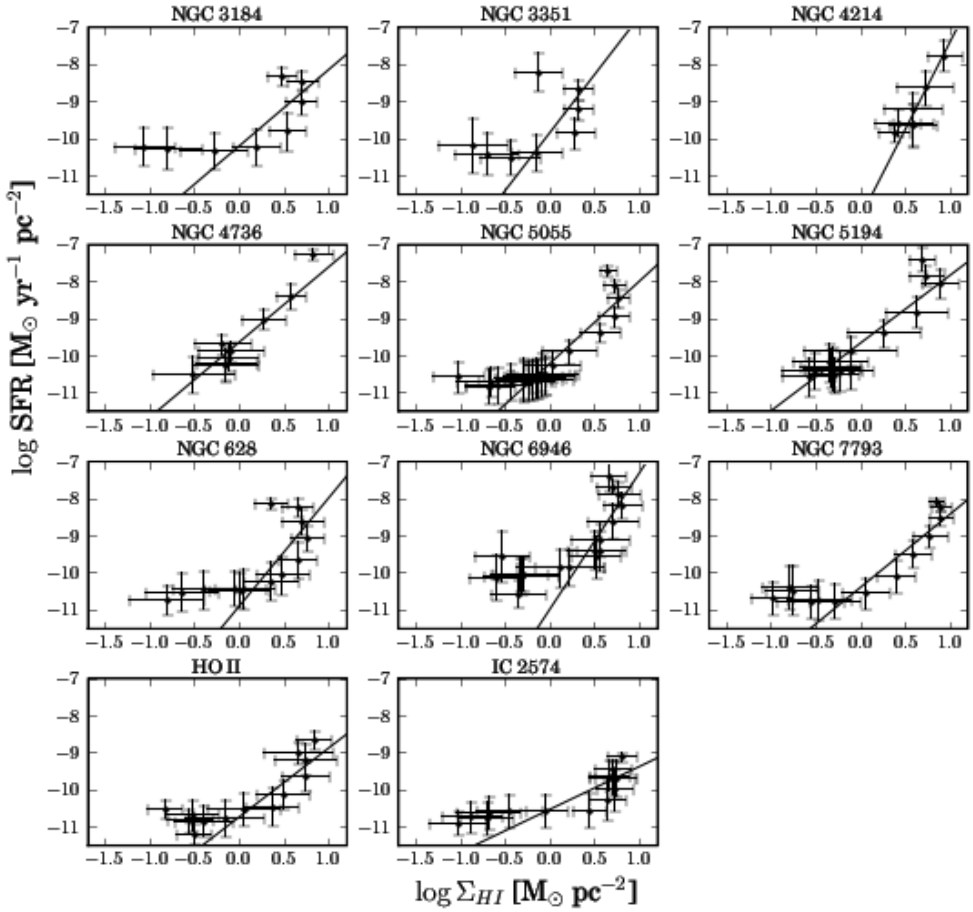

Figure 5.9: The $\Sigma_{\rm SFR}$ vs $\Sigma_{\rm HI}$ relation in radial bins. The innermost to the outermost bins are orderly denoted by highest to the lowest values of $\Sigma_{\rm SFR}$. See Fig. 5.7 for further description.

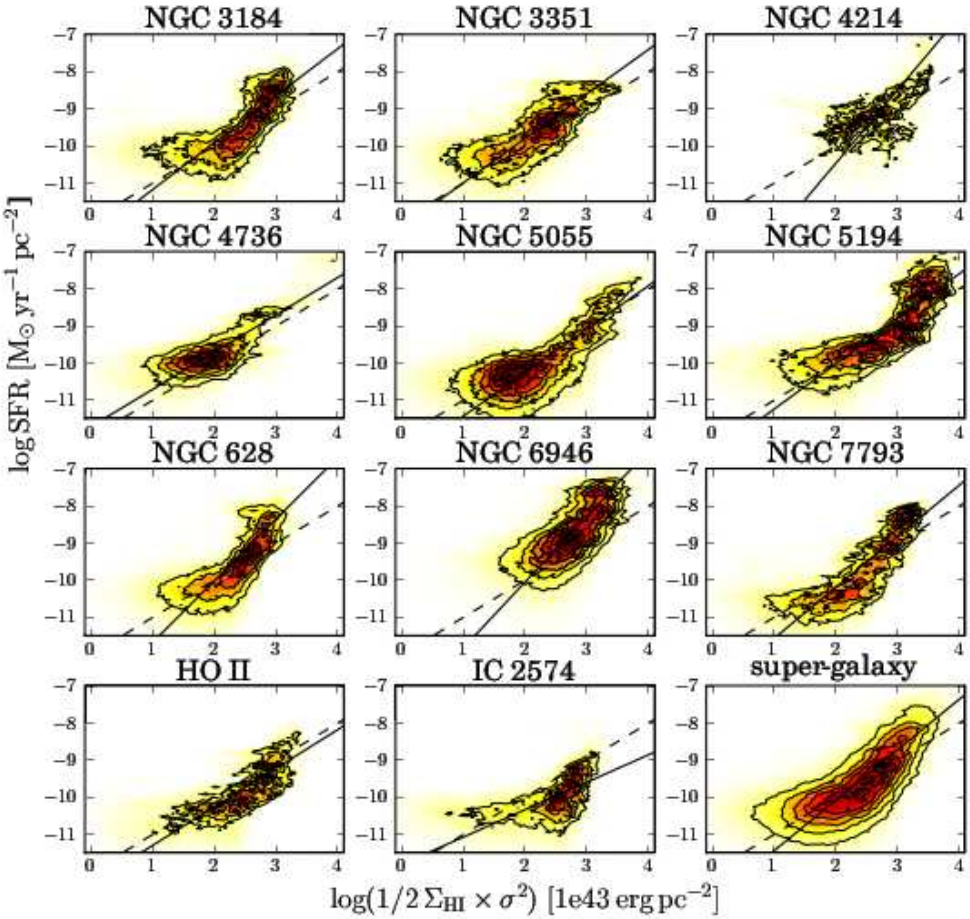

Figure 5.10: Pixel-by-pixel scatter plot of $\Sigma_{\rm SFR}$ vs $E_k = 1/2\ \Sigma_{\rm HI}\ \sigma^2$ for all the galaxies of our sample. The solid line represents the linear fit. For comparison the dashed line represent the unity slope such that $\log\ \Sigma_{\rm SFR} = -12 + \log E_k$ adopting the units expressed in the plot. The last panel (tagged "super-galaxy") represents the superposition of data points for all the galaxies of the sample.

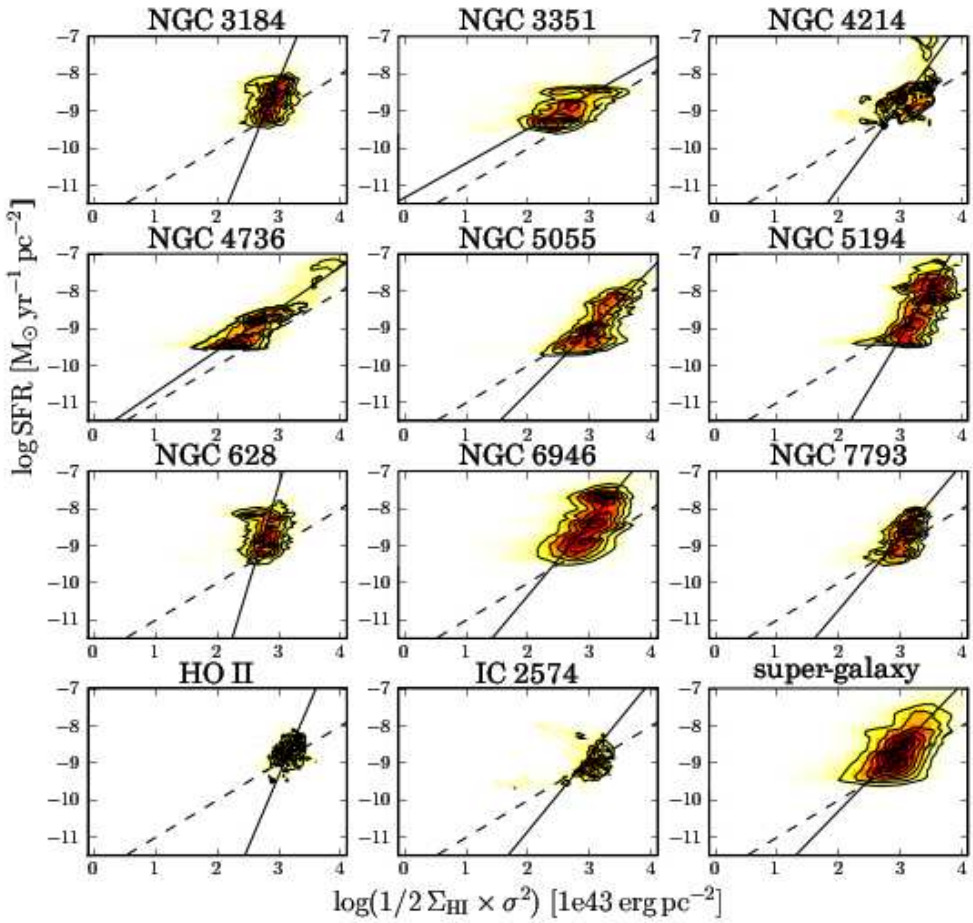

Figure 5.11: See description from Fig. 5.10. We ratained here only those $\Sigma_{\rm SFR}$ data points with high 24 μm + FUV flux; at low 24 μm + FUV flux $\Sigma_{\rm SFR}$ is calculted using the FUV flux only; we reject data points with low 24 μm flux and at $r > 1.5\, r_{25}$.

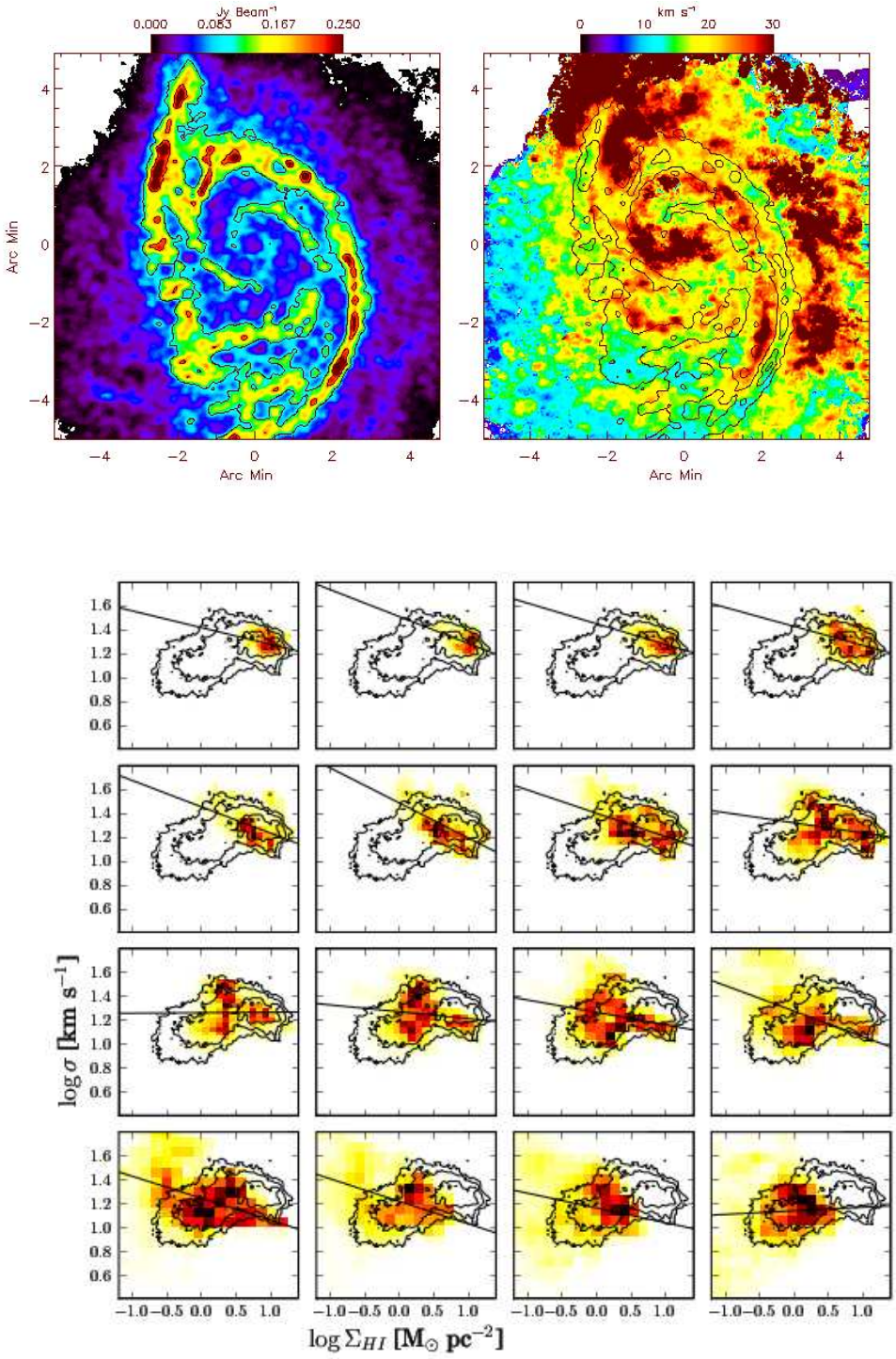

Figure 5.12: M51 – Top left: integrated H I column density map. Top right: H I velocity dispersion. In both top panels the contours denote levels of H I column density. Multi-box panel: the color scale represents the pixel-by-pixel density plot of σ vs $\Sigma_{\rm HI}$ for individual concentric rings by steps of 15″ width from $\sim 0.5r_{25}$ to $\sim 1.5r_{25}$; the solid line represents the best linear fit to these points; for comparison, the contours denote the density levels of all the pixels.

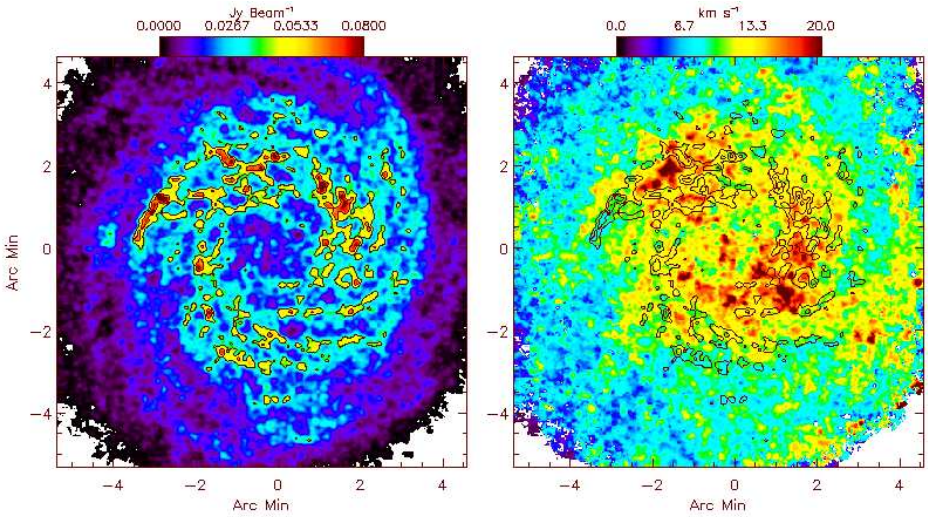

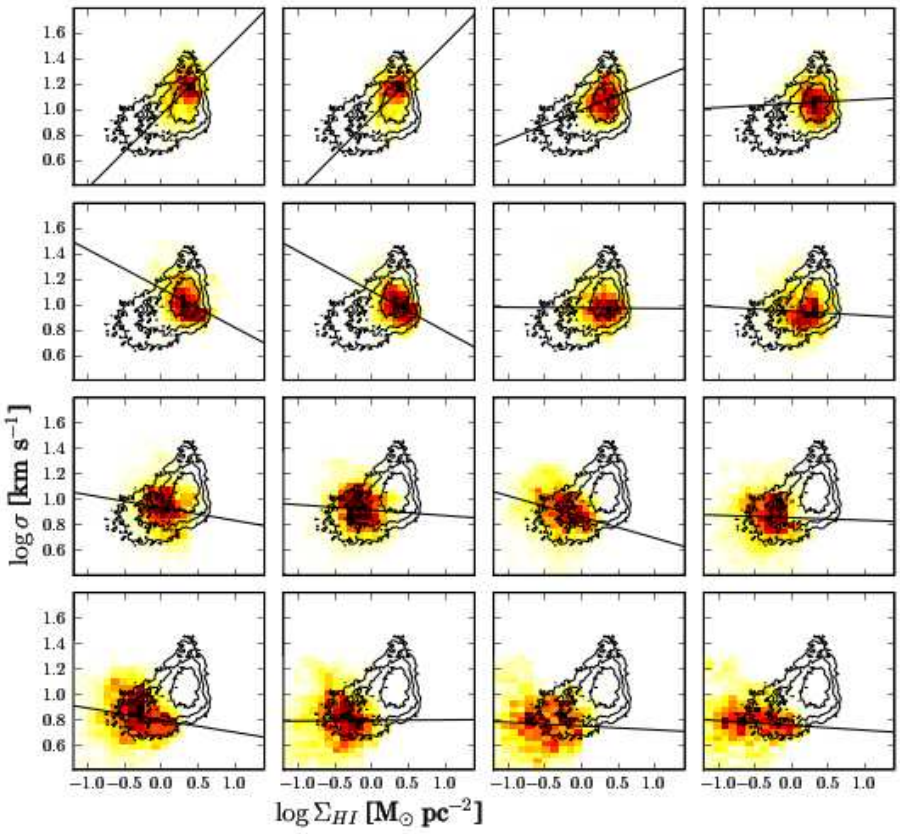

Figure 5.13: NGC3184 – See description from Fig. 5.12.

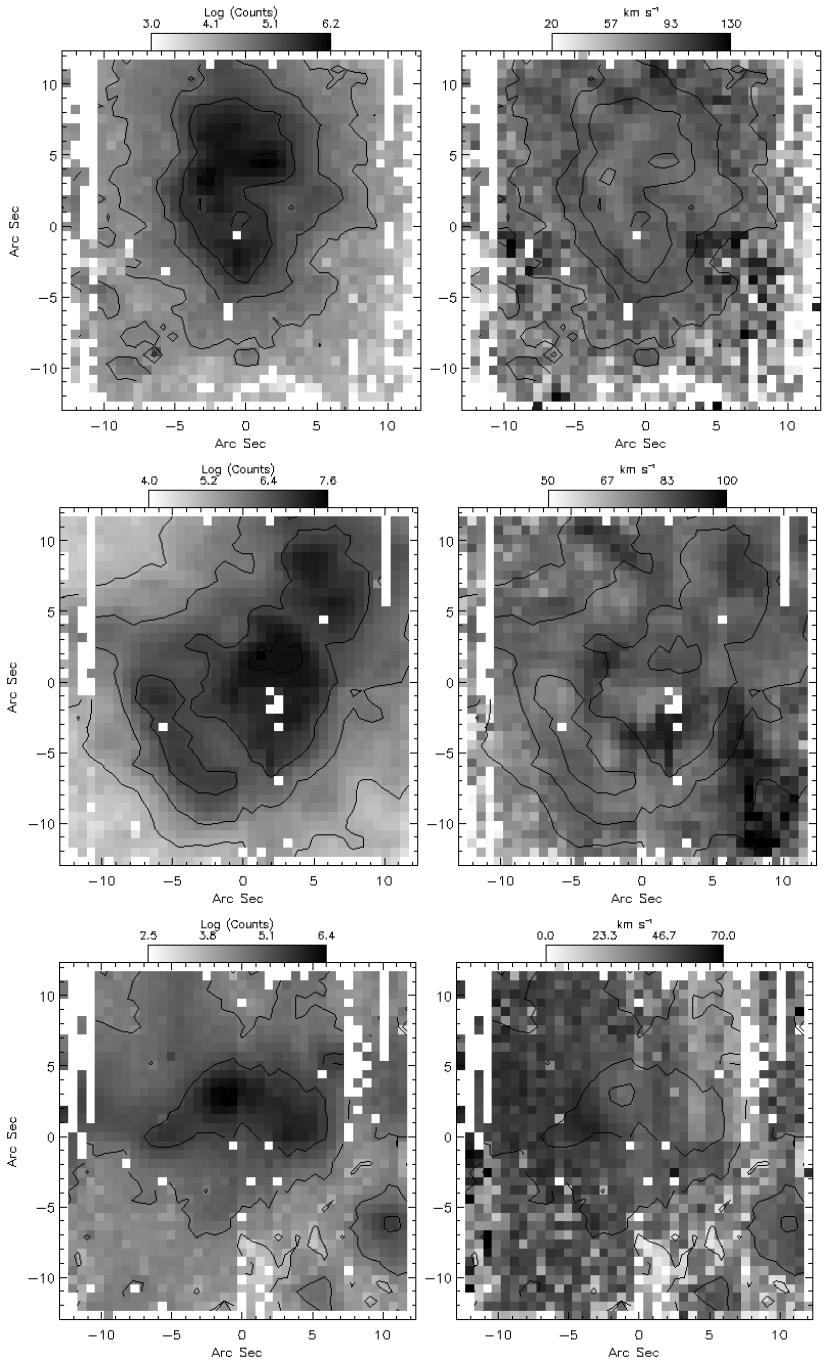

Figure 5.14: From top row to bottom: NGC 2903, NGC 5236, and NGC 7793. Left column: Hα emission map ([S II] λ6716.5 Å for NGC 2903) in arbitrary counts. Right column: ionized gas velocity dispersion. In both panels the contours denote the levels of Hα (or [S II]) emission.

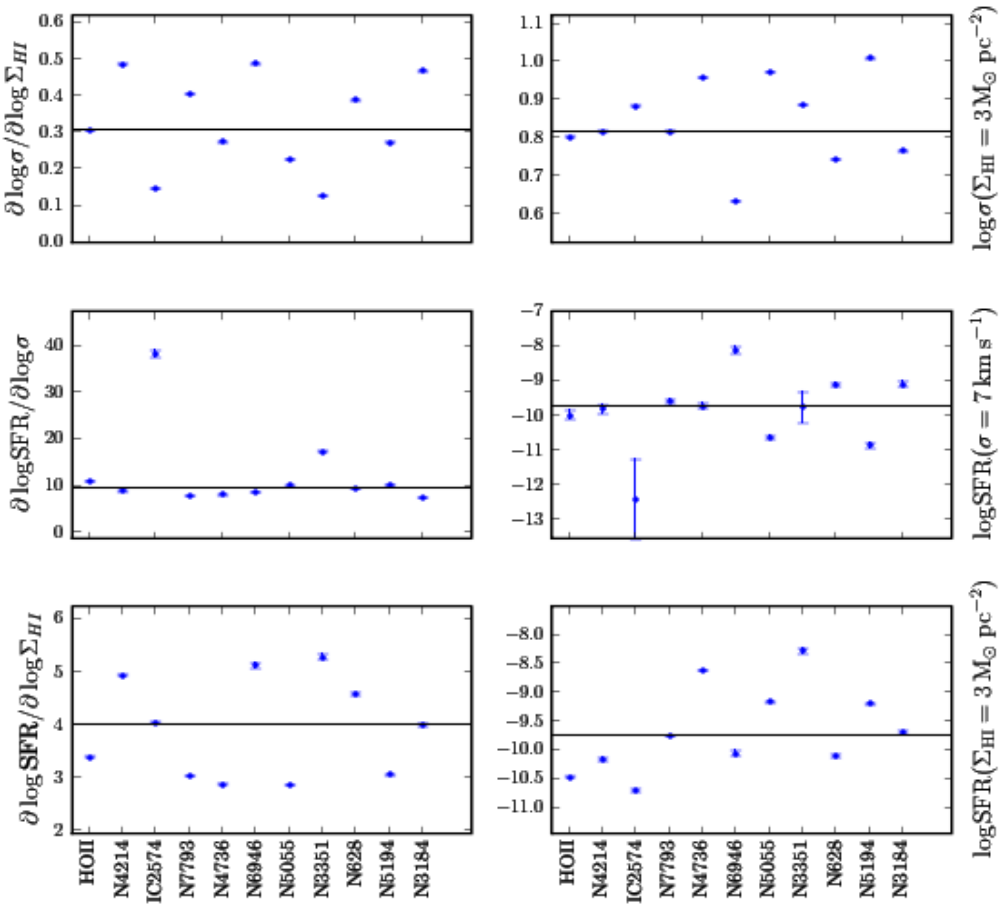

Figure 5.15: Same description as for Fig. 5.6, but using Gaussian moment maps.

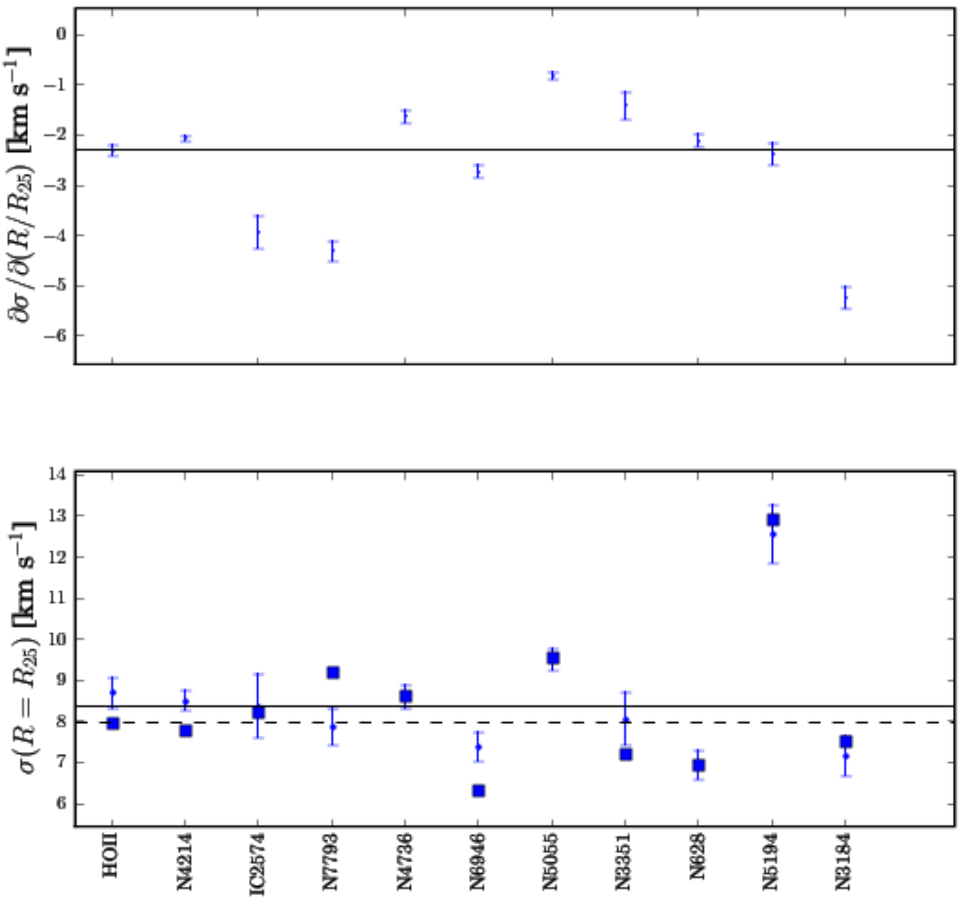

Figure 5.16: Same description as for Fig. 5.1, but using Gaussian moment maps.

Bibliography

Avila-Reese, V., & Vázquez-Semadeni, E. 2001, ApJ, 553, 645

Balbus, S. A., & Hawley, J. F. 1991, ApJ, 376, 214

Ballesteros-Paredes, J., Hartmann, L., & Vázquez-Semadeni, E. 1999, ApJ, 527, 285

Begeman, K. G. 1989, A&A, 223, 47

Bigiel, F., et al. 2008, AJ, submitted

Binney, J., & Tremaine, S. 1987, Princeton, NJ, Princeton University Press, 1987, 747 p.,

Blitz, L. 1993, Protostars and Planets III, 125

Blitz, L., Fukui, Y., Kawamura, A., Leroy, A., Mizuno, N., & Rosolowsky, E. 2007, Protostars and Planets V, 81

Blitz, L., & Shu, F. H. 1980, ApJ, 238, 148

Boissier, S., Prantzos, N., Boselli, A., & Gavazzi, G. 2003, MNRAS, 346, 1215

Bonazzola, S., Heyvaerts, J., Falgarone, E., Perault, M., & Puget, J. L. 1987, A&A, 172, 293

Boulanger, F., & Viallefond, F. 1992, A&A, 266, 37

Calzetti, D., et al. 2005, ApJ, 633, 871

Calzetti, D., et al. 2007, ApJ, 666, 870

Cho, J., & Lazarian, A. 2003, MNRAS, 345, 325

Dib, S., Bell, E., & Burkert, A. 2006, ApJ, 638, 797

Dib, S., & Burkert, A. 2005, ApJ, 630, 238

Dickey, J. M., Hanson, M. M., & Helou, G. 1990, ApJ, 352, 522

Dziourkevitch, N., Elstner, D., Rüdiger, G. 2004, A&A, 423, L29

Elmegreen, B. G. 1993, ApJL, 419, L29

Elmegreen, B. G. 2002, ApJ, 577, 206

Elmegreen, B. G., Elmegreen, D. M., & Leitner, S. N. 2003, ApJ, 590, 271

Elmegreen, B. G., Kim, S., & Staveley-Smith, L. 2001, ApJ, 548, 749

Elmegreen, B. G., & Scalo, J. 2004, ARA&A, 42, 211

Field, Goldsmith, & Habing, H. J. 1969, ApJL, 155, L149

Fleck, R. C., Jr. 1981, ApJL, 246, L151

Gammie, C. F., & Ostriker, E. C. 1996, ApJ, 466, 814

Gil de Paz, A., et al. 2007, ApJS, 173, 185

Goldreich, P., & Lynden-Bell, D. 1965, MNRAS, 130, 97

Gordon, K. D., et al. 2005, PASP, 117, 503

Heitsch, F., Mac Low, M.-M., & Klessen, R. S. 2001, ApJ, 547, 280

Heyer, M. H., Corbelli, E., Schneider, S. E., & Young, J. S. 2004, ApJ, 602, 723

Huber, D., & Pfenniger, D. 2001, A&A, 374, 465

Hunter, D. A., Elmegreen, B. G., & Baker, A. L. 1998, ApJ, 493, 595

Hunter, D. A., Elmegreen, B. G., & van Woerden, H. 2001, ApJ, 556, 773

Hunter, J. H., Jr., Sandford, M. T., II, Whitaker, R. W., & Klein, R. I. 1986, ApJ, 305, 309

Isobe, T., Feigelson, E. D., Akritas, M. G., & Babu, G. J. 1990, ApJ, 364, 104

Joung, M. K. R., & Mac Low, M.-M. 2006, ApJ, 653, 1266

Kamphuis, J. J. 1993, Ph.D. Thesis

Kennicutt, R. C., Jr. 1989, ApJ, 344, 685

Kennicutt, R. C., Jr. 1998, ApJ, 498, 541

Kennicutt, R. C., Jr., et al. 2003, PASP, 115, 928

Kennicutt, R. C., Jr., et al. 2007, ApJ, 671, 333

Kim, J., Balsara, D., & Mac Low, M.-M. 2001, Journal of Korean Astronomical Society, 34, 333

Kim, C.-G., Kim, W.-T., & Ostriker, E. C. 2006, ApJL, 649, L13

Kim, W.-T., & Ostriker, E. C. 2006, ApJ, 646, 213

Klessen, R. S., Heitsch, F., & Mac Low, M.-M. 2000, ApJ, 535, 887

Kornreich, P., & Scalo, J. 2000, ApJ, 531, 366

Leroy, A., et al. 2008, in preparation

Li, Y., Mac Low, M.-M., & Klessen, R. S. 2005, ApJL, 620, L19

Li, Y., Mac Low, M.-M., & Klessen, R. S. 2006, ApJ, 639, 879

Mac Low, M.-M. 1999, ApJ, 524, 169

Mac Low, M.-M., & Klessen, R. S. 2004, Reviews of Modern Physics, 76, 125

Mac Low, M.-M., Klessen, R. S., Burkert, A., & Smith, M. D. 1998, Physical Review Letters, 80, 2754

Martin, C. L., & Kennicutt, R. C., Jr. 2001, ApJ, 555, 301

McKee, C. F., & Ostriker, E. C. 2007, ARA&A, 45, 565

Murgia, M., Crapsi, A., Moscadelli, L., & Gregorini, L. 2002, A&A, 385, 412

Osterbrock, D. E., Fulbright, J. P., & Bida, T. A. 1997, PASP, 109, 614

Ostriker, E. C., Stone, J. M., & Gammie, C. F. 2001, ApJ, 546, 980

Padoan, P., & Nordlund, Å. 1999, ApJ, 526, 279

Pérez-González, P. G., et al. 2006, ApJ, 648, 987

Petric, A., & Rupen, M. P. 2001, Gas and Galaxy Evolution, 240, 288

Petric, A. O., & Rupen, M. P. 2007, AJ, 134, 1952

Passot, T., & Vázquez-Semadeni, E. 2003, A&A, 398, 845

Piontek, R. A., & Ostriker, E. C. 2005, ApJ, 629, 849

Quirk, W. J. 1972, ApJL, 176, L9

Rafikov, R. R. 2001, MNRAS, 323, 445

Rieke, G. H., et al. 2004, ApJS, 154, 25

Rix, H.-W., Guhathakurta, P., Colless, M., & Ing, K. 1997, MNRAS, 285, 779

Roberts, W. W. 1969, ApJ, 158, 123

Rownd, B. K., Dickey, J. M., & Helou, G. 1994, AJ, 108, 1638

Salim, S., et al. 2007, ApJS, 173, 267

Schaye, J. 2004, ApJ, 609, 667

Sellwood, J. A., & Balbus, S. A. 1999, ApJ, 511, 660

Spitzer, L. J. 1942, ApJ, 95, 329

Spitzer, L. J. 1968, Nebulae and interstellar matter. Edited by Barbara M. Middlehurst; Lawrence H. Aller. Library of Congress Catalog Card Number 66-13879. Published by the University of Chicago Press, Chicago, ILL USA, 1968, p.1, 1

Spitzer, L. 1978, New York Wiley-Interscience, 1978. 333 p.

Stone, J. M., Ostriker, E. C., & Gammie, C. F. 1998, ApJL, 508, L99

Talbot, R. J., Jr., & Arnett, W. D. 1975, ApJ, 197, 551

Tamburro, D., et al. 2008, AJ, submitted

Toomre, A. 1964, ApJ, 139, 1217

van der Hulst, J. M., Skillman, E. D., Smith, T. R., Bothun, G. D., McGaugh, S. S., & de Blok, W. J. G. 1993, AJ, 106, 548

van der Kruit, P. C., & Shostak, G. S. 1982, A&A, 105, 351

van Zee, L., & Bryant, J. 1999, AJ, 118, 2172

van Zee, L., Haynes, M. P., Salzer, J. J., & Broeils, A. H. 1997, AJ, 113, 1618

Wada, K., & Koda, J. 2004, MNRAS, 349, 270

Wada, K., Meurer, G., & Norman, C. A. 2002, ApJ, 577, 197

Walter, F., et al. 2008, AJ, submitted

Wannier, P. G., Lichten, S. M., Andersson, B.-G., & Morris, M. 1991, ApJS, 75, 987

Williams, J. P., Blitz, L., & McKee, C. F. 2000, Protostars and Planets IV, 97

Williams, J. P., Blitz, L., & Stark, A. A. 1995, ApJ, 451, 252

Wong, T., & Blitz, L. 2002, ApJ, 569, 157

Chapter 6

Conclusions

6.1 Star Formation and HI Kinematics

The main questions addressed in this thesis focus on how rapidly star formation takes place after the gas has collapsed, and what impact the onset of star formation has on the surrounding ISM.

The time scales for stars to form from the assembly of H I gas clouds and their procession into the molecular phase are measured using a geometric method. We assume that the spiral wave, the network of dense gaseous structures in galaxy disks, remains stationary from end-to-end of the process – from the early gaseous phase to the shining of young hot stars onto their enshrouding molecular envelopes, so that these two distinct phases are "frozen" in the two distinct corresponding wavelength tracers, rotated with respect to each other. Then, the rotation velocity, obtained from the H I kinematics, permits to interpret the angular offsets in terms of time lag from end-to-end.

The onset of star formation, with the consequent existence of winds and UV radiation from hot stars and SNe explosions, is likely to be violent. We question which part of the non-ordered motions of the gas might be due to star formation feedback. Overall, we tackle the problem from two main directions. We model the observed H I velocity fields of spiral galaxies and try to separate the gravitationally induced motions from the turbulent motions. We assume that the large-scale irregularities of the H I velocity fields are due to perturbations induced by a non-axisymmetric gravitational potential. The results suggest that our method can, at first order, provide a reasonable measure of the pattern speed of bars distorting the velocity fields. However, our approach can not recover the fine structure of the gas motions. By contrast, we argue that the H I velocity dispersion might better represent the turbulent motions. From this other perspective, we compare maps of H I velocity dispersion and surface density of star formation rate (SFR) to test our basic statement, that is whether star formation affects the local gas dynamics.

We extensively use high resolution and sensitivity maps at the 21-cm wave-

length obtained with the NRAO Very Large Array, and at infra-red wavelengths (mostly employing the 24 μm band) obtained with the Spitzer space telescope. The 21-cm maps trace the atomic neutral (H I) gas, which constitutes the bulk of total gas content in normal spiral galaxies and dwarf galaxies. The infra-red emission maps trace the dust heated by young massive stars, therefore represent the optimal proxy for star formation activity. Combining those data (§ 6.1.1) we explore the fundamental questions posed in this thesis. We summarize in the next sections our main results on the optimal modeling of H I velocity fields (§ 6.1.2), on the time scales for star formation in spiral arms environment (§6.1.3), and on the study of the interplay between turbulence and star formation (§ 6.1.4).

6.1.1 The Data Sample: SINGS and THINGS

The two large observational campaigns, The Spitzer Infrared Nearby Galaxies Survey (SINGS; Kennicutt et al. 2003) and The H I Nearby Galaxy Survey (THINGS; Walter et al. 2008), enable a detailed study of gas and stellar populations, star formation processes and phases of the ISM, in a multi-wavelength perspective, preserving at the same time a large field coverage, which permits a panoramic view of the target galaxies (Chapter 2). SINGS and THINGS have surveyed a large number of nearby spiral galaxies and dwarf galaxies, spanning over diverse morphological types, star formation rates, metalicities, dynamical masses, etc. The exploitation of the SINGS and THINGS maps offers a promising insight into open issues, in particular, star formation on galactic scales and the star formation laws, gas phase balance, and consumption of the gas reservoir, origin of the Hubble sequence and galaxy evolution.

Since the 21-cm maps of THINGS have become available for analysis, several areas of exploration have been already targeted, spanning over kinematics and dynamics implied by the H I velocity maps combined with stellar surface density maps, over the study of morphological structures e.g. holes and supergiant shells displayed in the H I maps of several galaxies of the sample, and the relation of these structures with feedback from star formation activity, and ultimately tests pixel-by-pixel of the Schmidt-Kennicutt law and of the star formation thresholds. Specifically in this thesis, we focus on determining the time scales for the onset of star formation since the commence of gravitational instability (Chap. 4), based on a geometric method which clearly opens the opportunity to extend its application to other bands. Also, we carry out a comparative study of small scale kinematics of the gas, in terms of deviations from laminar flow or of velocity dispersion, and indicators of star formation (Chapters 3 and 5).

The multi-wavelength observations have improved our understandings on stellar populations and more importantly on the ISM phases and dynamics. Note, in fact, that the emission and absorption features of the gas are distributed over a vast range of the radiation spectrum, from radio to the γ-rays. The successful achievements of SINGS and THINGS is due indeed to the multi-wavelength studies.

6.1.2 Models of Velocity Fields

A possibility to analyze deviations from the motions due to the global gravitational potential of galaxies could be carried out through the optimal modeling of the velocity field, including perturbations to the axisymmetric potential (Chapter 3). The motivation of such an analysis points toward the understanding of the nature of these deviations. Their amplitude and the location may contain informations on their driving source. Possibly, the fact that regions of recent star formation are characterized by energetic activities as SNe explosions, superbubbles, stellar winds, ionizing radiation, etc., is suggesting that a substantial fraction of this energy feedback is transferred to the ISM and produce turbulent motions which are ultimately observable as H I velocity dispersion or net deviations from the global rotation dictated by the galactic potential. In these circumstances, with a spectral resolution of ~ 5 km s^{-1} the H I velocity maps from THINGS represent the optimal tool. The mass and the amplitude of the velocity deviations can be used in order to calculate the associated kinetic energy, and constrain the energy of the driving source.

Our approach is based on an analytical model of the potential described in terms of a non-axisymmetric perturbation contributing the axisymmetric component of gravitational potential, that ultimately provides a model of the velocity field. A perturbation in the potential causes the orbiting gas particles to deviate from their equilibrium point and develop harmonic oscillations at the epicyclic frequency about this point. If the azimuthal dependence of the non-axisymmetric perturbation is expressed in terms of harmonic functions, thus sine and cosine, this approach permits to describe the velocity field in terms of Fourier series. In particular, a perturbation with azimuthal order of m will produce in the velocity field harmonic terms of order $m-1$ and $m+1$. We decompose the observed velocity map v_{obs} in harmonic coefficients $(c_n, s_n)_{obs}$, which, then, we model as function of galactocentric radius, and, ultimately, obtain from the best fit the model harmonic coefficients $(c_n, s_n)_{mod}$, which allow to reconstruct the model velocity field v_{mod}.

Minimizing the residual map $v_{obs} - v_{mod}$ down to a satisfactory level has proven to be not trivial. First of all, the model itself could be not sufficiently accurate. The character of the actual perturbation could be more complex, both in the radial and in the azimuthal directions, than its corresponding analytic description. Likewise, the assumption of a stationary perturbation is questionable. Besides, velocity deviations are possibly ensued by effects of disk instabilities due to the influence of magnetic fields and/or to large scale gravitational instabilities (Kim & Ostriker 2002, 2006; Li, Mac Low, & Klessen 2005, 2006), which cause large regions of gas to collapse. In these terms, to track the gas kinematics analytically would be quite complicated.

The model can resemble the pattern speed of the perturbations that are causing part of the distortions in the velocity field, as we show for the barred galaxy NGC 2903. The typical velocity residuals for the face-on galaxy NGC 3184 obtained after subtracting the model have values up to $5-10$ km s^{-1}. This is suggesting that our model can describe neither this level of amplitude nor the lo-

cation of the resulting structured velocity deviations, and that the observed H I kinematics is considerably more complex than what our methodology predicts.

Perspectives

With regard to the theory here illustrated, the adopted methodology could be improved in order to better mimic the complexity of the gravitational potential. Clearly, this does not appear to be the primary issue, since disk instabilities could play a major role. However, it may deserve further consideration, more precisely, taking into account for the stellar surface density maps. We raise, in this perspective, a natural question: at what level, in terms of absolute velocity deviations, can the azimuthal variations in the stellar mass distribution drive the gas kinematics? In addition, since high order structured residuals persist even after subtracting more and more complex forms of perturbations from the velocity field v_{obs}, this is suggesting that velocity deviations may occur over a full wealth of scale sizes. At this point, an additional natural question addresses to the Kolmogorov character of the velocity field, and in particular whether the size distribution of the velocity field, residuals, gas distribution and stellar map are all consistent with this broad picture. In this case, the same driving source of the turbulence in the ISM would also be be the cause of the velocity deviations.

6.1.3 Time Scales for Star Formation

We use outstanding data to show that – at least a portion of – the star formation near spiral arms is very rapid (Chapter 4). To avoid conflicts with gas consumption arguments, star formation either has to be inefficient, or we are seeing the initially triggered population of young stars.

We estimate the characteristic time-scale for star formation in disk galaxies, going from H I gas to dust enshrouded young massive star clusters. We measure the angular offset between the H I and 24 μm emission patterns taken from SINGS and THINGS data samples, respectively. Assuming that these two wavelengths trace two distinct epochs differing by a time span $t_{\mathrm{HI}\mapsto 24\,\mu\mathrm{m}}$, and that the spiral wave is characterized by an instantaneous kinematic pattern speed Ω_p, the angular offset as function of radius is given by $\Delta\phi = (\Omega - \Omega_p) \times t_{\mathrm{HI}\mapsto 24\,\mu\mathrm{m}}$, where knowing the rotation velocity Ω of the H I, allows to obtain Ω_p and $t_{\mathrm{HI}\mapsto 24\,\mu\mathrm{m}}$. For the characteristic time-span between the dense H I phase and the existence of massive stars that heat the surrounding dust, we find $t_{\mathrm{HI}\mapsto 24\,\mu\mathrm{m}}$ ranging between 1 and 4 Myr.

According to the observational results of the last few decades, the time scale for star formation to set in is not a well constrained parameter. Although, this may be due to effects of limited resolution. Our results are consistent with a rapid procession of the molecular phase ultimately resulting in star formation and exclude, at least at high regimes of SFR, that star formation proceeds slowly. Rapid star formation is suggesting a few implications. First, molecular cloud evolution occurs on a dynamical time once gravitational instability has set in,

however we can not constrain the total lifetime of molecular gas in these regions, which could initially produce a burst of star formation, and subsequently get dispersed by star formation itself, but still forming stars within sub-fragments. Molecular clouds are not likely to be quasi-static systems evolving over many free-fall times. Second, the rate-limiting step for star formation is the assembly of H I gas into gravitationally unstable configurations. That is, only after that the H I regions have grown super-critical they can collapse into molecular clouds. Ultimately, the short time scales found here are suggesting that star formation must be relatively inefficient to avoid the short term depletion of gas reservoir.

Perspectives

Clearly, this approach applies also to other wavelength bands and could be used to constrain the various evolutionary phases of the ISM, providing an alternative method for estimating time scales, on the condition that we are able to unambiguously attribute to a given wavelength the corresponding epoch. For instance, the CO traces the molecular phase that precedes star formation, however not necessarily all the molecular clouds undergo collapse, and some of those could survive to the star formation feedback. The Hα emission, instead, traces ongoing star formation activity only after it has set on. Moreover, since Hα radiation can be easily absorbed by the dust enshrouding star forming regions, the appearance of Hα emission indicates that the obscuring molecular envelop has been removed by the stellar feedback. If compared to the $t_{\mathrm{HI}\mapsto 24\,\mu\mathrm{m}}$ time scale, the H I-to-Hα phase time lag could provide constraints on the break out time of star forming regions, and constrain the lifetime of molecular clouds. On the same line of reasoning, the technique is applicable to measure the age of the populations traced by the UV emission, and compare it to previous independent studies.

6.1.4 Turbulence in the HI

We reconsider the question whether the star formation activity is able – via SNe explosions, winds from young stars, etc. – to inject energy into the ISM that results in turbulent gas motions (Chapter 5). As an alternative to modeling the H I velocity fields and focusing on the velocity residuals, we consider directly the velocity dispersion. We compare maps of H I surface density mass, H I velocity dispersion obtained from THINGS, and surface density of star formation rate (SFR) obtained from SINGS. In our analysis we find that velocity dispersion and SFR are correlated for a sample of spiral and dwarf galaxies. Also, we find radial systematic decline of H I velocity dispersion, accordingly with the radial decline of SFR, and a common value of velocity dispersion, 10 ± 1 km s^{-1}, in correspondence with common values of stellar surface brightness, $B = 25$ mag arcsec^{-2}, H I surface density mass, ~ 3 M$_\odot$ pc^{-2}, and SFR, $\sim 10^{-9.5}$ M$_\odot$ year^{-1} pc^{-2}.

Our results show that the SFR and the H I velocity dispersion are correlated. We conclude that the H I turbulence could be driven by feedback of star formation activity. Moreover, the weak dependence of velocity dispersion as

function of SFR suggests that turbulence is not able to efficiently induce star formation by generating stochastic density enhancements in the gas that could grow super-critical. However, we could also interpret the positive correlation between SFR and velocity dispersion as an indirect interplay. Both these quantities relate to the local gravity, which balances the velocity dispersion (of gas and stars) and facilitate the collapse of gas clouds. The onset of large scale gravitational instability can in principle also produce turbulence in the gas. In these circumstances, both SFR and velocity dispersion increase accordingly with the strength of the gravitational instability.

Perspectives

This field of investigation, although quite promising, reveals the necessity for improving our analysis before drawing premature conclusions. In particular, our SFR maps need to be improved, provided that they exhibit biases at low regimes of SFR. Though we have already obtained a set of innovative results by analyzing the H I velocity dispersion and the SFR, we also propose to narrow our analysis on sub-sets of small regions, which so far have been considered only qualitatively. Possibly, in order to test our final statements, we would need to measure the velocity dispersion of the stars in order to constrain the vertical distribution of the gravitational potential, which, as we argue, determines the regime of velocity dispersion of the gas.

6.1.5 Summary of the Results

We address, as the main result of this thesis, the short time scales for massive star clusters to form. Star formation in spiral arms environment takes place in 1–4 Myr. Our results are consistent with a scenario in which star formation sets on as rapidly as physically possible where the SFR is the highest, suggesting therefore that it occurs on small scales, and exclude the possibility of slow star formation, although our methodology can not test these time scales at the lowest regimes of SFR.

The modeling of observed H I velocity maps even including non-axisymmetric perturbations, reveals large scale velocity residuals after subtracting the model reconstruction from the actual velocity field. On the one hand, our approach can retrieve the pattern speed of the considered non-axisymmetric components, but on the other, it is suggesting that the H I kinematics is much more complex than we assumed.

The analyzed galaxies exhibit that the H I velocity dispersion declines radially with a constant rate, and has a common value of ~ 10 km s^{-1} at r_{25}. Our preliminary results are also suggesting that star formation could be a driving mechanism of turbulence in the ISM. We also conclude that turbulent density waves do not represent an effective mechanism for inducing star formation. We can not exclude that the same mechanism that produces the observed regime of velocity dispersion, is also inducing the large scale velocity deviations from gravitationally induced orbital motions – large scale gravitational instability.

Bibliography

Kennicutt, R. C., Jr., et al. 2003, PASP, 115, 928

Kim, W.-T., & Ostriker, E. C. 2002, ApJ, 570, 132

Kim, W.-T., & Ostriker, E. C. 2006, ApJ, 646, 213

Li, Y., Mac Low, M.-M., & Klessen, R. S. 2005, ApJL, 620, L19

Li, Y., Mac Low, M.-M., & Klessen, R. S. 2006, ApJ, 639, 879

Walter, F., et al. 2008, AJ, submitted

I gratefully acknowledge the people that worked with me during these three years and gave their scientific contribution to this thesis.

In first place, I am indebted with Hans-Walter Rix – more than a supervisor, a colleague – for being always present and patient, for training me professionally, for providing his relief when needed and granting me enough liberty during my research.

My gratitude also goes to Fabian Walter, for our interactions troughout this intriguing project, for the tips from which I benefitted much and the friendly atmosphere that has emerged.

I am grateful to the THINGS collaboration team, and especially Elias Brinks, Erwin de Block, and Rob Kennicutt for all useful and constructive comments, and for helping me improving my work.

I thank Mordecai-Marc Mac Low for joining our research and provide to it a significant upgrade.

I thank Ralph Klessen for his interest in my thesis and supplying comments.

I also wish to thank Enrik Beuther for useful discussions, Sami Dib for feeding back with ideas on feedback, Adam Leroy for rendering Chapter 5 more and more turbulent, Anna Pasquali for being delightfully nice commenting my thesis, Nacho Trujillo for our animated and fervid exchanges of ideas, Stefano Zibetti for reading and commenting part of my thesis, the students of the THINGS team, especially Frank Bigiel, and my originary research group Alessandro Pizzella, Enrico Maria Corsini, and Francesco Bertola.

My profound gratitude goes to the old friends and the new ones that I knew durinng these three years, starting from Fulvio, the first person I met at the MPIA – he practically opened the door as I arrived at the institute – for being so generous; Alessandro for the good time and the lost ping-pong matches; José for his bright complicity; Alex for the nice coffee-time friendship; Lorena G. for the truthful and genuine friendship; Claudia, a colorful comrade; Patrizia for her kindness; Aldo, an outstanding bloke; Orlando, though very far, always so near; Serena and Matteo for their picturesque presence; Maurizio, to his memory, such a seizing waste.

A very warm-harted thank you is addressed to Stefano and Lorena for being always there, generous and odd.

Special thanks to my parents, Antonio and Mariantonietta, to my sister, Maria Luisa, and to my grandmother, Maria, for being always by my side, for their relief in the bad times, for their unreserved love.

I wish to dedicate this thesis to Caterina, my horizon and source of joy, for casting my shelter and easing my burdens. We are a powerful team.